INFORMATION TO USERS

This manuscript has been reproduced from the microfilm master. UMI films the text directly from the original or copy submitted. Thus, some thesis and dissertation copies are in typewriter face, while others may be from any type of computer printer.

The quality of this reproduction is dependent upon the quality of the copy submitted. Broken or indistinct print, colored or poor quality illustrations and photographs, print bleedthrough, substandard margins, and improper alignment can adversely affect reproduction.

In the unlikely event that the author did not send UMI a complete manuscript and there are missing pages, these will be noted. Also, if unauthorized copyright material had to be removed, a note will indicate the deletion.

Oversize materials (e.g., maps, drawings, charts) are reproduced by sectioning the original, beginning at the upper left-hand corner and continuing from left to right in equal sections with small overlaps. Each original is also photographed in one exposure and is included in reduced form at the back of the book.

Photographs included in the original manuscript have been reproduced xerographically in this copy. Higher quality 6" x 9" black and white photographic prints are available for any photographs or illustrations appearing in this copy for an additional charge. Contact UMI directly to order.

UMI

A Bell & Howell Information Company
300 North Zeeb Road, Ann Arbor MI 48106-1346 USA
313/761-4700 800/521-0600

Formation and Characteristics of Sprays from Annular Viscous Liquid Jet Breakup

by

Jihua Shen
B.Sc., Southwestern Petroleum Institute, 1984
M.Sc., University of New Brunswick, 1992

A Dissertation Submitted in Partial Fulfillment of the
Requirements for the Degree of
DOCTOR OF PHILOSOPHY
in the
Department of Mechanical Engineering.

We accept this Dissertation as conforming
to the required standard

Dr. X. Li, Supervisor (Dept. of Mechanical Engineering)

Dr. S. Dost, Departmental Member (Dept. of Mechanical Engineering)

Dr. N. Djilali, Departmental Member (Dept. of Mechanical Engineering)

Dr. A. Weaver, Outside Member (School of Earth and Ocean Sciences)

Dr. P. G. Hill, External Examiner (University of British Columbia)

Supervisor: Dr. Xianguo Li

Abstract

The formation process and characteristics of sprays from annular liquid jet breakup in moving gas streams have been investigated. In the first part of the thesis, a linear instability analysis is carried out for the instability and breakup of annular liquid jets. A dispersion relation has been derived and solved numerically by using Muller's method. Temporal instability analysis shows that two independent unstable modes, para-sinuous and para-varicose, exist for the annular jet instability. The para-sinuous mode outgrows the para-varicose one at relatively low gas-liquid density ratios and large Weber numbers as typically encountered in the twin-fluid atomization. The curvature of the annular jet promotes the jet instability and may not be neglected for the breakup processes of annular liquid jets. Not only the velocity difference across each interface but also the absolute velocity of each fluid is important for the jet instability. Co-flowing gas at high velocities is found to significantly improve atomization performance.

A mesh-searching method has been developed to determine absolute mode of instability. The numerical results indicate that both absolute and convective instability exist for para-sinuous and para-varicose modes under certain flow conditions. Para-sinuous unstable waves outgrow para-varicose ones, and hence dominate the jet instability according to both absolute and convective instability analysis. The liquid viscosity has a simple stabilizing effect on the jet instability while the gas inertial force shows fairly complex influence on the absolute instability of the jet. The convective growth rates for various inner gas velocities indicate that not only the velocity difference between, but also the absolute velocity of the liquid and gas, determine the jet breakup process.

In the second part of this thesis, experimental investigations have been conducted for the breakup process of annular water jets exposed to an inner air stream by photographic technique, and the characteristics of the resultant sprays by Phase Doppler Particle Analyzer. Two annular nozzles of the same structure but different dimensions are designed and constructed especially to provide smooth contraction for the liquid flow. The test apparatus is constructed to produce the annular liquid sheets or sprays of good quality.

Flow visualization reveals that there exist three regimes. i.e., bubble formation, annular jet formaion and atomization regime for the jet breakup process. Within the bubble formation regime, the jet breakup characteristics measured from the photographs taken under various liquid and gas velocities show that uniform bubbles are observed for various air-to-water velocity ratios. The jet breakup and wave lengths

decrease with the air-to-water velocity ratio. The measurements are compared with the predictions by the linear instability analysis, and fair agreement is obtained.

Spray characteristics measured by a Phase Doppler Particle Analyzer indicate that using atomizing air enhances the jet breakup process and improves the atomization performance by producing fine sizes of droplets and increasing the uniformity of drop sizes. The drop axial velocity has a jet-type distribution in the radial direction, and decreases monotonically along the spray axis. Increase in the water and air velocities results in higher drop axial velocity. The droplet size described by its Sauter mean diameter (SMD) reaches a minimum value at the central region of the spray and increases towards the spray edge. The SMD has a complex variation along the spray axis.

Examiners:

Dr. X. Li, Supervisor (Dept. of Mechanical Engineering)

Dr. S. Dost, Departmental Member (Dept. of Mechanical Engineering)

Dr. N. Djilali, Departmental Member (Dept. of Mechanical Engineering)

Dr. A. Weaver, Outside Member (School of Earth and Ocean Sciences)

Dr. P. G. Hill, External Examiner (University of British Columbia)

Table of Contents

List of Tables

List of Figures

Nomenclature

d	diameter of individual droplet (μm)
D_b	bubble diameter (mm)
i	imaginary number, $i = \sqrt{-1}$
I_0, I_1	modified Bessel function of the first kind of order 0 and 1
k	dimensionless wave number, $k = \alpha r_h$
K_0, K_1	modified Bessel function of the second kind of order 0 and 1
L_B	jet breakup length (m)
L_w	wave length (m)
mr	magnification rate
p	pressure change induced by perturbation (N/m^2)
$\tilde{p}$	initial amplitude of pressure p (N/m^2)
P, $\bar{P}$	pressure of perturbed and base flow (N/m^2)
r_a	dimensionless inner radius, $r_a = r_a^*/r_h$
r_a^*	inner radius of annular sheet (m)
r_b	dimensionless outer radius, $r_b = r_b^*/r_h$
r_b^*	outer radius of annular sheet (m)
r_h	reference length scale (m), $r_h = r_a^*, r_b^*$ or $(r_b^* - r_a^*)/2$
r_m	mean sheet radius (m), $r_m = (r_a^* + r_b^*)/2$
Re	Reynolds number, $Re = U_h^* r_h/\nu_\ell$

t	time (s)
$\mathbf{u}$	change of velocity vector induced by perturbation (m/s)
$\tilde{\mathbf{u}}$	initial amplitude of velocity $\mathbf{u}$ (m/s)
$\mathbf{U}$, $\bar{\mathbf{U}}$	velocity vector of perturbed and base flow (m/s)
U^*	axial velocity of base flow (m/s)
U	dimensionless axial velocity of base flow, $U = U^*/U_h^*$
We	Weber number, $We = \rho_\ell U_h^{*2} r_h/\sigma$
z	Coordinate along flow axial direction (m)

Greek Symbol

α	wave number $(1/m)$
ϵ	initial amplitude of disturbance (m)
η	displacement of interface from its initial equilibrium position (m)
θ	phase difference
λ	wavelength (m), $\lambda = 2\pi/\alpha$
μ	dynamic viscosity $(kg/m \cdot s)$
ν	kinematic viscosity (m^2/s)
ρ_n	density (kg/m^3), subscript $n = g, \ell$
ρ	density ratio, $\rho = \rho_g/\rho_\ell$
σ	surface tension (N/m)
ω	dimensionless wave frequency, $\omega = \Omega r_h/U_h^*$
Ω	wave frequency $(1/s)$

Subscript

- a for inner gas medium or at inner interface
- b for outer gas medium or at outer interface
- ℓ for liquid jet
- g for both inner and outer gas medium
- h for reference length and velocity scale
- i for imaginary part of a complex
- r for real part of a complex

Acknowledgements

I would like to express my deepest gratitude to my supervisor, Dr. X. Li, for his continuous support, guidance and encouragement throughout all of this work. I would also like to thank Dr. S. Dost, Dr. N. Djilali, Dr. A. Weaver and Dr. P. G. Hill for serving on my thesis examination committee.

The assistance from Mr. R. Katz in the installation of the experimental apparatus and from Mr. Jianming Cao in taking photograph for liquid jets is highly appreciated.

The financial support from the University of Victoria and the Natural Sciences and Engineering Research Council of Canada is gratefully acknowledged.

To my dearest parents, supportive husband and lovely son
who make my life full of happiness

Chapter 1

Introduction

When a liquid is injected under pressure from a nozzle into a surrounding gas medium, a continuous liquid jet is formed. Because of its inherent instability or its inability to sustain itself against even small perturbations, to which any physical system is subject, the liquid jet develops unstable waves, which amplify downstream, and eventually it disintegrates into a train of droplets. The process of the liquid jet breakup consists of two fundamental steps. The first step is that the jet breaks up into ligaments. The second is that the ligaments further disintegrate into fine droplets. This process of liquid jet breakup into ligaments and then ligaments into droplets of fine sizes is often referred to as liquid atomization. The nozzle from which the liquid emanates is called atomizer, and the cluster of fine droplets so produced is usually termed as a spray.

Sprays have wide applications in not only our daily life but also industries for decades [1, 2]. Hair sprays can be generated by simply forcing jelly through a fine orifice nozzle. Agricultural spraying of herbicides, fungicides and insecticides is carried out on a huge scale in all countries using aircraft and tractors. In material processing industry, liquid metal and ceramic sprays are used to manufacture tools, dyes, gear

wheels and a wide variety of objects with complex shapes. Instead of casting and machining materials, material shapes are being formed by spraying layer upon layer of materials onto substrates. In food processing industry, spray drying is used very often to remove moisture and produce dry packaged foods and powders. Sprays are also widely used in pharmaceutical processes, and oral or nasal sprays are used by millions of people every day. In combustion applications, liquid fuel sprays are necessary for the efficient and effective combustion of liquid fuels and the control of pollutant emissions in power generation and propulsion systems.

In reality, almost every application has its own specific requirement of spray characteristics. This makes the design of atomizers and the organization of atomization processes extremely important in order to produce sprays with the required specific spray angles, shapes and penetration as well as specified distributions of drop size, velocity, number density and liquid flux. There are, basically, three types of atomization: pressure, rotary and twin-fluid atomization. Pressure atomization is achieved simply by forcing the pressurized liquid through an orifice, and a pressure atomizer is simple in construction and hence inexpensive as well. The disadvantage of pressure atomization is its narrow operating range. This type of atomization is extensively used in our daily life, such as hair and detergent sprays, and also in industry such as in diesel engines, jet engines and ramjets. As for a rotary atomization, rotating and speed controlling devices are required to generate the rotation motion for the liquid to be atomized. This type of atomization is capable of handling slurries and often applied in spray drying and cooling systems.

The third category is so-called twin-fluid atomization, that is the focus of this thesis. In general, the relative motion between the two fluids is utilized to disintegrate the liquid to be atomized, and the other fluid can be a gas, its own vapor, or even another liquid which is immiscible with the atomizing liquid. In practice, most twin-

fluid atomization belongs to the air-assist or airblast atomization. The main difference between the two is that the air-assist atomization use relatively small quantities of air flowing at very high velocities (usually sonic), whereas the airblast atomization utilizes large amounts of air flowing at much lower velocities. In combustion systems, both air-assist and airblast atomization are ideally suited for dispersing liquid fuels, and the most common approach is that the liquid is first spread into cylindrical or annular sheet called prefilming, and then exposed to high velocity air streams on either one side or both sides of the sheet. As a result, an annular liquid sheet or jet is formed with two gas-liquid interfaces of finite radii of curvature. Such a liquid jet is unstable against any disturbances, even infinitesimally small ones, and the instability is manifested through the onset and growth of unstable waves propagating downstream. When the amplitude of the unstable waves exceeds a certain critical value, the continuous liquid jet breaks up into discreet ligaments and then individual droplets.

Twin-fluid atomization is of significant fundamental and practical importance because of its extensive applications in pharmaceutical and chemical processing, spray drying operations, power generation and propulsion systems. The formation and characteristics of sprays are strongly affected by the breakup process of the annular liquid jets.

Therefore, the development and growth of unstable waves on the annular liquid jet subject to inner and/or outer gas streams are investigated in this thesis theoretically by using the linear instability analysis, and experimentally by using the photographic and video-graphic techniques. The resulting spray characteristics such as the distribution of droplet size, velocity, number density and liquid flux are measured by Particle Dynamics Analyzer (PDA). The PDA, based on the light scattering interferometry and phase Doppler principle, is a time-averaged, spatial-resolved and non-intrusive

instrument. Hence, it is a recognized state-of-art instrument ideally suited for spray characterization.

1.1 Scope and Objectives

The present work investigates interfacial instability of an annular viscous liquid jet subject to internal and/or external gas streams and the characteristics of the resulting sprays. In the first part of the thesis, a linear instability analysis of the liquid jet is performed. The effects of various parameters such as finite curvature, liquid viscosity, surface tension, liquid and gas density on the jet breakup processes are examined quantitatively by solving the dispersion relations numerically.

In the second part, an experimental investigation is carried out for the formation and the characteristics of sprays from the annular liquid jet disintegration. Photographic technique is used to assess the jet breakup characteristics such as dominant growth rate and wave length of the unstable surface waves and jet breakup length. The measured data from the photographs taken are compared with the predictions by the linear instability theory. In order to study atomization mechanism of hollow-cone sprays formed by twin-fluid atomizers, an Phase Doppler Particle Analyzer is adopted to measure drop sizes and velocities. Of special interest are spatial distributions of the drop axial velocity and size as well as the effects of liquid and gas flow rates on the drop velocity and size.

PART I: LINEAR INSTABILITY ANALYSIS

Chapter 2

Introduction

In this chapter, classic linear stability theory or small disturbance theory in hydrodynamics is introduced starting from some basic concepts for the theory, mathematical procedure involved in stability or instability analysis, and finally the dispersion relation which governs the characteristics of unstable wave evolution.

2.1 Basic Concepts

The hydrodynamic equations, in spite of their complexity, allow some simple patterns of flow as stationary solutions. However, these patterns of flow can be realized only for certain ranges of the parameters characterizing them. Outside these ranges, they cannot be observed in real hydrodynamic systems because of their inherent instability, in another word, their inability to sustain themselves against small perturbations to which any physical system is subject. Then the question is whether the permissible pattern of flow is stable or not when it is disturbed, even slightly. There are three possible responses: the disturbance may gradually damp such that the flow system

returns to its original state: the disturbance may persist with similar magnitude or oscillate with time: the disturbance may grow in amplitude such that the flow system progressively departs away from its initial state and never reverts to it. These three responses are named (asymptotically) **stable**, **neutrally stable**, and **unstable**, respectively. A system must be considered as unstable even if there is only **one** particular disturbance with respect to which it is unstable. On the other hand, a system can not be considered as stable unless it is stable with respect to **every** possible disturbance to which it can be subject. Among these three classes of states, the neutral state which separates the stable from unstable states is also called **marginal state** and is always one of the prime objects of hydrodynamic stability studies.

2.2 Small Disturbance Theory

Small Disturbance Theory is a theory used to study the instability of a hydrodynamic flow system by applying small disturbances to the base flow and then observing whether the disturbed flow is stable, neutrally stable or unstable. For a given hydrodynamic system, the base flow is first obtained from the governing equations of hydrodynamics. Then the base flow is assumed to be disturbed by small (infinitesimal) disturbances, and the equations governing the disturbed flow are obtained from the governing equations of hydrodynamics. By linear stability theory, all terms which involve higher orders than the first order of the disturbances are neglected, and only the linear terms of the disturbance are retained. For non-linear stability theory, the finite amplitudes of the disturbances are allowed. The evolution of disturbances are then followed.

The mathematical procedure involved in linear instability analysis is now almost standardized as listed below [3]:

(a) Select a base flow

(b) Add an infinitesimal disturbance to the base flow

(c) Find the disturbance equations

(d) Linearize the obtained disturbance equations

(e) Solve the linearized equations by assuming a wave form solution (e.g. a traveling wave form)

(f) Solve for the eigenvalue problem, i.e., find the dispersion relation

(g) Interpret the stability conditions and draw a chart showing the neutral curves and growth rates, find the maximum wave growth rate or dominant wave number from the dispersion relation.

As for the linear stability analysis for a steady simple base flow, the disturbance (or solution) is typically assumed in the form of normal mode, i.e., $\exp[i(\alpha z - \Omega t)]$. This is because any disturbance can be resolved into independent components or modes in the form of $\exp[i(\alpha z - \Omega t)]$, and for a linear system each mode can be treated separately. The solutions obtained in this manner are often called **normal mode** solutions.

2.3 Linear Instability Analysis

In linear instability analyses, the dispersion relations for liquid or gas jets are usually solved to determine the values of Ω and the spatial variations of corresponding wave components α as eigenvalues or eigenfunctions. Here, Ω and α could all be complex numbers as $\Omega = \Omega_r + i\Omega_i$ and $\alpha_r + i\alpha_i$. However in some cases, either their real parts

or imaginary parts may vanish. Depending on the signs of Ω and α satisfying the dispersion relations, three modes of instability may be possible for liquid or gas jets, which are **temporal**, **convective** and **absolute** instability.

Corresponding to the wave form, $\exp[i(\alpha z - \Omega t)]$, a **temporal instability** mode would exists if α is real or $\alpha_i = 0$ and Ω is complex with $\Omega_i > 0$ representing the temporal growth rate of a certain disturbance (of wave number α_r). In this case, the disturbance will grow exponentially with time until it is so large that nonlinearity becomes significant. The disturbance is, therefore, said to be **unstable**. If $\Omega_i = 0$, it means that the disturbance stays as it is, and it is said to be **neutrally stable**. However if $\Omega_i < 0$, the disturbance is damped exponentially until its complete disappearance, which is said to be (asymptotically) **stable**.

Usually, there will be a critical value of the wave number α_r, which separates the unstable from the stable region of disturbance wavenumbers. That is $\Omega_i = 0$ at such a critical value of the wave number α_r often named **stability limit**. Within the unstable region, there usually exists a particular mode of disturbance whose growth rate Ω_i reaches a maximum. This mode is termed the mode of maximum instability or fastest growing mode or **dominant mode**. It is this dominant unstable wave mode that could actually be observed in reality if all modes of disturbances have comparable initial magnitude.

In practice, a disturbance will be not only one normal mode, but usually some superposition of many normal modes determined by the nature of the initial disturbances. For an unstable system, a localized initial disturbance not only will grow, but also may propagate and spread, with each unstable component growing at its own rate and moving at its own phase velocity. Generally, the space-time evolution of a localized initial disturbance in an unstable system could be classified into two physically distinct categories:

(a) the disturbance can grow as its center propagates away from its origin, such that eventually at a fixed point in space the disturbance decays with time. This is called **convective instability**;

(b) the growing disturbance can engulf more and more of space as time goes on, such that eventually at every spatial location the disturbance grows. This is referred to as **absolute instability**.

To determine whether absolute and/or convective instabilities exist for a particular system with disturbances in the form of $A_0 \exp[i(\alpha z - \Omega t)]$, the analysis usually starts from the dispersion relation. According to Briggs [4] and Bers [5], it is essential to search for pinch points (α_0, Ω_0) on the complex α-plane with $\alpha_{0,i} < 0$ and $\Omega_{0,i} > 0$ for absolute instabilities. Notice that one pinch point with $\Omega_{0,i} > 0$ for an absolute instability represents one normal mode, the normal mode with the largest positive $\Omega_{0,i}$ is the maximum instability mode which dominates the time-asymptotic response of the system.

The pinch points (α_0, Ω_0) may have the other two possibilities. One is that $\Omega_{0,i} = 0$ stands for a critical state which separates absolute from convective instability. The other is $\Omega_{0,i} < 0$, meaning that disturbances at every spatial location will die away with time, such that the original unperturbed state retains. This indicates that there are no absolute instabilities. However, spatially growing waves or convective instability may exist. Since convectively unstable waves possess the character of a **wavepacket** rather than a single wave, it is the wavepacket that propagates and spreads out while it grows. The method to find convective instabilities is to solve the dispersion relation for $\alpha(\Omega_r)$ with $\Omega_i = 0$. If α_i solved is of negative values, the disturbances grow and propagate through the space in the positive z direction, as it is usually set in the direction of jet flow originated from a nozzle, and vice versa.

The differences among temporal, absolute and convective instability modes are summarized in Appendix A.

Chapter 3

Literature Review

The instability and breakup process of liquid jets have been the research subject in connection with liquid atomization for more than a century. Since Rayleigh [6, 7, 8] carried out the first stability analysis for cylindrical liquid columns in vacuum, many studies have contributed to the instability analyses of jets of various cross sectional shapes under different flow conditions (see Appendix C). Most of the earlier studies focused on temporal instability analyses. For example, for a cylindrical liquid jet, the first stability analysis by Rayleigh was temporal one [6, 7, 8]. Then Weber [9], Sterling and Sleicher [10], Lin and Kang [11] and many others [12] also conducted temporal analyses by taking into account the effects of different parameters such as gas density, liquid velocity and viscosity. The spatial instability was first introduced to jet instability studies by Keller et al. [13] for a cylindrical liquid jet, although the idea of spatially amplifying disturbances has been known in many other problems in hydrodynamics [14, 15, 16, 17] and plasma instability [4, 5].

The instability and breakup of annular liquid sheets, which are often referred to as annular liquid jets as well, are of significant scientific and practical importance, and extensive studies have been conducted in the past in relation to the formation of

spherical shells [18, 19, 20, 21], water bells [22, 23, 24] and acoustical barriers [25], and only a limited number of studies are related to liquid atomization and spray application [26, 27]. For a given liquid and annular nozzle, the annular jet converges, at relatively low velocities, to become an ordinary liquid jet some distance downstream of the nozzle primarily due to the capillary effects. The geometric configuration and instability mechanism of annular jets [24, 28] and the related water bells [23] as well as compound jets [29, 30] have been studied in great details, including the effects of gravity [23], surface tension [24], buoyancy [31] and pressure (or velocity) differences [22, 24] between the inner and outer gas regions.

At relatively high liquid velocities, unstable waves develop at the two interfaces of an annular liquid jet. The growth of these waves eventually leads to the breakup of the jet into ligaments and finally individual droplets. This process of the jet disintegration is often employed for the formation of liquid sprays [26, 27]. One typical type of sprays, hollow-cone sprays formed from conical liquid sheet disintegration, has been extensively used in practical applications, ranging from pharmaceutical and chemical processes, spray drying operations to power generation and propulsion systems. Such a conical liquid sheet involves three important characteristics. First, the liquid sheet is very thin. Second, it has two interfaces with finite radius or curvature. And last its thickness changes with the downstream distance. To fully understand the mechanism of hollow-cone spray formation, the instability of such a conical liquid sheet has to be investigated. However, because of the complexity of the problem, such a liquid sheet has been conventionally modeled by a constant (but very small) thickness with infinite radius, which is a plane liquid sheet case [32, 33, 34, 35, 36, 37, 38]. The instability and breakup characteristics of thin and radically moving liquid sheets whose thickness reduces as the distance from the nozzle increases have also been studied [39, 40]. In order to assess the effects of finite curvature on the sheet instability processes,

annular liquid sheets with well-defined curvature need to be studied. This is one of the motivations for the present work. Another motivation of this work is that an annular liquid sheet can be regarded as a generalization including three well-known limiting cases, a cylindrical liquid jet, thin planar liquid sheet and cylindrical gas jet (Appendix C). The investigations on the annular sheet instability is, therefore, necessary and essential for the understanding of liquid jet disintegration processes.

3.1 Temporal Instability

A few studies have been carried out to investigate the breakup process of annular liquid jets based on **temporal instability** analyses. As summarized in Table B.1, Crapper et al. [41] analyzed theoretically the instability of an inviscid annular liquid sheet moving in an inviscid stationary gas medium. The temporal wave growth rates were obtained for two unstable wave modes, para-varicose (symmetric), and para-sinuous (anti-symmetric) with the approximation of very thin liquid sheets. Meyer and Weihs [42] investigated the capillary instability of a static viscous liquid sheet in a moving gas stream with a particular type of disturbances by assuming the amplitude ratio of initial disturbances at the outer interface to that at the inner interface equal to the ratio of the inner to outer radii of the jet. The instability of a stationary viscous annular liquid sheet with unequal gas velocities for the inner and outer gas streams was formulated by Lee and Chen [43]. Two dispersion relations corresponding to each interface were derived. However, only cases for inviscid liquids were theoretically examined in their study. Obviously, in the previous works, either stationary liquid or gas was considered. However in twin-fluid atomization, the velocity of air streams on one side [43, 20] or both sides [44, 45] of liquid sheets is very important for the breakup process of the liquid sheets. Using high-velocity gas can promote the breakup

processes of the liquid sheets and improve atomization performance. On the other hand, since the Galilean transformation of coordinate often changes the characteristics of the temporal-spatial evolution of unstable waves [5, 46], the absolute velocities of both liquid and gas should be taken into account.

Therefore as one part of this work, a temporal instability analysis is carried out for an annular viscous liquid jet exposed to both inner and outer gas streams of unequal velocities [47, 48]. The general forms of the dispersion relation and the equations for the amplitude ratio of initial disturbances at the two interfaces are derived by considering absolute velocity of each flow. The effects of geometrical and flow parameters are examined based on numerical results obtained from the dispersion relations.

3.2 Absolute and Convective Instability

There are very limited previous works on absolute and convective instability analyses for liquid jets or sheets. Especially for annular liquid sheets or jets, there is no any work published so far. The first work by Keller et al. [13] was for a cylindrical liquid jet. For the first time, Keller et al. pointed out that the temporal instability theory implies that the disturbance wave grows in amplitude everywhere along the jet, even in the immediate neighborhood of a nozzle, which is contrary to the experimental observations [33, 49, 35]. The instability and breakup of a liquid jet or sheet discharged from a nozzle was due to spatially rather than temporally growing disturbances. They also found that the temporal and spatial instability at sufficiently large Weber numbers are related by Gaster's relation [50]. Leib and Goldstein studied the absolute instability of a cylindrical inviscid [51] and viscous liquid jet [52], and showed that the jet is absolutely unstable for Weber numbers below a certain critical

value and is convectively unstable when the Weber number is above the critical value. The effect of the ambient gas density on the absolute instability of cylindrical liquid jets was studied by Lin and Lian [53]. Spatial mode of instability was also identified for plane liquid sheets, as Lin et al. [54] did in their studies for a viscous liquid sheet in a stationary gas medium. They reported that the sinuous mode of disturbances is neutrally stable below a critical Weber number of one , and in the sense of Briggs [4] and Bers [5] they termed it as pseudo-absolute instability. For sinuous mode at Weber numbers higher that the critical value of one and for varicose mode at any Weber number, convective instability exists in the system for a non-zero gas density. Li [37] further analyzed the problem and pointed out that liquid viscosity plays a dual role of stabilizing and destabilizing for sinuous mode at low Weber numbers, while for varicose mode and sinuous mode at higher Weber numbers, it is always stabilizing. The same problem has also been addressed by Ibrahim [55] and the subject has been reviewed by Li [37].

As a part of this work, absolute and convective instability are reported for an annular viscous liquid jet with its inner and outer sides exposed to inviscid gas streams of unequal velocities [56]. An efficient mesh-searching method over the complex plane of wave number is used to determine the absolute modes of instability [57]. The effects of geometrical and various flow parameters are examined. It is found that both absolute and convective instability exist for para-sinuous and -varicose modes under certain flow conditions. For para-sinuous mode, the annular liquid jet with an inner gas moving at relatively small velocity can have convective or absolute instability depending on specific flow conditions. However, the jet has only absolute instability if the inner gas is either stationary or moves at sufficiently large velocity. Para-sinuous unstable waves outgrow para-varicose ones, and hence dominate the jet instability according to both absolute and convective instability analysis. The liquid viscosity

has a simple stabilizing effect on the jet instability while the gas inertial force shows fairly complex influence on the absolute instability of the jet. The convective growth rates for various inner gas velocities indicate that not only the velocity difference between, but also the absolute velocity of the liquid and gas, determines the jet breakup process.

Chapter 4

Linear Instability Analysis

An annular liquid jet is formed by discharging liquid from an annular nozzle into surrounding gas streams of unequal velocities as shown in Figure 4.1. The formed annular liquid jet is subjected to the influence of surface tension and the gaseous pressure difference between its two sides. The linear instability for the liquid jet is then studied by imposing small two-dimensional disturbances at the two interfaces based on Small Disturbance Theory as introduced in Chapter 2.

4.1 Basic Assumptions

To simplify the problem, the following assumptions are made without a loss of the main characteristics of the problem:

(a) Both liquid jet and gaseous media are assumed to be incompressible since both velocities are presumed to be small compared to the velocity of the sound;

(b) Surrounding gas is inviscid, but liquid is viscous with constant viscosity μ_ℓ;

(c) Fluid properties such as density ρ_ℓ and ρ_g and surface tension σ are assumed to be constant;

(d) Gravity effect is neglected;

(e) The base liquid and gas flows are semi-infinitely long and axisymmetric with different uniform velocities U_l^*, U_a^*, and U_b^* for the liquid, inner gas and outer gas, respectively, in the axial direction;

(f) Two-dimensional dispersive wave is supposed to propagate in the axial direction.

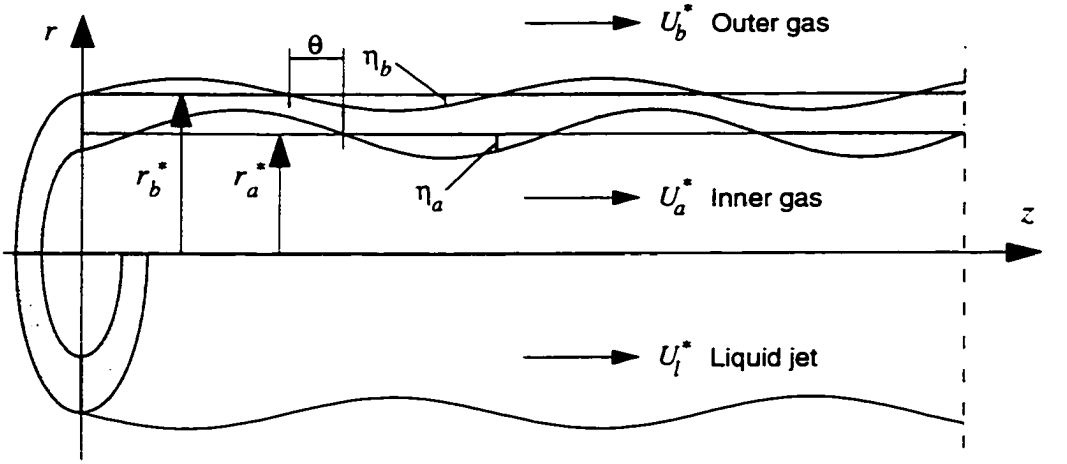

Figure 4.1: Schematic of an annular liquid jet exposed to inner and outer gas streams

4.2 Formulation

Figure 4.1 shows an semi-infinitely long annular liquid jet with inner radius r_a^* and outer radius r_b^*. To derive the dispersion relation and the equation for the amplitude ratio of initial disturbances at two gas-liquid interfaces, two-dimensional infinitesimal disturbances are applied at the two interfaces. Since the gravity is neglected, the

pressure fields for the base flows are constant within the liquid and gas, respectively, and have a jump across the two gas-liquid interfaces, due to the effect of surface tension σ. When disturbances develop in the liquid jet, resulting in the interface deformation and deviation away from its equilibrium configuration, the flow field is disturbed with the perturbed flow velocity $\mathbf{u}$ and pressure p superimposed on the base flow velocity $\bar{\mathbf{U}}$ and pressure $\bar{P}$. Then in a cylindrical coordinate system (z, r, θ), the perturbed flow fields become:

$$\mathbf{U}_n = \bar{\mathbf{U}}_n + \mathbf{u}_n, \quad \mathbf{u}_n = (u_n, v_n, 0), \quad P_n = \bar{P}_n + p_n \tag{4.1}$$

where the subscript $n = \ell, a$ and b correspond to the liquid jet, the inner and outer gas streams, respectively. The base flow quantities are given by:

$$\bar{\mathbf{U}}_\ell = (U_\ell^*, 0, 0), \quad \bar{\mathbf{U}}_a = (U_a^*, 0, 0), \quad \bar{\mathbf{U}}_b = (U_b^*, 0, 0)$$
$$\bar{P}_\ell = \bar{P}_a - \sigma/r_a^* = \bar{P}_b + \sigma/r_b^*$$

The equations governing the motion of the perturbed flow are the continuity equation for incompressible flow and balance of momentum, which become, upon linearization,

$$\nabla \cdot \mathbf{u}_n = 0 \tag{4.2}$$

$$\rho_n \left(\frac{\partial}{\partial t} + U_n^* \frac{\partial}{\partial z} \right) \mathbf{u}_n = -\nabla p_n + \mu_n \nabla^2 \mathbf{u}_n \tag{4.3}$$

The boundary conditions that the solutions of the above governing equations have to satisfy are the kinematic and dynamic conditions at the inner and outer interfaces, which are represented by $r = r_a^* + \eta_a(z, t)$ and $r = r_b^* + \eta_b(z, t)$, respectively. In linear instability theory, these conditions need not be applied at the disturbed liquid-gas interfaces. Rather, they can be linearized in the same manner as done above for the governing equations. Then the linearized boundary conditions can be applied at the

unperturbed interfaces. Because the interfaces are material surfaces, the kinematic boundary conditions are

$$\begin{aligned} v_\ell &= \frac{\partial \eta_a}{\partial t} + U_\ell^* \frac{\partial \eta_a}{\partial z} \\ v_a &= \frac{\partial \eta_a}{\partial t} + U_a^* \frac{\partial \eta_a}{\partial z} \end{aligned} \tag{4.4}$$

at $r = r_a^*$ and

$$\begin{aligned} v_\ell &= \frac{\partial \eta_b}{\partial t} + U_\ell^* \frac{\partial \eta_b}{\partial z} \\ v_b &= \frac{\partial \eta_b}{\partial t} + U_b^* \frac{\partial \eta_b}{\partial z} \end{aligned} \tag{4.5}$$

at $r = r_b^*$.

The dynamic condition implies that the shear stress must vanish at the interfaces because of the inviscid assumption for the gas phase, and normal stresses across the interfaces must be continuous with allowance for the effect of surface tension σ. Mathematically, these dynamic conditions can be expressed as follows:

$$\mu_\ell \left(\frac{\partial u_\ell}{\partial r} + \frac{\partial v_\ell}{\partial z} \right) = 0 \qquad (\text{at } r = r_a^* \text{ and } r = r_b^*) \tag{4.6}$$

$$p_a - p_\ell + 2\mu_\ell \frac{\partial v_\ell}{\partial r} = -\sigma \left(\frac{\eta_a}{r_a^{*2}} + \frac{\partial^2 \eta_a}{\partial z^2} \right) \quad (\text{at } r = r_a^*) \tag{4.7}$$

$$p_b - p_\ell + 2\mu_\ell \frac{\partial v_\ell}{\partial r} = \sigma \left(\frac{\eta_b}{r_b^{*2}} + \frac{\partial^2 \eta_b}{\partial z^2} \right) \quad (\text{at } r = r_b^*) \tag{4.8}$$

Further, in the ambient gas phase, the effects of disturbances should physically remain bounded, whether it is at the centerline or far away from the liquid jet. That is,

$$\mathbf{u}_a \text{ and } p_a \text{ bounded as } r \to 0 \tag{4.9}$$

$$\mathbf{u}_b \text{ and } p_b \text{ bounded as } r \to \infty \tag{4.10}$$

The solutions to the governing equations are sought in terms of the normal mode in the following form:

$$(\mathbf{u}_n, p_n, \eta_a, \eta_b) = [\tilde{\mathbf{u}}_n(r), \tilde{p}_n(r), \epsilon_a, \epsilon_b] \exp\{i(\alpha z - \Omega t)\} \tag{4.11}$$

where $n = \ell, a$ and b, ϵ_a and ϵ_b are the amplitudes of initial disturbances at the inner and outer interfaces, and are regarded to be much smaller than the inner and outer radius as well as the thickness of the annular liquid jet. The real part α_r of α is axial wavenumber of the disturbance and is related to the disturbance wavelength λ by the relation $\alpha_r = 2\pi/\lambda$. The imaginary part α_i stands for the rate of growth or decay of the disturbance through space. The imaginary part Ω_i of Ω represents the rate of growth or decay of the disturbance with time, the real part Ω_r is equal to 2π times the disturbance frequency, and $-\Omega_r/\alpha$ represents the wave propagation velocity of the disturbance.

Substituting Eq. (4.11) into the governing differential equations, Eqs. (4.2) and (4.3), yields the required general solutions with unknown integration constants which can be determined by using the boundary conditions, Eqs. (4.4), (4.5), (4.6) and two limiting conditions Eqs. (4.9) and (4.10). The solutions are

$$\begin{aligned} u_a &= -\frac{\epsilon_a I_0(\alpha r)}{I_1(\alpha r_a^*)}(\alpha U_a^* - \Omega)e^{i(\alpha z - \Omega t)} \\ v_a &= \frac{i\epsilon_a I_1(\alpha r)}{I_1(\alpha r_a^*)}(\alpha U_a^* - \Omega)e^{i(\alpha z - \Omega t)} \\ p_a &= \frac{\epsilon_a \rho_g I_0(\alpha r)}{\alpha I_1(\alpha r_a^*)}(\alpha U_a^* - \Omega)^2 e^{i(\alpha z - \Omega t)} \end{aligned} \tag{4.12}$$

for the inner gas flow,

$$\begin{aligned} u_b &= \frac{\epsilon_b K_0(\alpha r)}{K_1(\alpha r_b^*)}(\alpha U_b^* - \Omega)e^{i(\alpha z - \Omega t)} \\ v_b &= \frac{i\epsilon_b K_1(\alpha r)}{K_1(\alpha r_b^*)}(\alpha U_b^* - \Omega)e^{i(\alpha z - \Omega t)} \\ p_b &= -\frac{\epsilon_b \rho_g K_0(\alpha r)}{\alpha K_1(\alpha r_b^*)}(\alpha U_b^* - \Omega)^2 e^{i(\alpha z - \Omega t)} \end{aligned} \tag{4.13}$$

for the outer gas flow, and

$$\begin{aligned} u_\ell &= \frac{1}{r}\frac{\partial \psi}{\partial r} = [A_1 S I_0(Sr) - A_2 S K_0(Sr) + A_3 \alpha I_0(\alpha r) - A_4 \alpha K_0(\alpha r)] e^{i(\alpha z - \Omega t)} \\ v_\ell &= -\frac{1}{r}\frac{\partial \psi}{\partial z} = -i\alpha e^{i(\alpha z - \Omega t)} [A_1 I_1(Sr) + A_2 K_1(Sr) + A_3 I_1(\alpha r) + A_4 K_1(\alpha r)] \\ p_\ell &= -\rho_\ell(\alpha U_\ell^* - \Omega)[A_3 I_0(\alpha r) - A_4 K_0(\alpha r)] e^{i(\alpha z - \Omega t)}. \end{aligned} \tag{4.14}$$

for the liquid flow, where

$$\begin{aligned} A_1 &= \frac{2i\alpha\nu_\ell[\epsilon_b K_1(Sr_a^*) - \epsilon_a K_1(Sr_b^*)]}{[I_1(Sr_a^*)K_1(Sr_b^*) - I_1(Sr_b^*)K_1(Sr_a^*)]} \\ A_2 &= \frac{2i\alpha\nu_\ell[\epsilon_a I_1(Sr_b^*) - \epsilon_b I_1(Sr_a^*)]}{I_1(Sr_a^*)K_1(Sr_b^*) - I_1(Sr_b^*)K_1(Sr_a^*)} \\ A_3 &= \frac{i\nu_\ell(S^2+\alpha^2)[\epsilon_a K_1(\alpha r_b^*) - \epsilon_b K_1(\alpha r_a^*)]}{\alpha[I_1(\alpha r_a^*)K_1(\alpha r_b^*) - I_1(\alpha r_b^*)K_1(\alpha r_a^*)]} \\ A_4 &= \frac{i\nu_\ell(S^2+\alpha^2)[\epsilon_b I_1(\alpha r_a^*) - \epsilon_a I_1(\alpha r_b^*)]}{\alpha[I_1(\alpha r_a^*)K_1(\alpha r_b^*) - I_1(\alpha r_b^*)K_1(\alpha r_a^*)]}. \end{aligned}$$

Substituting the above solutions of each flow, Eqs. (4.12), (4.13) and (4.14), into the dynamic boundary conditions at the two interfaces, Eqs. (4.7) and (4.8), leads to two equations with two unknowns ϵ_a and ϵ_b. Since these two equations are homogeneous, the coefficients of the equations must satisfy a condition for non-trivial solutions to exist. That is the determinant of the coefficient matrix must vanish, which gives the following dispersion relation between Ω and α.

$$\begin{aligned} &\left\{(S^2+\alpha^2)^2\Delta_4\Delta_1 - 4\alpha^3 S\Delta_3\Delta_6 - \frac{2i\alpha}{r_a^*\nu_\ell}(\alpha U_\ell^* - \Omega)\right. \\ &\left. + \frac{1}{\nu_\ell^2}\left[\frac{\alpha\sigma}{\rho_\ell}\left(\frac{1}{r_a^{*2}} - \alpha^2\right) + \frac{\rho_g}{\rho_\ell}\frac{I_0(\alpha r_a^*)}{I_1(\alpha r_a^*)}(\alpha U_a^* - \Omega)^2\right]\right\} \\ &\times\left\{(S^2+\alpha^2)^2\Delta_4\Delta_2 - 4\alpha^3 S\Delta_3\Delta_5 + \frac{2i\alpha}{r_b^*\nu_\ell}(\alpha U_\ell^* - \Omega)\right. \\ &\left. + \frac{1}{\nu_\ell^2}\left[\frac{\alpha\sigma}{\rho_\ell}\left(\frac{1}{r_b^{*2}} - \alpha^2\right) + \frac{\rho_g}{\rho_\ell}\frac{K_0(\alpha r_b^*)}{K_1(\alpha r_b^*)}(\alpha U_b^* - \Omega)^2\right]\right\} \\ &- \left[4\alpha^3\Delta_3 - \frac{(S^2+\alpha^2)^2}{\alpha}\Delta_4\right]^2 \frac{1}{r_a^* r_b^*} = 0 \end{aligned} \tag{4.15}$$

The relation between the wave amplitudes at the inner and outer surface, as the part of the solution, is expressed as:

$$\frac{\epsilon_a}{\epsilon_b} = \frac{G_3}{aG_4} \tag{4.16}$$

$$\begin{aligned} G_3 &= -4\alpha^3\Delta_3 + \frac{(S^2+\alpha^2)^2}{\alpha}\Delta_4 \\ G_4 &= (S^2+\alpha^2)^2\Delta_4\Delta_1 - \frac{2i\alpha}{r_a^*\nu_\ell}(\alpha U_\ell^* - \Omega) - 4\alpha^3 S\Delta_3\Delta_6 \\ &\quad + \frac{\alpha\sigma}{\rho_\ell\nu_\ell^2}(\frac{1}{r_a^{*2}} - \alpha^2) + \frac{\rho_g}{\rho_\ell\nu_\ell^2}\frac{I_0(\alpha r_a^*)}{I_1(\alpha r_a^*)}(\alpha U_a^* - \Omega)^2 \end{aligned}$$

Or,

$$\frac{\epsilon_b}{\epsilon_a} = \frac{G_5}{bG_6} \tag{4.17}$$

$$\begin{aligned} G_5 &= -4\alpha^3\Delta_3 + \frac{(S^2+\alpha^2)^2}{\alpha}\Delta_4 \\ G_6 &= (S^2+\alpha^2)^2\Delta_4\Delta_2 + \frac{2i\alpha}{r_b^*\nu_\ell}(\alpha U_\ell^* - \Omega) - 4\alpha^3 S\Delta_3\Delta_5 \\ &\quad + \frac{\alpha\sigma}{\rho_\ell\nu_\ell^2}(\frac{1}{r_b^{*2}} - \alpha^2) + \frac{\rho_g}{\rho_\ell\nu_\ell^2}\frac{K_0(\alpha r_b^*)}{K_1(\alpha r_b^*)}(\alpha U_b^* - \Omega)^2 \end{aligned}$$

where, the dimensional variables are α and Ω, wave number and frequency: U_ℓ^*, U_a^* and U_b^*, the velocities of liquid jet, inner gas and outer gas streams: ρ_ℓ and ρ_g, liquid and gas density: r_a^* and r_b^*, inner and outer radius of two interfaces: σ, surface tension of liquid and gas: ν_ℓ, kinematic liquid viscosity: $S = \sqrt{\alpha^2 + \frac{i(\alpha U_\ell^* - \Omega)}{\nu_\ell}}$: I and K, modified first and second kind Bessel functions: and

$\Delta_1 = I_0(\alpha r_a^*)K_1(\alpha r_b^*) + K_0(\alpha r_a^*)I_1(\alpha r_b^*)$:

$\Delta_2 = I_0(\alpha r_b^*)K_1(\alpha r_a^*) + K_0(\alpha r_b^*)I_1(\alpha r_a^*)$:

$\Delta_3 = [I_1(Sr_a^*)K_1(Sr_b^*) - I_1(Sr_b^*)K_1(Sr_a^*)]^{-1}$:

$\Delta_4 = [I_1(\alpha r_a^*)K_1(\alpha r_b^*) - I_1(\alpha r_b^*)K_1(\alpha r_a^*)]^{-1}$:

$\Delta_5 = I_0(Sr_b^*)K_1(Sr_a^*) + K_0(Sr_b^*)I_1(Sr_a^*)$:

$\Delta_6 = I_0(Sr_a^*)K_1(Sr_b^*) + K_0(Sr_a^*)I_1(Sr_b^*)$:

4.3 Dimensionless Forms of Dispersion Relations

The dimensional dispersion relation, Eq. (4.15), and initial amplitude ratios at two gas-liquid interfaces, Eqs. (4.16) and (4.17), for annular liquid jets are necessary to be in non-dimensional forms for further numerical analyses. The dimensionless forms are presented in the following section. As a partial check for the equations derived above, the dimensionless forms of dispersion relations for three limiting case (see Appendix C) of plane liquid sheets, cylindrical gas jets and cylindrical liquid jets are retrieved from that for annular liquid jets and also presented below.

4.3.1 Annular Liquid Jets

The dimensional variables in Eq.(4.15) are non-dimensionalized as follows:

(a) Length scale is denoted by r_h, which could be one of three choices- half sheet thickness $(r_b^* - r_a^*)/2$, inner r_a^* and outer radius r_b^* of annular sheet

(b) Velocity scale is denoted by U_h^*, which could be one of three choices- liquid jet U_ℓ^*, inner U_a^* and outer gas stream velocity U_b^*

(c) Time (t) is normalized by (r_h/U_h^*)

(d) Wave number $k = \alpha r_h$

(e) Reynolds number, $Re = U_h^* r_h/\nu_\ell$

(f) Weber number, $We = \rho_\ell U_h^{*2} r_h/\sigma$

(g) $s = S r_h = \sqrt{k^2 + iRe(kU_\ell - \omega)}$

(h) Wave frequency, $\omega = \Omega r_h/U_h^*$

(i) The geometric sizes, r_a^* and r_b^*, are normalized by r_h, i.e. $r_a = r_a^*/r_h$, $r_b = r_b^*/r_h$

(j) Density ratio, $\rho = \rho_g/\rho_\ell$.

Substituting the above non-dimensional variables into Eq. (4.15) and times both sides of the equation by r_h^4, we have:

$$\begin{aligned}
&\left\{(s^2+k^2)^2\Delta_1\Delta_4 - 4k^3s\Delta_3\Delta_6 + \left[\frac{k}{We}\left(\frac{1}{r_a^2}-k^2\right)\right.\right. \\
&\left.\left. +\rho(kU_a-\omega)^2\frac{I_0(kr_a)}{I_1(ka)}\right]Re^2 - \frac{2ik}{r_a}Re(kU_\ell-\Omega)\right\} \\
&\times\left\{(s^2+k^2)^2\Delta_2\Delta_4 - 4k^3s\Delta_3\Delta_5 + \left[\frac{k}{We}\left(\frac{1}{r_b^2}-k^2\right)\right.\right. \\
&\left.\left. +\rho(kU_b-\omega)^2\frac{K_0(kr_b)}{K_1(kr_b)}\right]Re^2 + \frac{2ik}{r_b}Re(kU_\ell-\omega)\right\} \\
&-\frac{1}{k^2r_ar_b}\left[(s^2+k^2)^2\Delta_4 - 4k^4\Delta_3\right]^2 = 0
\end{aligned} \tag{4.18}$$

The amplitude ratios of the initial disturbances, Eqs. 4.16 and 4.17, at the inner and outer interfaces become:

$$\frac{\epsilon_a}{\epsilon_b} = \frac{4k^3\Delta_3 - (s^2+k^2)^2\Delta_4/k}{r_a\left\{(s^2+k^2)^2\Delta_1\Delta_4 - 4k^3s\Delta_3\Delta_6 + B_a\right\}} \tag{4.19}$$

or

$$\frac{\epsilon_b}{\epsilon_a} = \frac{4k^3\Delta_3 - (s^2+k^2)^2\Delta_4/k}{r_b\left\{(s^2+k^2)^2\Delta_2\Delta_4 - 4k^3s\Delta_3\Delta_5 + B_b\right\}} \tag{4.20}$$

where

$$B_a = Re^2\left[\frac{k}{We}\left(\frac{1}{r_a^2}-k^2\right) + \rho(kU_a-\omega)^2\frac{I_0(kr_a)}{I_1(kr_a)}\right] - \frac{2ik}{r_a}Re(kU_\ell-\omega)$$

$$B_b = Re^2\left[\frac{k}{We}\left(\frac{1}{r_b^2}-k^2\right) + \rho(kU_b-\omega)^2\frac{K_0(kr_b)}{K_1(kr_b)}\right] + \frac{2ik}{r_b}Re(kU_\ell-\omega)$$

Another dimensionless form of dispersion relation, obtained by re-arranging Eq. (4.18), especially for the calculations of absolute instability, are as follows:

$$\begin{aligned}
&\left\{(kU_\ell-\omega)^2-\frac{\rho}{\Delta_1\Delta_4}\frac{I_0(kr_a)}{I_1(kr_a)}(kU_a-\omega)^2\right.\\
&\qquad -2ik(kU_\ell-\omega)\left[2k-\frac{1}{\Delta_1\Delta_4 r_a}\right]\frac{1}{Re}\\
&\left.-\frac{4k^3}{Re^2}\left[k-s\frac{\Delta_3\Delta_6}{\Delta_1\Delta_4}\right]-\frac{k}{We}\left(\frac{1}{{r_a}^2}-k^2\right)\frac{1}{\Delta_1\Delta_4}\right\}\\
&\times\left\{(kU_\ell-\omega)^2-\frac{\rho}{\Delta_2\Delta_4}\frac{K_0(kr_b)}{K_1(kr_b)}(kU_b-\omega)^2\right.\\
&\qquad -2ik(kU_\ell-\omega)\left[2k+\frac{1}{\Delta_2\Delta_4 r_b}\right]\frac{1}{Re}\\
&\left.-\frac{4k^3}{Re^2}\left[k-s\frac{\Delta_3\Delta_5}{\Delta_2\Delta_4}\right]-\frac{k}{We}\left(\frac{1}{{r_b}^2}-k^2\right)\frac{1}{\Delta_2\Delta_4}\right\}\\
&-\left[4k^4\Delta_3-(s^2+k^2)^2\Delta_4\right]^2\frac{1}{k^2Re^4\Delta_1\Delta_2{\Delta_4}^2 r_a r_b}=0
\end{aligned}\tag{4.21}$$

where $s=\sqrt{k^2+iRe(kU_\ell-\omega)}$:

$\Delta_1 = I_0(kr_a)K_1(kr_b)+K_0(kr_a)I_1(kr_b)$:

$\Delta_2 = I_0(kr_b)K_1(kr_a)+K_0(kr_b)I_1(kr_a)$:

$\Delta_3 = [I_1(sr_a)K_1(sr_b)-I_1(sr_b)K_1(sr_a)]^{-1}$:

$\Delta_4 = [I_1(kr_a)K_1(kr_b)-I_1(kr_b)K_1(kr_a)]^{-1}$:

$\Delta_5 = I_0(sr_b)K_1(sr_a)+K_0(sr_b)I_1(sr_a)$:

$\Delta_6 = I_0(sr_a)K_1(sr_b)+K_0(sr_a)I_1(sr_b)$.

The relation for inviscid annular jet can be obtained from Eq. (4.18) with $Re\to\infty$.

$$\begin{aligned}
&\left\{(kU_\ell-\omega)^2\Delta_1-\left[\rho(kU_a-\omega)^2I_0(kr_a)/I_1(kr_a)+k\left(\frac{1}{{r_a}^2}-k^2\right)/We\right]\Delta_4{}^{-1}\right\}\\
&\cdot\left\{(kU_\ell-\omega)^2\Delta_2-\left[\rho(kU_b-\omega)^2K_0(kr_b)/K_1(kr_b)+k\left(\frac{1}{{r_b}^2}-k^2\right)/We\right]\Delta_4{}^{-1}\right\}\\
&\qquad -\frac{(kU_\ell-\omega)^4}{k^2r_ar_b}=0
\end{aligned}\tag{4.22}$$

$$\frac{\epsilon_a}{\epsilon_b}=\frac{(kU_\ell-\omega)^2}{kr_a\left\{(kU_\ell-\omega)^2\Delta_1-\left[\rho(kU_a-\omega)^2)\frac{I_0(kr_a)}{I_1(kr_a)}+k(1/{r_a}^2-k^2)/We\right]\Delta_4{}^{-1}\right\}}\tag{4.23}$$

or

$$\frac{\epsilon_b}{\epsilon_a} = \frac{(kU_\ell - \omega)^2}{kr_b\left\{(kU_\ell - \omega)^2\Delta_2 - \left[\rho(kU_b - \omega)^2\frac{K_0(kr_b)}{K_1(kr_b)} + k(1/r_b{}^2 - k^2)/We\right]\Delta_4{}^{-1}\right\}} \quad (4.24)$$

4.3.2 Asymptotic Relations for Limiting Cases

The asymptotic relations can be obtained for three limiting cases of plane liquid sheet, cylindrical gas jet and cylindrical liquid jet from the dispersion relation for annular liquid sheets by applying appropriate limits of the radius r_a and r_b of two gas-liquid interfaces (see Appendix C).

(a) Plane Liquid Sheet– Approximation of Large Sheet Radii

To obtain the dispersion relation for plane viscous liquid sheets in stationary gaseous environment from Eq. (4.21), let

$$\begin{cases} r_a \to \infty \\ r_b \to \infty \\ r_b - r_a = const. \end{cases}$$

In this case, the half thickness of the liquid sheet, $(r_b{}^* - r_a{}^*)/2$, is chosen as the reference length scale or $r_h = (r_b{}^* - r_a{}^*)/2$. By applying the asymptotic relations for the Bessel functions with large arguments,

$$\begin{aligned} I_0(x) &\to \frac{e^x}{\sqrt{2\pi x}} \\ K_0(x) &\to \sqrt{\frac{\pi}{2x}}e^{-x} \\ I_1(x) &\to \frac{e^x}{\sqrt{2\pi x}} \\ K_1(x) &\to \sqrt{\frac{\pi}{2x}}e^{-x} \end{aligned}$$

where $x = kr_a, sr_a, kr_b$ and sr_b, and approach infinity for finite k and s, we have:

$$\begin{aligned} \Delta_1 = \Delta_2 &\rightarrow \frac{\epsilon^{-2k} + \epsilon^{2k}}{2k\sqrt{r_a r_b}} \\ \Delta_4 &\rightarrow \frac{2k\sqrt{r_a r_b}}{\epsilon^{-2k} - \epsilon^{2k}} \\ \Delta_3 &\rightarrow \frac{2s\sqrt{r_a r_b}}{\epsilon^{-2s} - \epsilon^{2s}} \\ \Delta_5 = \Delta_6 &\rightarrow \frac{\epsilon^{-2s} + \epsilon^{2s}}{2s\sqrt{r_a r_b}} \end{aligned} \tag{4.25}$$

Times Eq. (4.21) by $(\Delta_1\Delta_2\Delta_4{}^2)$, substituting Eqs. (4.25) into the equation, and considering $U_a = U_b = 0$ as well as

$$\begin{aligned} \frac{\epsilon^{-2k} + \epsilon^{2k}}{-\epsilon^{-2k} + \epsilon^{2k}} &= \frac{1}{2}[\tanh(k) + \coth(k)] \\ \frac{\epsilon^{-2s} + \epsilon^{2s}}{-\epsilon^{-2s} + \epsilon^{2s}} &= \frac{1}{2}[\tanh(s) + \coth(s)] \\ \frac{4}{-\epsilon^{-2k} + \epsilon^{2k}} &= \tanh(k) - \coth(k) \\ \frac{4}{-\epsilon^{-2s} + \epsilon^{2s}} &= \tanh(s) - \coth(s) \\ \frac{4 - (\epsilon^{-2k} + \epsilon^{2k})^2}{(\epsilon^{-2k} - \epsilon^{2k})^2} &= -1 \\ \frac{4 - (\epsilon^{-2s} + \epsilon^{2s})^2}{(\epsilon^{-2s} - \epsilon^{2s})^2} &= -1 \\ \frac{(\epsilon^{-2s} - \epsilon^{2s})(\epsilon^{-2k} - \epsilon^{2k}) - 4}{(\epsilon^{-2s} + \epsilon^{2s})(\epsilon^{-2k} + \epsilon^{2k})} &= \frac{1}{2}[\tanh(k)\coth(s) + \coth(k)\tanh(s)] \end{aligned}$$

Eq. (4.21) becomes, after decomposition and re-arranging,

$$\left[(kU_l - \omega) + \frac{2k^2}{iRe}\right]^2 \tanh(k) + \frac{4k^3 s}{Re^2}\tanh(s) + \rho\omega^2 - \frac{k^3}{We} = 0 \tag{4.26}$$

or

$$\left[(kU_\ell - \omega) + \frac{2k^2}{iRe}\right]^2 \coth(k) + \frac{4k^3 s}{Re^2}\coth(s) + \rho\omega^2 - \frac{k^3}{We} = 0 \qquad (4.27)$$

for sinuous and varicose instability mode, respectively.

(b) Cylindrical Gas Jet– Limit of Large Outer Radius

An inviscid gas jet submerged in a moving viscous liquid stream can be retrieved by considering

$$\begin{cases} r_a = const. \\ r_b \to \infty \end{cases}$$

In this case, the inner radius r_a^* is chosen as the reference length scale, i.e., $r_h = r_a^*$ and $r_a = 1$. Then by using the asymptotic relations for the Bessel functions with large arguments,

$$\begin{aligned} I_0(x) &\to \frac{e^x}{\sqrt{2\pi x}} \\ K_0(x) &\to \sqrt{\frac{\pi}{2x}}e^{-x} \\ I_1(x) &\to \frac{e^x}{\sqrt{2\pi x}} \\ K_1(x) &\to \sqrt{\frac{\pi}{2x}}e^{-x} \end{aligned}$$

where $x = kr_b$ and sr_b, and approach infinity for finite k and s.

we have:

$$\begin{aligned} \Delta_1 &\to I_0(k)\sqrt{\frac{\pi}{2kr_b}}e^{-kr_b} + K_0(k)\frac{e^{kr_b}}{\sqrt{2\pi kr_b}} \\ \Delta_2 &\to I_1(k)\sqrt{\frac{\pi}{2kr_b}}e^{-kr_b} + K_1(k)\frac{e^{kr_b}}{\sqrt{2\pi kr_b}} \\ \Delta_4 &\to \left[I_1(k)\sqrt{\frac{\pi}{2kr_b}}e^{-kr_b} - K_1(k)\frac{e^{kr_b}}{\sqrt{2\pi kr_b}}\right]^{-1} \end{aligned}$$

$$
\begin{aligned}
\Delta_3 &\rightarrow \left[I_1(s)\sqrt{\frac{\pi}{2sr_b}}\epsilon^{-sr_b} - K_1(s)\frac{e^{sr_b}}{\sqrt{2\pi sr_b}} \right]^{-1} \\
\Delta_5 &\rightarrow I_1(s)\sqrt{\frac{\pi}{2sr_b}}\epsilon^{-sr_b} + K_1(s)\frac{e^{sr_b}}{\sqrt{2\pi sr_b}} \\
\Delta_6 &\rightarrow I_0(s)\sqrt{\frac{\pi}{2sr_b}}\epsilon^{-sr_b} + K_0(s)\frac{e^{sr_b}}{\sqrt{2\pi sr_b}} \\
\Delta_1\Delta_4 &\rightarrow -\frac{K_0(k)}{K_1(k)} \\
\Delta_2\Delta_4 &\rightarrow -1 \\
\Delta_3\Delta_6 &\rightarrow -\frac{K_0(s)}{K_1(s)} \\
\Delta_3\Delta_5 &\rightarrow -1
\end{aligned}
\tag{4.28}
$$

Multiplying the first factor of the first term in Eq. (4.21) by ($\Delta_1\Delta_4$), the second factor of the first term by ($\Delta_2\Delta_4$) and the second term by ($\Delta_1\Delta_2\Delta_4^2$), Eq. (4.21) will be reduced, after applying Eq. (4.28), to:

$$
\left[(kU_\ell - \omega) - \frac{2ik^2}{Re} \right]^2 + \frac{4k^3 s}{Re^2} + \rho(kU_a - \omega)^2 - \frac{k^3}{We} = 0 \tag{4.29}
$$

or

$$
\begin{aligned}
(kU_\ell - \omega)^2 + \rho(kU_a - \omega)^2 \frac{I_0(k)}{I_1(k)}\frac{K_1(k)}{K_0(k)} - \frac{2ik^2}{Re}\left[2 + \frac{1}{k}\frac{K_1(k)}{K_0(k)} \right](kU_\ell - \omega) \\
- \frac{4k^3}{Re^2}\left[k - s\frac{K_0(s)}{K_1(s)}\frac{K_1(k)}{K_0(k)} \right] + \frac{k(1-k^2)}{We}\frac{K_1(k)}{K_0(k)} = 0
\end{aligned}
\tag{4.30}
$$

Eq.(4.29) represents the classical Kelvin-Helmholtz instability with the effect of surface tension included [38, 58], and is identical to the results for a stationary gas medium over a flowing liquid stream [38].

Equation (4.30) is the limiting form for the para-sinuous mode, and represents the dispersion relation for a gas jet in a moving liquid medium. Clearly it is related to the disturbances at the inner interface. For $\rho = 0$ and $Re \rightarrow \infty$, Eq.(4.30) becomes

$$
(kU_\ell - \omega)^2 = -\frac{k(1-k^2)}{We}\frac{K_1(k)}{K_0(k)} \tag{4.31}
$$

which is identical to the result first given by Rayleigh [8].

(c) Cylindrical Liquid Jet– Limit of Small Inner Radius

A viscous cylindrical liquid jet can be obtained by allowing

$$\begin{cases} r_a \to 0 \\ r_b = const. \end{cases}$$

In this case, the reference length scale r_h is chosen to be the outer radius r_b^*, such that the dimensionless outer radius $r_b = 1$. The dispersion relation, Eq.(4.21), can then be reduced by using the asymptotic relations for the Bessel functions with small arguments. However, since the arguments of the Bessel functions in Eq.(4.21) are either (kr_a) or (sr_a), the asymptotic relations can only be utilized if both s and k remains finite values when $r_a \to 0$. Because $s^2 = k^2 + iRe(kU_\ell - \omega)$, this requirement is satisfied by assuming ω is finite as the inner radius vanishes. As $r_a \to 0$, the asymptotic relations for Bessel functions to be used are:

$$\begin{cases} K_1(x) & \to \frac{1}{x} \\ I_1(x) & \to \frac{x}{2} \\ K_0(x) & \to -ln(x) \\ I_0(x) & \to 1 \end{cases} \tag{4.32}$$

with $x = kr_a$ and sr_a.

By applying the above relations, Eq. (4.32), we have:

$$\begin{cases} \Delta_1 & \rightarrow K_1(k) - \ln(kr_a) I_1(k) \\ \Delta_2 & \rightarrow \frac{I_0(k)}{kr_a} + \frac{kr_a}{2} K_0(k) \\ \Delta_4 & \rightarrow -\frac{kr_a}{I_1(k)} \\ \Delta_1\Delta_4 & \rightarrow 0 \\ \Delta_2\Delta_4 & \rightarrow -\frac{I_0(k)}{I_1(k)} \\ \Delta_3 & \rightarrow -\frac{sr_a}{I_1(s)} \\ \Delta_5 & \rightarrow \frac{I_0(s)}{sr_a} + \frac{sr_a}{2} K_0(s) \\ \Delta_6 & \rightarrow K_1(s) - \ln(sr_a) I_1(s) \\ \Delta_3\Delta_6 & \rightarrow 0 \\ \Delta_3\Delta_5 & \rightarrow -\frac{I_0(s)}{I_1(s)} \end{cases} \tag{4.33}$$

Multiplying the first factor of the first term in Eq. (4.21) by $(r_a^2\Delta_1\Delta_4)$, the second factor of the first term by $(\Delta_2\Delta_4)$ and the second term by $(r_a^2\Delta_1\Delta_2\Delta_4^2)$, Eq. (4.21) will be reduced, after applying Eq. (4.32) and Eq. (4.33) as well as noticing $[r_a \ln(kr_a)]$ and $[r_a \ln(sr_a)]$ vanish as $r_a \rightarrow 0$, to:

$$\begin{aligned} (kU_\ell - \omega)^2 + \rho(kU_b - \omega)^2 \frac{K_0(k)}{K_1(k)} \frac{I_1(k)}{I_0(k)} - \frac{2ik^2}{Re}(kU_\ell - \omega)\left[2 - \frac{I_1(k)}{I_0(k)}\right] \\ - \frac{4k^3}{Re^2}\left[k - s\frac{I_0(s)}{I_1(s)}\frac{I_1(k)}{I_0(k)}\right] + \frac{k(1-k^2)}{We}\frac{I_1(k)}{I_0(k)} = 0 \end{aligned} \tag{4.34}$$

or

$$\begin{aligned} (kU_\ell - \omega)^2 + \rho(kU_b - \omega)^2 \frac{K_0(k)}{K_1(k)} \frac{I_1(k)}{I_0(k)} - \frac{2ik^2}{Re}\left[1 + \frac{I_1'(k)}{I_0(k)}\right](kU_\ell - \omega) \\ - \frac{4k^3}{Re^2}\left[k\frac{I_1'(k)}{I_0(k)} - s\frac{I_1'(s)}{I_1(s)}\frac{I_1(k)}{I_0(k)}\right] + \frac{k(1-k^2)}{We}\frac{I_1(k)}{I_0(k)} = 0 \end{aligned} \tag{4.35}$$

upon re-arranging Eq. (4.34), which is identical to that by Lin and Kang [11] and Sterling [10].

4.4 Computational Algorithm

The dimensionless forms, Eqs. (4.18) and (4.21), of the dispersion relation are solved to yield numerical results for annular liquid jet instability. Each form of the dispersion relation is a complex equation with the fourth order for wave frequency ω. Therefore, the solution is not unique for a given flow condition. Both ω and k in the equation can be complex variables. When ω is complex but k real or $k_i = 0$, the imaginary part ω_i of ω represents temporal growth rate of disturbances. Hence for *temporal instability*, it is to solve complex wave frequencies from Eq. (4.18) for given real wave numbers k_r with $k_i = 0$. In this case, Eq. (4.18) is a quartic equation for ω, and has four roots. The two solutions with positive real parts of complex wave frequency represent two families of unstable solutions, while the other two solutions with negative real parts of complex wave frequency correspond to stable solutions which are not concerned in this thesis.

As for *absolute instability*, both ω and k are complex with ω_i standing for temporal wave growth rate and k_i for spatial growth rate. To find the absolute instability, pinch points k_0 on the complex k-plane with $\omega_i > 0$ are to be sought from the dispersion relation, Eq. (4.21), numerically. A mesh-searching technique has been developed for this purpose. The details for this technique is presented in Appendix D.

Another instability mode that a flow system may have is *convective instability*, meaning that disturbances in the system grow only with spatial locations. What need be solved from the dispersion relation Eq. (4.18) is complex k for given real wave frequency ω_r with $\omega_i = 0$. The solution to be considered is the one with $k_i < 0$, representing unstable convective wave growth. It is known that the convective instability occurs only for those flow conditions under which $\omega_i < 0$ for the pinch points. Therefore for any flow system, it is usual to find the absolute instability mode

first and then the convective instability.

Muller's method [59] is used for all modes of instability analysis mentioned above. This method requires three initial guesses. The computational iteration is terminated when the relative error between the successive solutions is less than a certain pre-set tolerance, usually 10^{-5} in this work.

The modified Bessel functions of the first and second kind with complex arguments are evaluated by the iterative scheme [60]. It should be noted that the evaluation of the Bessel functions with complex argument, especially the modified Bessel function of the second kind, involves many difficulties since there is no reliable and accurate commercial software package available [61]. Considerable efforts have been devoted to improving the computational accuracy of these Bessel functions.

Chapter 5

Results and Discussion

The numerical results based on linear instability analysis are presented in this chapter. The dimensionless dispersion relation, Eq. (4.18) or Eq. (4.21), is solved by using Muller's method [59]. To begin with, the temporal instability is first studied to illustrate in general effects of various parameters on annular liquid sheet instability and to understand the fundamental mechanism of the breakup process of annular liquid jets. Secondly, the absolute instability is investigated. The critical Weber numbers which separate absolute from convective instability are presented for various flow conditions. Finally, the convective instability analysis is performed to examine, especially, the effects of gas stream velocities.

5.1 Temporal Instability

In this section, the temporal wave growth rates ω_i are presented for annular viscous liquid jets. The effects of geometric parameters are first discussed by considering the stationary surrounding gas. The second part of this section focuses on the effects

of various flow parameters, such as gas and liquid velocities, liquid viscosity, liquid and gas density and surface tension, on temporal wave growth rates ω_i and dominant wave numbers $k_{r,m}$.

5.1.1 Effects of Geometric Parameters

The geometric parameters, which play an important role in the instability of annular liquid sheets or jets, are the inner radius r_a, outer radius r_b or half thickness $(r_b - r_a)/2$ of the annular sheet. When they are assigned different extreme values, as indicated in Appendix C, three limiting cases of plane liquid sheet, cylindrical gas jet and cylindrical liquid jet can be approached geometrically. However, of main concern in this instability analysis are if the dispersion relations for these three limiting cases can be retrieved from that for annular liquid jets, and if the numerical solutions from solving the dispersion relation of annular liquid jets can approach those for the three cases when various values are assigned to r_a and r_b and the extreme conditions are approached by r_a and r_b.

In the following section, the asymptotic behavior of the dispersion relation Eq. (4.18) for annular liquid jets, is examined for different extreme geometric conditions. The detailed procedures for retrieving the dispersion relations of the three limiting cases from that for the annular liquid jet are presented in Section 4.3. The numerical solutions of these dispersion relations are discussed, and the effects of the geometrical parameter on the jet instability are examined.

(a) Approximation of Large Sheet Radii — Plane Liquid Sheet

As shown in Section 4.3, the dispersion relations, Eq. (4.26) and Eq. (4.27), for plane liquid sheets are retrieved from that for annular liquid jets as r_a^* and r_b^* approach to infinity with keeping the sheet thickness $(r_b^* - r_a^*)$ constant. The equations,

Eqs. (4.19) and (4.20), for the amplitude ratio of the initial disturbances at the two interfaces of the annular liquid sheet becomes either $\epsilon_a/\epsilon_b = 1$ or $\epsilon_a/\epsilon_b = -1$ for the plane liquid sheet. The result of $\epsilon_a/\epsilon_b = 1$ corresponding to Eq. (4.26) indicates that the two interfaces of the liquid sheet are displaced in the same directions, which is often referred to as sinuous mode of disturbances. On the other hand, the initial amplitude ratio, $\epsilon_a/\epsilon_b = -1$ for the result given in Eq. (4.27), implies that the two interfaces are displaced in exactly opposite directions, corresponding to a varicose mode. Therefore, Eqs. (4.26) and (4.27) represent, respectively, the dispersion relations for the sinuous and varicose disturbances for viscous plane liquid sheets moving in a stationary inviscid gas medium, and they are identical to the results given previously by Li and Tankin [36]

For annular liquid sheets, Eqs. (4.19) and (4.20) indicate that the initial disturbance amplitude ratio is generally a complex rather than a real value as for the plane liquid sheet shown above. This implies that the two interfacial waves differ not only in the magnitude of the initial disturbance amplitudes but also in the phase angle. In general, the phase difference between the two surface waves will be neither zero nor π. Because a zero phase difference represents the sinuous mode (exactly in phase) and a phase difference of π corresponds to the varicose mode (exactly out of phase), apparently, the strictly sinuous and varicose mode only exist for plane liquid sheets. For the present annular liquid sheets, the two unstable interfacial waves are neither sinuous nor varicose. Rather, they will exhibit a phase difference θ between them as illustrated in Figure 4.1 However, as the inner and outer radius of the annular sheet approach infinity, the above analysis implies that one unstable mode will approach to sinuous mode, and the other to varicose mode. As the numerical computation indicates, in general the value of θ for the former case remains fairly close to zero, while for the latter close to π. Therefore, the two unstable modes will hereafter be

referred to as para-sinuous and para-varicose mode.

The numerical results from the dispersion relation, Eq. (4.18), for the annular liquid sheets are obtained by using successively large values for the inner and outer radius r_a and r_b ($\rightarrow \infty$) while maintaining the sheet thickness $2r_h$ constant. The results show how a plane liquid sheet is approached, and also reveal the effect of the sheet curvature on the instability process. Figures 5.1 and 5.2 present two sets of typical unstable solutions, with one set being at a relatively high Weber number and the other at a low Weber number. It is clear from Figures 5.1A and 5.1C that the disturbance growth rate decreases for both para-sinuous and para-varicose modes as the radii of the annular sheet increase. This indicates that the sheet curvature has a destabilizing effect on the sheet breakup process. Figures 5.1B and 5.1D show that in general the amplitude of the disturbances at the outer interface is larger than its counterpart at the inner interface for the para-varicose mode, while the result is just opposite for the para-sinuous mode. When r_a and r_b become large, both surface waves tend to have the same magnitude of amplitude, as this is the case clearly shown earlier by the analytical approach. Therefore, the curvature effect is seen to reduce the relative amplitude of the disturbances at either the inner or outer interface, depending on whether it is the para-varicose or para-sinuous mode. The phase difference θ between the two surface waves is very close to the value of π for the para-varicose mode, and zero for the para-sinuous mode. For example, for the results shown in Figures 5.1A and 5.1B, θ at the maximum growth rate is approximately equal to 0.03 degree while θ has a value of 180.57 degree for the results given in Figures 5.1C and 5.1D.

At low Weber numbers, the behaviors of the amplitude ratios and the phase differences between the two interfacial waves are very similar to those at high Weber numbers discussed above. However, as shown in Figure 5.2A, the growth rate for a

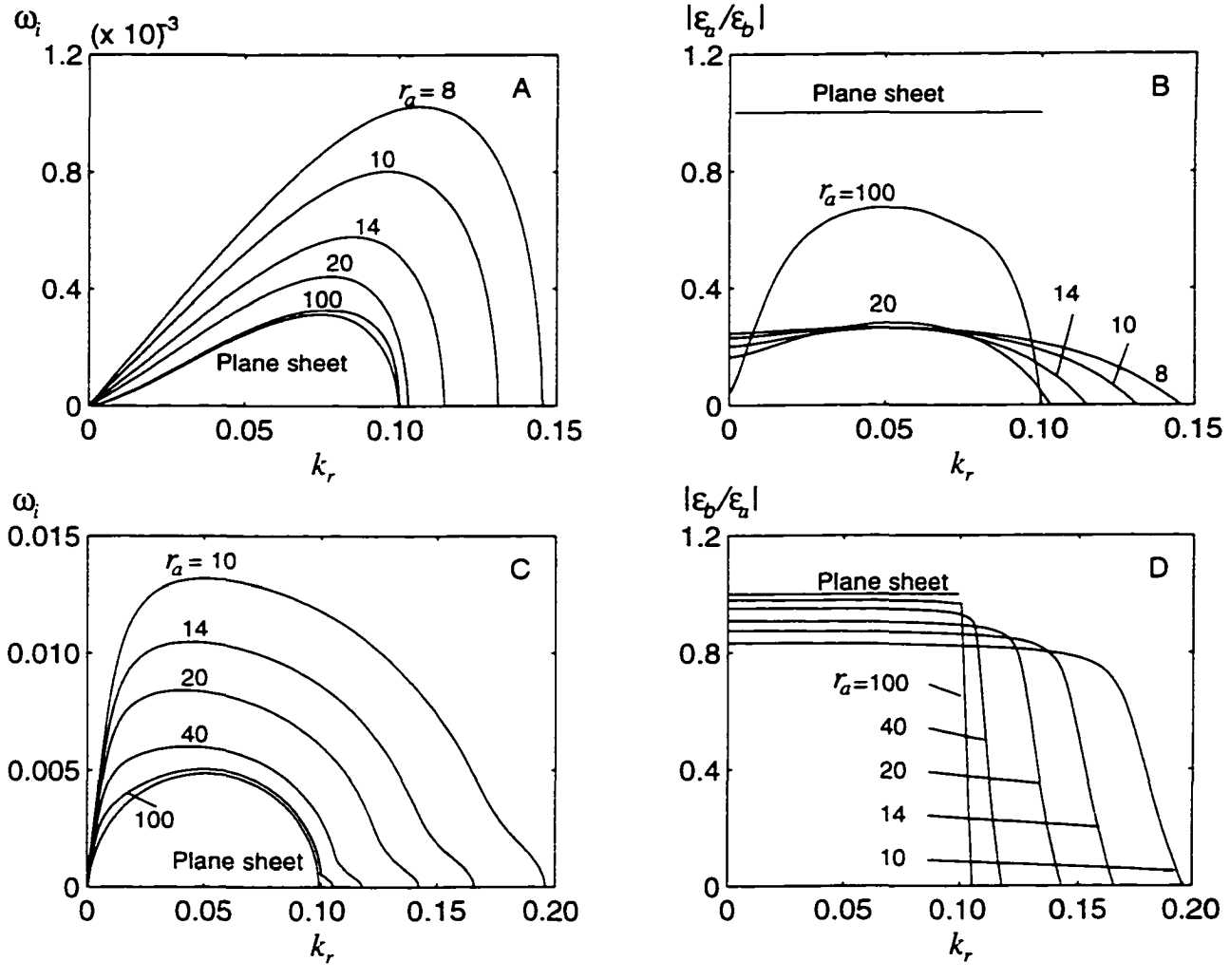

Figure 5.1: The curvature effects on the disturbance growth rate and amplitude ratio for A, B para-varicose and C, D para-sinuous modes. $We = 100, Re = 1000, \rho = 0.001, r_h = (r_b^* - r_a^*)/2$ (hence $r_b = r_a + 2$) and r_a as shown.

thin annular liquid sheet exhibits two peaks for the para-sinuous mode. The peak at the smaller wavenumber, which will be referred to as the first peak hereafter, is fairly independent of the viscous effects. Whereas the peak at the larger wavenumber, or the second peak, is fairly insensitive to the curvature effects.

It is seen in the figure that the first peak is influenced significantly by the sheet curvature. Even when the inner and outer radii, normalized by the half sheet thickness, reach the order of 10^4, the corresponding growth rates are still considerably larger than the values for plane liquid sheets ($r_a = r_b = \infty$). But for the results given in Figure 5.1, r_a and r_b on the order of 60 are sufficiently large for the present results to approach those of plane liquid sheets. This implies that the curvature of the annular sheet is an important parameter for the sheet instability process, and the critical sheet radius beyond which the curvature effect can be neglected depends strongly on the flow conditions. The significant enhancement of the instability process by the sheet curvature may explain why in practice annular or conical liquid sheets have much smaller breakup lengths than the corresponding plane liquid sheets.

Although liquid viscosity has little effect on the first peak as shown in the figure, the second peak increases considerably with the Reynolds number, indicating viscous effects promote instability. In fact, the second peak even becomes larger than the first peak at $Re = 0.1$ for $r_a = 10^4$ and ∞, implying that in reality it dominates the instability process under these conditions. These instability characteristics are very similar to plane liquid sheets at low Reynolds numbers examined by Li and Tankin [36]. Similarly, it can also be shown that the first peak here is due to the aerodynamic interactions between the liquid and gas phases, while the second peak is primarily promoted by viscous effects. The viscous promotion of the instability is achieved by the resonant effects due to interfacial pressure fluctuations, which result from a frequency shift and a phase shift between the gas and liquid phase pressures

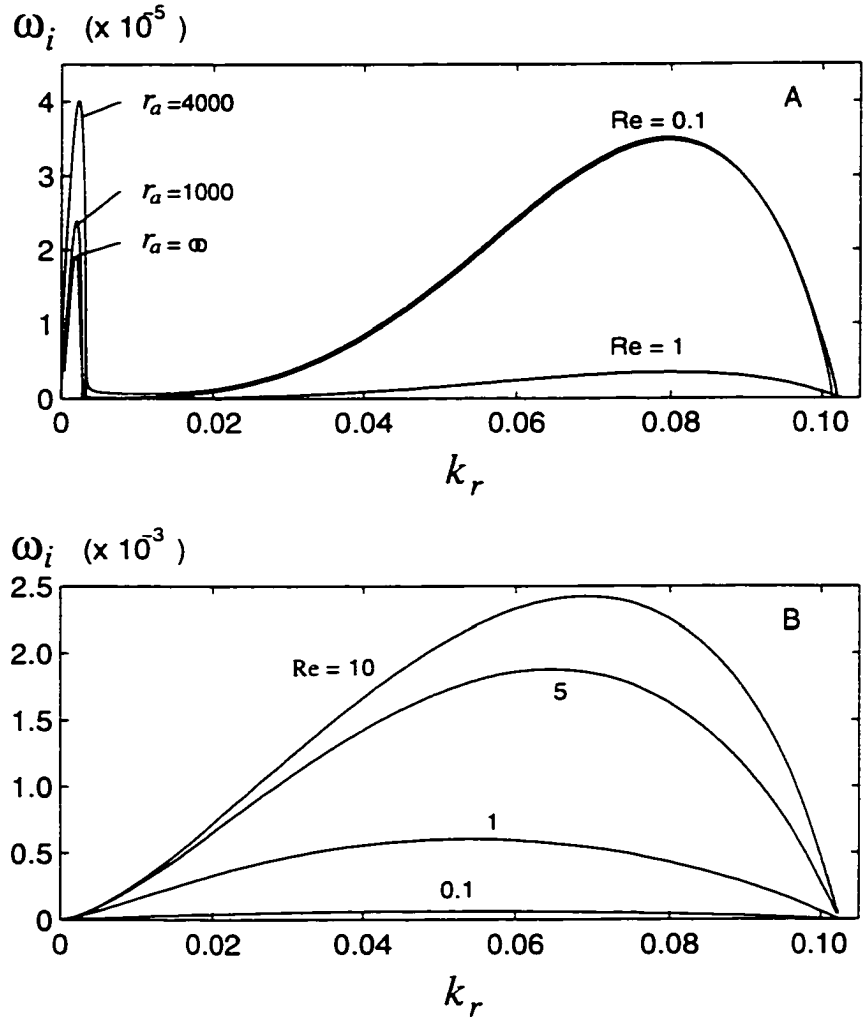

Figure 5.2: The effects of sheet curvature and Reynolds number on the disturbance growth rate and amplitude ratio for A. para-sinuous and B. para-varicose modes. $We = 1.025, Re = 1000, \rho = 0.1, r_h = (r_b^* - r_a^*)/2$ (hence $r_b = r_a + 2$) and r_a as shown.

induced by the liquid viscosity [36]. From these points of view, the first peak may be called aerodynamic instability while the second peak viscosity-enhanced instability. However, it should be pointed out that even for the second peak, an examination of disturbance energy [38] reveals that liquid viscosity still dissipates disturbance kinetic energy, while interfacial pressure fluctuations provide the energy source for the growth of disturbances. This clearly illustrates the dual role the viscosity plays in the instability process. Other examples of dual effects of viscosity have been discussed in [36].

As a comparison, the corresponding results for the para-varicose mode are given in Figure 5.2B. The growth rate curves for $r_a = 2 \times 10^3$, 4×10^3, 10^4 and ∞ coincide with one another, and hence is not discernible. Clearly at these large sheet radii, the results are identical to plane liquid sheets. Further, it is seen that the growth rate increases with the Reynolds number, indicating that the viscous effect reduces the instability of the para-varicose mode.

(b) Limits of Large Outer Radius — Gas Jet in a Liquid Medium

The equations, Eq. (4.29) and Eq. (4.30), obtained from the dispersion relation for annular liquid sheets by allowing the outer radius r_b of the annular sheet to approach to infinity while keeping the inner radius r_a constant in Section 4.3, are the ones for inviscid gas jets exposed to moving viscous liquid streams. It can be shown that corresponding to Eq. (4.29), the amplitude ratio ϵ_a/ϵ_b goes to zero from the negative side, indicating this solution is approached from the present para-varicose mode as $r_b \to \infty$. For sufficiently large r_b, it is seen that this mode is associated with the outer interface, which becomes a plane surface separating two homogeneous fluids as $r_b \to \infty$. Therefore, the instability associated with the outer interface is due to the velocity discontinuity across the interface, and Eq. (4.29) represents the classical Kelvin-Helmholtz instability with the effect of surface tension included [38, 58], and

is identical to the results for a stationary gas medium over a flowing liquid stream [38] if U_a in the equation is set 0.

Equation (4.30) is the limiting form for the para-sinuous mode, and represents the dispersion relation for a quiescent gas column in a moving liquid medium. Clearly it is related to the disturbances at the inner interface. For $\rho = 0$ and $Re \rightarrow \infty$, Eq. (4.30) becomes

$$(kU_\ell - \omega)^2 = -\frac{k(1-k^2)}{We}\frac{K_1(k)}{K_0(k)} \tag{5.1}$$

which is identical to the result first given by Rayleigh [8] for this case. It is seen that the unstable wavenumber range is dictated by $k < 1$ or the dimensional wavenumber becomes $\alpha < 1/r_a^*$, and the growth rate becomes $\Omega \sim 1/r_a^*$. Therefore, both the dimensional unstable wavenumber range and growth rate can be very large as the inner radius is reduced. The source of this instability is due to the surface tension effects [8].

The above two unstable solutions for $r_b \rightarrow \infty$ can also be retrieved numerically as shown in Figure 5.3. For the para-varicose mode given in Figures 5.3A and 5.3B, it is seen that the growth rate gradually increases to the value for the classical Kelvin-Helmholtz instability at $r_b \approx 100$, and the disturbance amplitude at the inner interface vanishes for $r_b \rightarrow \infty$. Therefore, the two interfacial waves become independent of each other. For the para-sinuous mode (Figures 5.3C and 5.3D), the growth rate reduces as r_b increases, and approaches to the results for a gas column in a moving liquid medium at $r_b \approx 10$, and the disturbance amplitude at the outer interface gradually goes to zero, another way of showing decoupling of the two interfacial waves. Hence, disturbances at one interface have little influence to the instability development on another interface when r_b is sufficiently large.

(c) Limits of Small Inner Radius— Round Liquid Jet

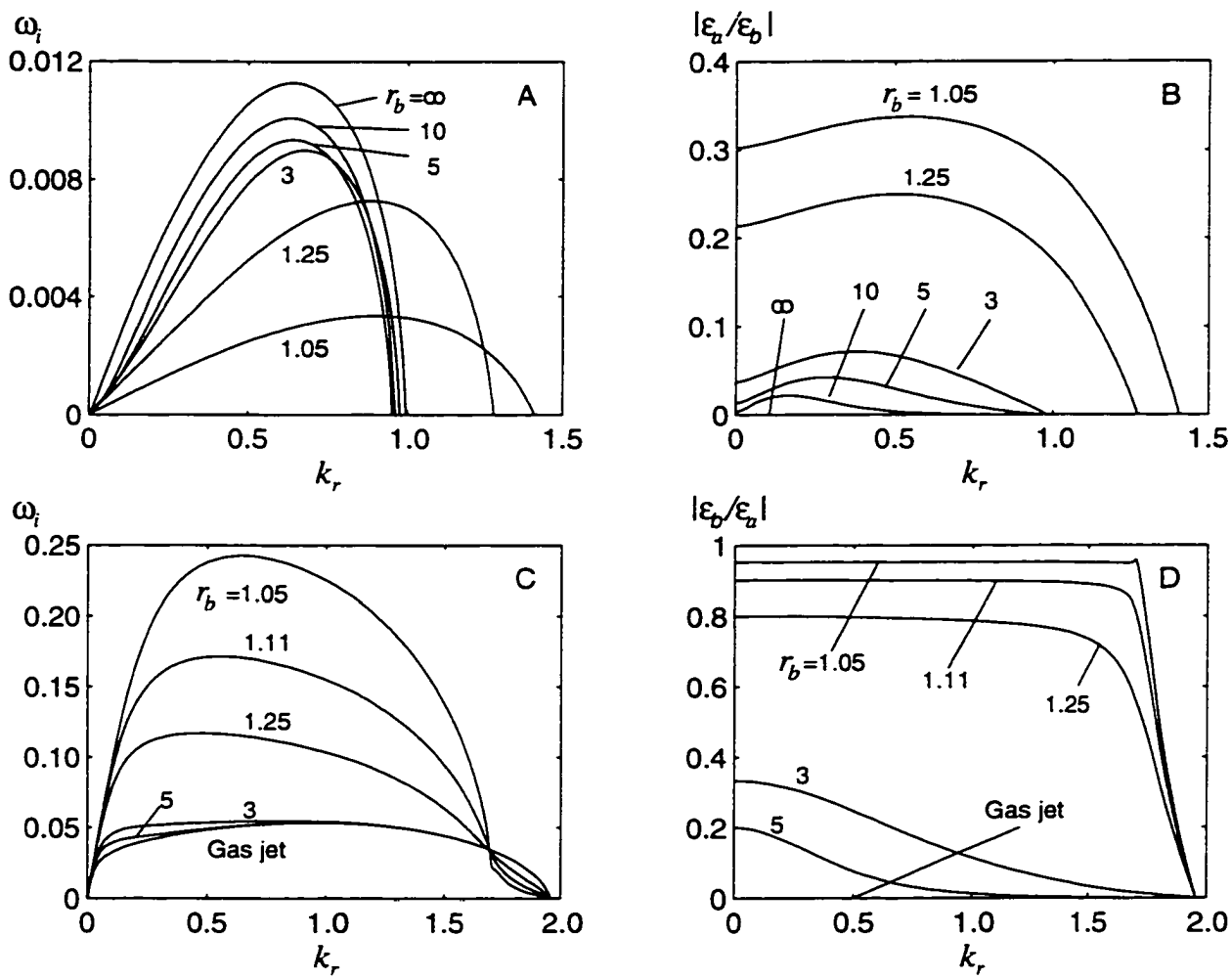

Figure 5.3: The effects of outer radius r_b on the disturbance growth rate and amplitude ratio for A, B para-varicose and C, D para-sinuous modes. $We = 1000$, $Re = 1000$, $\rho = 0.001$, $r_h = r_a^*$ (hence $r_a = 1$) and r_b as shown.

The equation, Eq. (4.34), obtained from the dispersion relation for annular liquid sheets by allowing the inner radius r_a of the annular sheet approaches to zero when keeping the outer radius r_b constant in Section 4.3, represents the dispersion relation for a cylindrical viscous liquid jet exposed to an inviscid gas stream, which is identical to the dispersion relation for a viscous round liquid jet in an inviscid quiescent gas medium [11, 54] if $U_b = 0$ in the equation. The amplitude ratio approaches zero from the negative side, indicating that the above equation is approached from the para-varicose mode of the annular liquid sheet. Hence it becomes clear that the para-varicose mode is associated with the outer interface at sufficiently small inner radius r_a.

On the other hand, if s and k (i.e., the unstable wavenumber range) are not finite as $r_a \rightarrow 0$, the asymptotic relation for the Bessel functions cannot be applied. In fact, the second unstable solution, which is the para-sinuous mode in this case, is associated with the inner interface as $r_a \rightarrow 0$. Because the surface tension term, σ/r_a^*, becomes dominant for sufficiently small inner radius and the surface tension force promotes capillary instability, both the unstable range and the growth rate for the para-sinuous mode will be very large and in fact, approach to infinity as r_a vanishes. Physically, as $r_a \rightarrow 0$, the influence of the outer interface will diminish and two surface waves will be eventually decoupled. Then the instability associated with the inner interface will represent an inviscid gas column in a moving liquid medium, a case analyzed in the previous section. Mathematically, it can be shown that the dispersion relation for this mode is reduced to Eq. (4.30) by choosing the inner radius r_a^* as the reference length scale, and maintaining the resulting dimensionless growth rate and wavenumber finite as $r_a \rightarrow 0$.

These behaviors of the two unstable solutions can be also seen from the numerical results shown in Figure 5.4. Figures 5.4A and 5.4B present the results from the

dispersion relation, Eq. (4.18), for the para-varicose mode. It is clearly seen that the growth rate approaches nicely to the results for round liquid jets, and the corresponding disturbance amplitude at the inner interface decreases gradually to the value of zero, as expected, when $r_a \rightarrow 0$. However, for the para-sinuous mode as given in Figures 5.4C and 5.4D, the growth rate decreases first, then it keeps on increasing along with the unstable wavenumber range as the inner radius r_a is reduced. Further, the growth rates for the para-sinuous mode is generally much larger than the corresponding values for the para-varicose mode. Hence the para-sinuous mode will dominate and be observed in reality. Then it seems that the present annular sheet results could not be continuously reduced, in practice, to round liquid jet results since the latter is the limit of the present para-varicose mode as discussed earlier.

The explanation may lie in the fact that the disturbance amplitude at the inner interface, as shown in Figure 5.4D, becomes very large ($\rightarrow \infty$) for the para-sinuous mode as $r_a \rightarrow 0$. Hence at sufficiently small inner radius, the inner wave amplitude may become so large that the inner interface at the wave troughs may reach the centerline of the annular sheet, thus forming the enclosed gas bubbles periodically along the annular jet. As the inner radius r_a vanishes, the size of the gas bubbles reduces to zero, hence retrieving the round liquid jet. This scenario of recovering the round liquid jet from the annular liquid sheet has been alluded to by the previous experimental observations [20], but is discussed explicitly here for the first time from a theoretical point of view. The formation and separation of the gas bubbles from the annular liquid sheet have been the subject of extensive previous investigation [18, 19, 20, 21, 22, 23, 24, 28, 31, 30].

The results presented above make it possible to identify and classify the eigenvalues of the flow system, and to gain some insight into the physical nature of the jet instability. For annular liquid sheets, unstable interfacial waves at the two liquid-gas

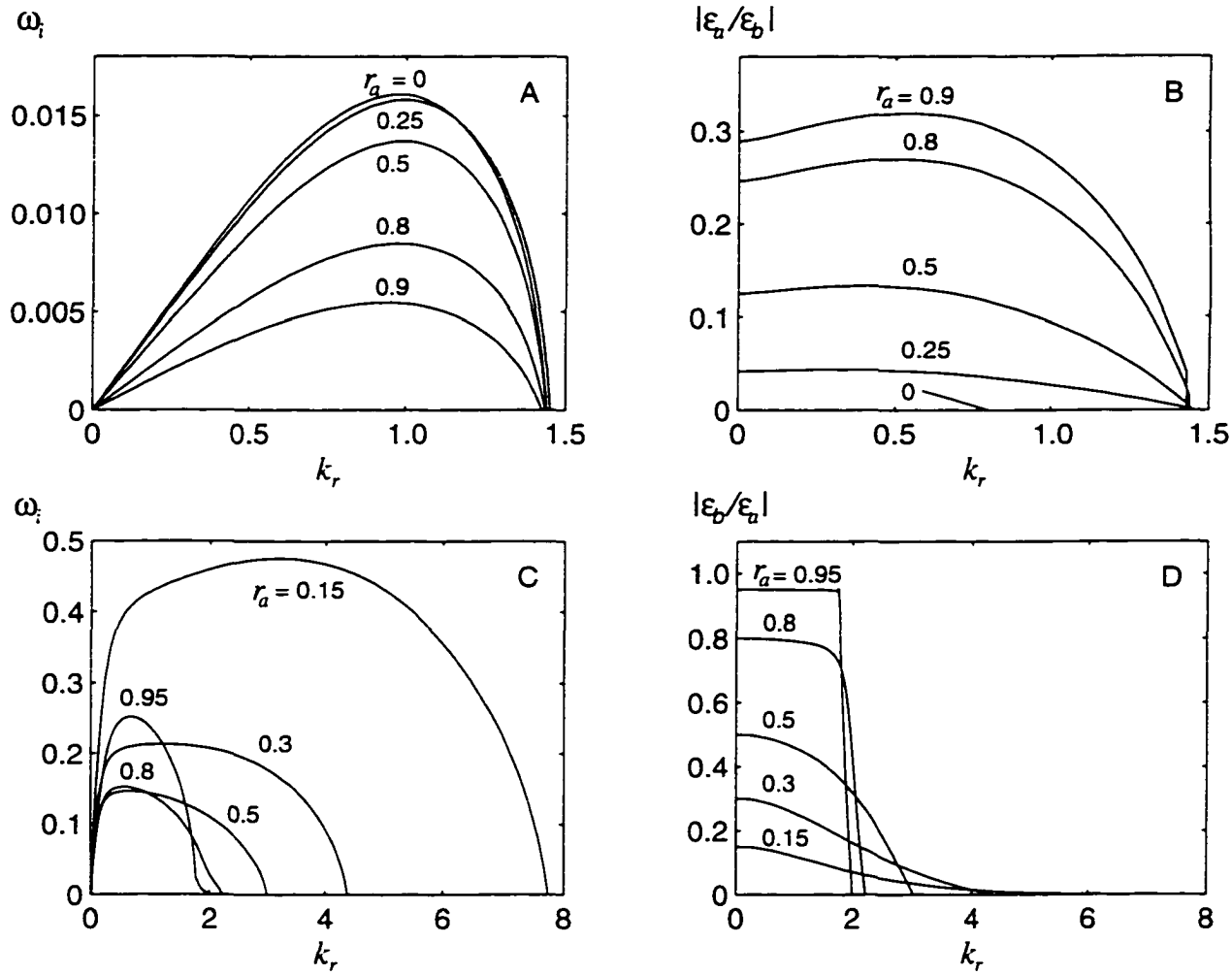

Figure 5.4: The effects of inner radius on the disturbance growth rate and amplitude ratio for A, B para-varicose and C, D para-sinuous modes. $We = 1000$, $Re = 1000$, $\rho = 0.001$, $r_h = r_b^*$ (hence $r_b = 1$) and r_a as shown.

interfaces are neither sinuous (exactly in phase) nor varicose (exactly out of phase) as for plane liquid sheets. In Fact, there exists a phase difference θ of certain numerical value between two interfacial waves. According to the θ values from the dispersion relation, the corresponding two sets of solutions obtained are term as para-sinuous and para-varicose ones depending on whether the θ value is close to 0 or π. The results shown above also serve as a partial check on the dispersion relations derived in this study, and help guiding initial guesses in the numerical solutions of the dispersion relations.

5.1.2 Effects of Flow Parameters

The flow parameters affecting the instability of annular liquid jets are mainly the liquid and gas velocities and densities, liquid viscosity, and surface tension. To illustrate the effects of these flow parameters, the numerical solutions of the dispersion relation, Eq. (4.18), are presented in two parts. In the first part, the dependence of the temporal wave growth rate ω_i on various flow parameters are presented. In the second part, the dominant wave number $k_{r,m}$ is examined under various flow conditions.

(a) Effects of Flow Parameters on Temporal Wave Growth Rates

To show **the effects of liquid and gas velocities** on the instability of annular liquid jets, the dispersion relation, Eq. (4.18), is solved for temporal modes of unstable wave growth rate ω_i at a fixed nozzle geometry of $r_a = 40.12$ and $r_b = 42.12$ for various inner U_a and/or outer gas-to-liquid velocity ratio U_b. The flow conditions and nozzle sizes used here correspond mostly to those used in the experiments to be presented later. The numerical results are presented in Figures 5.5 to 5.8.

Figure 5.5 shows the unstable wave growth rate ω_i for different velocities of the inner gas stream U_a with stationary outer gas medium ($U_b = 0$). It is seen from

Figure 5.5A that the growth rate for para-sinuous disturbances decreases along with the dominant wave number as the inner gas velocity increases from 0 to 1, or the velocity difference ($\Delta U_a = |U_a - 1|$) between the gas and liquid phases at the inner interface decreases from 1 to 0. Further increase in the inner gas velocity U_a up to 2 causes the growth rate ω_r to increase since the velocity difference ΔU_a increases from 0 to 1. The unstable wavenumber range does not change significantly for $0 \leq U_a \leq 2$. When U_a is larger than 2, ω_r increases considerably while the dominant wave number increases relatively slowly. Clearly the velocity difference across the interface enhances the jet instability and extends the unstable wave regime to higher wave numbers. However, it is seen that the growth rate at a higher gas velocity (e.g., $U_a = 1.7$) is larger than that at a lower one (e.g., $U_a = 0.3$), even though the velocity difference across each interface is the same. Hence, it indicates that not only the velocity difference across each interface but also the absolute gas and liquid velocity themselves affect the breakup processes of annular liquid jets. Calculations of disturbance energy, similar to that of Li [38] and Lin and Creighton [54], implies that a shift in the disturbance frequency and phase angle of gas pressure fluctuations [36] is responsible for this behavior.

As for the para-varicose mode (Figure 5.5B), the growth rate ω_i also increases with the velocity difference ΔU_a, but approaches a certain limit. This indicates that when the gas velocity is sufficiently large, further increase in the gas velocity has little effect on the growth rate of the para-varicose mode. This is because the para-varicose mode, as shown by Li [38] for plane liquid sheets, is always related primarily with the smaller of the two velocity differences across the two interfaces, whereas the para-sinuous mode is always associated with the larger velocity difference across the interfaces. It is also seen from Figure 5.5 that the unstable wave growth rate for the para-sinuous mode is approximately two orders of magnitude larger than that for

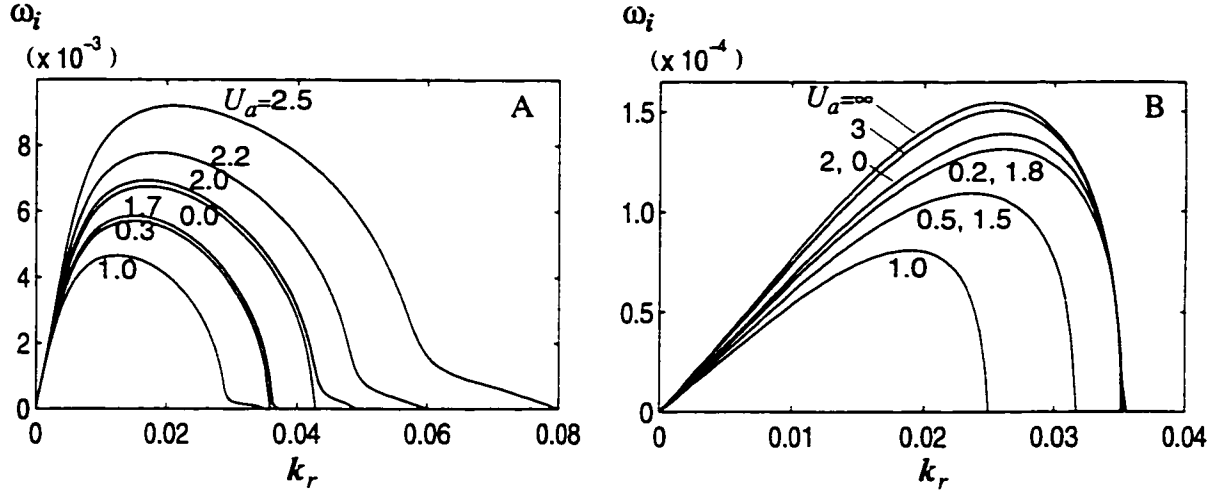

Figure 5.5: Wave growth rate for different velocities of inner gas stream with stationary outer gas medium. $r_a = 40.12$, $Re = 4112$, $We = 19.25$, $\rho = 0.00129$ and $U_b = 0$. A: para-sinuous and B: para-varicose mode.

the corresponding para-varicose mode, indicating that in practice, the para-sinuous unstable waves will outgrow para-varicose ones and predominate the jet breakup processes. However, it is known that the para-varicose mode becomes more important as the gas-to-liquid density ratio ρ increases. As Rangel and Sirignano [62] show for a plane liquid sheet, the growth rates for both modes become comparable at $\rho = 0.25$, and the para-varicose mode becomes dominant at $\rho = 1$. For the present problem, the para-sinuous mode has much larger growth rate than the corresponding para-varicose mode for the density ratio up to about 0.1, which corresponds to the conditions in rocket engines and is probably the highest density ratio that may be encountered in practical applications. Therefore, only para- sinuous solutions will hereafter be presented.

When the inner gas stream is stationary ($U_a = 0$), but the outer gas velocity U_b is varied, the wave growth rate ω_i exhibits the same trends as discussed above. The comparison of these two sets of para-sinuous growth rates are shown in Figure 5.6 at

low and high gas velocities, respectively. At low gas velocities ($U_a \leq 2$ or $U_b \leq 2$), it is seen from Figure 5.6A that the growth rate ω_i, shown by the dashed curves for $U_a = 0$, is larger than that given by the solid curves for $U_b = 0$ for a comparable gas velocity on the other side of the liquid jet. For either $U_a \geq 2$ or $U_b \geq 2$ and the gas on the other side of the liquid jet stationary, Figure 5.6B shows that ω_i for $U_b = 0$ is larger than that for $U_a = 0$. From both Figures 5.6A and B, it is seen that the larger wave growth rate always occurs when the velocity difference across the inner surface ($\Delta U_a = |U_a - 1|$) is larger than that across the outer interface ($\Delta U_b = |U_b - 1|$). This implies that to promote jet instability, a gas stream applied to the outer interface is more effective than to the inner surface when the gas velocity is less than twice the liquid velocity, while the gas stream with a velocity higher than twice the liquid velocity should be exposed to the inner interface. This may explain why the air stream in practical air-assisted atomization is sometimes supplied inside of the liquid jet, and sometimes outside of the jet. It is also interesting to see from Figure 5.6B that the tailing portion of the growth rate curve at higher wave numbers increases with the gas velocity, and exceeds the leading portion at lower wave numbers when the gas velocity is approximately higher than 6. This indicates that the dominant wave length may not decrease smoothly with the gas velocity, rather may have a sudden decrease under certain flow conditions, e.g., at the inner gas velocity U_a of about 6 for the present case. Therefore, the corresponding drop size may suddenly decrease significantly as the gas velocity is gradually increased.

To examine the effect of co-flowing gas stream on the jet breakup process, the para-sinuous wave growth rate is shown in Figure 5.7, for various gas velocities on both sides of the liquid jet. For comparison, the growth rate due to a single gas stream on the inner side of the sheet is also shown in Figure 5.7. It is obvious from Figure 5.7A that the co-flowing gas stream increases the wave growth rate significantly

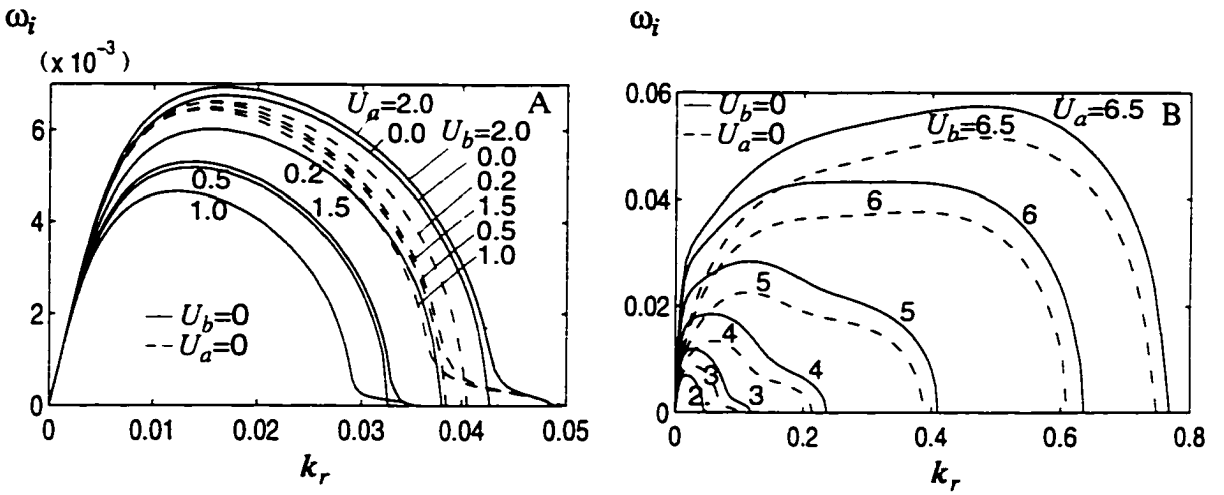

Figure 5.6: Wave growth rate of the para-sinuous mode for different velocities of gas stream on either inner or outer side of the jet. $r_a = 40.12, Re = 4112, We = 19.25$ and $\rho = 0.00129$. A: low and B: high gas velocity.

as compared with a single gas stream. It especially shifts the dominant wave to shorter wave lengths. This indicates that using co-flowing air in air-assisted atomization is beneficial for the improvement of the atomization performance compared with a single air stream when the air velocity is at least three or four times larger than the liquid velocity (Figure 5.7A). When the dimensionless gas velocity is lower than 2, as shown in Figure 5.7B, the co-flowing gas stream has little effect on the wave growth rate. Hence, it is less attractive for practical applications at low gas velocities.

Shown in Figure 5.8 is the wave growth rate with the same velocity jump across each interface but distinct velocity difference ($U_d = U_a - U_b$) between two gas streams for each pair of curves. It is seen that the growth rates for each pair of curves are almost the same, indicating that it is the velocity discontinuity across each interface that mainly determines the growth rate. The small difference shown is due to the different outer gas velocities ($U_b = 0$ for solid curves and $U_b = 2$ for dashed curves), implying also that the breakup of the annular liquid jet depends on not only the

velocity difference across each interface but also the absolute velocity of each liquid and gas stream. However, it should be pointed out that the effect of absolute velocity is relatively small and at best secondary compared to that of velocity differences across the interfaces.

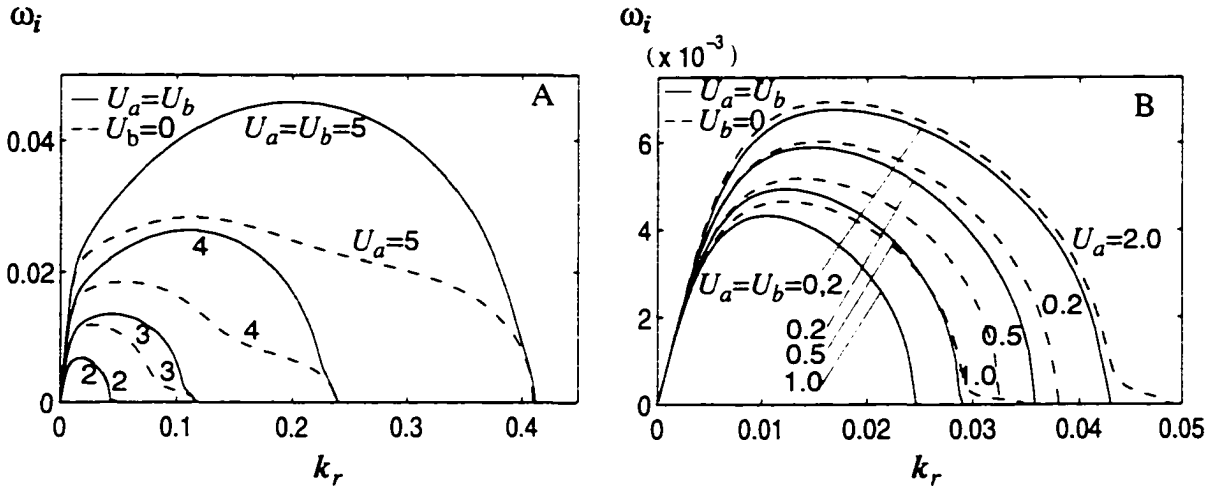

Figure 5.7: Wave growth rate of the para-sinuous mode for different velocities of gas streams on one side and both sides of the jet. $r_a = 40.12$, $Re = 4112$, $We = 19.25$ and $\rho = 0.00129$. A: high and B: low gas velocity.

The para-sinuous wave growth rates shown in Figures 5.9, 5.10, and 5.11 illustrate the effects of gas-to-liquid density ratio, liquid viscosity and surface tension on the breakup process of an annular viscous liquid jet with fixed jet radii ($r_a = 40.12$ and $r_b = 42.12$).

Figure 5.9 shows the growth rate at $Re = 1000$, $We = 1000$, and different **density ratios** ρ of gas-to-liquid with (5.9A) and without velocity discontinuity across the gas-liquid interfaces (5.9B). It is clear that the growth rate, the limiting and dominant wavenumber all increase with the density ratio as shown in Figure 5.9A. This indicates that the presence of the surrounding gas promotes the sheet disintegration process when there is a velocity difference at any interface. A large density ratio (i.e., low

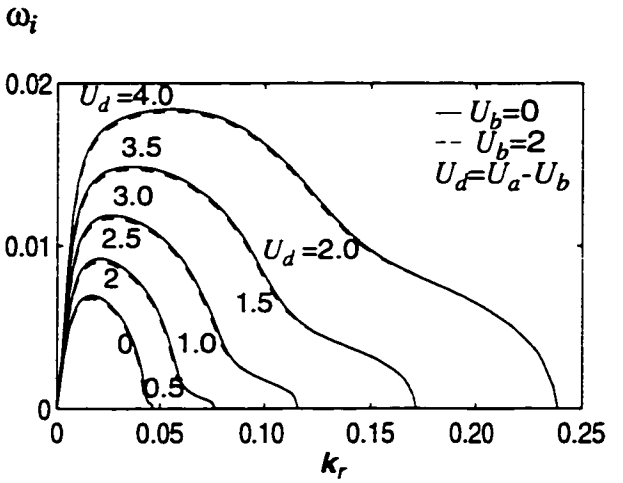

Figure 5.8: Effects of velocity difference between inner and outer gas streams on the para-sinuous wave growth rate for $r_a = 40.12$, $Re = 4112$, $We = 19.25$ and $\rho = 0.00129$.

liquid or high gas density) is always beneficial to the breakup of annular sheets. These results are consistent with the earlier studies on a cylindrical liquid jet [63] and plane liquid sheets [36, 38]. Without velocity discontinuity at the gas-liquid interfaces (Figure 5.9B) increasing liquid density or decreasing gas density promotes the jet breakup process, an effect opposite to the result with the velocity discontinuity as shown in Figure 5.9A. This implies that the presence of a gas medium would suppress the jet instability for the special case of $U_a = U_b = 1$.

To examine the **viscous effects of liquid**, the para-sinuous wave growth rate at various Reynolds number is presented in Figure 5.10 for $We = 500$ and $\rho = 0.001$. The inviscid solution is obtained from Eq. (4.22). It is seen from Figure 5.10 that the growth rates increase with the Reynolds number, similar to that with a velocity difference across the gas-liquid interface [47]. This implies that liquid viscosity has a stabilizing effect at high Weber numbers. However, for a thin annular sheet at low Weber numbers as shown in Figure 5.2, liquid viscosity may induce additional mode of instability, and may even become dominant under certain conditions. For most

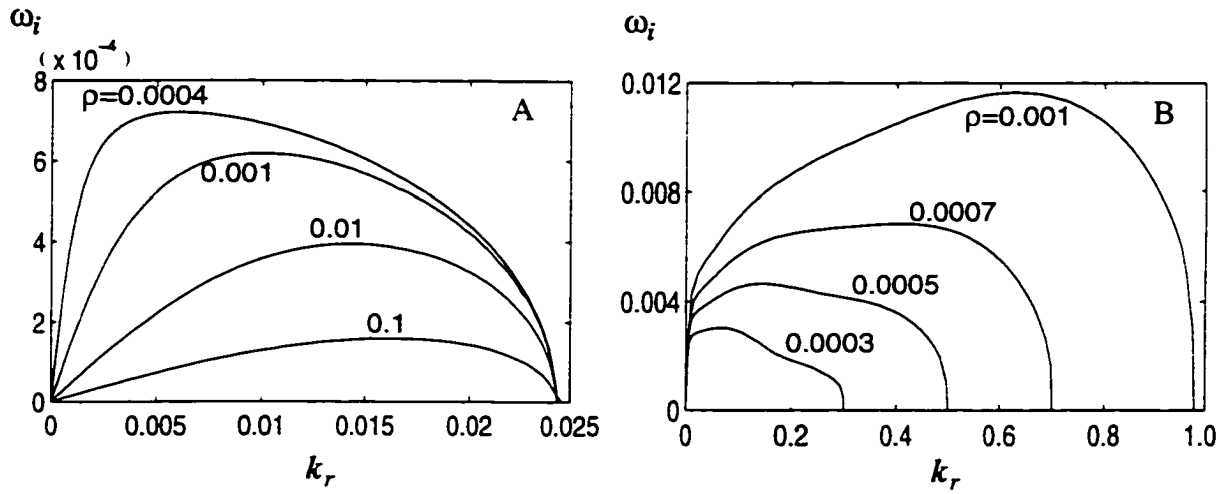

Figure 5.9: Density effects on the para-sinuous wave growth rate for $a = 40.12$, $Re = 1000$ and $We = 1000$. A: with velocity discontinuity, $U_a = 0$ and $U_b = 1$ and B: without velocity discontinuity, $U_a = U_b = 1$.

of practical applications where the Weber number is usually large, liquid viscosity reduces the degree of sheet instability.

Surface tension effect is examined by observing the para-sinuous growth rates shown in Figure 5.11 at different Weber numbers. It is found that the surface tension has a destabilizing effect when there is no velocity difference between the liquid and gas phases (Figure 5.11A). This means that without aerodynamic interaction, the capillary force is the only source of the jet instability, consistent with the observation for a cylindrical liquid column by Rayleigh [6]. However, it is observed that with a velocity difference across any interface, surface tension is the source of instability only at low Weber numbers (Figure 5.11B). At high Weber numbers, the source of the jet instability is the aerodynamic interaction between the liquid and gas phases. This is because, as for Rayleigh instability [6], surface tension has a destabilizing effect only for long wavelength disturbances. As Weber number increases, the unstable disturbances move into short wavelength range where the surface tension has a

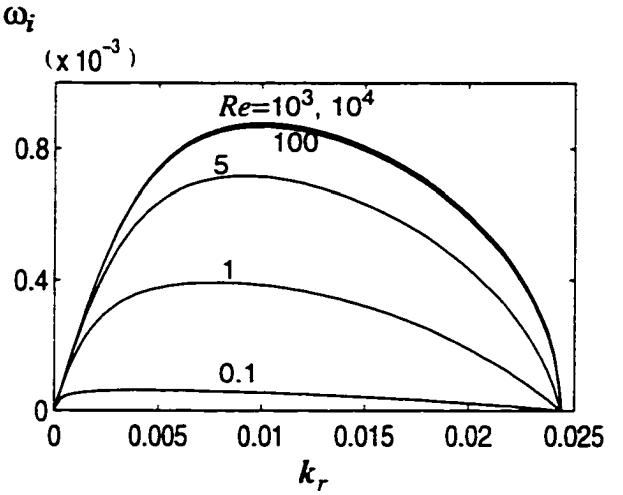

Figure 5.10: Effects of liquid viscosity on the para-sinuous wave growth rate without velocity discontinuity. $r_a = 40.12$, $We = 500$, $\rho = 0.001$ and $U_a = U_b = 1$.

stabilizing effect. This indicates that in atomization processes which usually occur at high Weber numbers, the onset of atomization is primarily due to the aerodynamic interaction that leads to the pressure fluctuation, which in turn causes the resonant oscillation of capillary waves at the liquid-gas interfaces [11].

(b) Effects of Flow Parameters on Dominant Wavenumber

The dominant wave number $k_{r,m}$, for which the growth rate is a maximum, is important for practical applications, because it gives an indication of the ligament breakup length, and in the absence of secondary atomization, a direct link to the drop size of the resulting sprays. Therefore, the effects on $k_{r,m}$ of various gas-to-liquid velocity ratios and density ratios, Weber numbers and Reynolds numbers have been investigated. The dependence of $k_{r,m}$ on various flow parameters can also be seen partly from Figures 5.5 to 5.11. For example, the dominant wave number in Figure 5.6 decreases slowly for $U_a < 1$ (or $U_b < 1$), and then increases quickly for $U_a > 1$ (or $U_b > 1$) with U_a (or U_b). Apparently, the surrounding gas streams with high velocities can improve the atomization performance in the sense of reducing

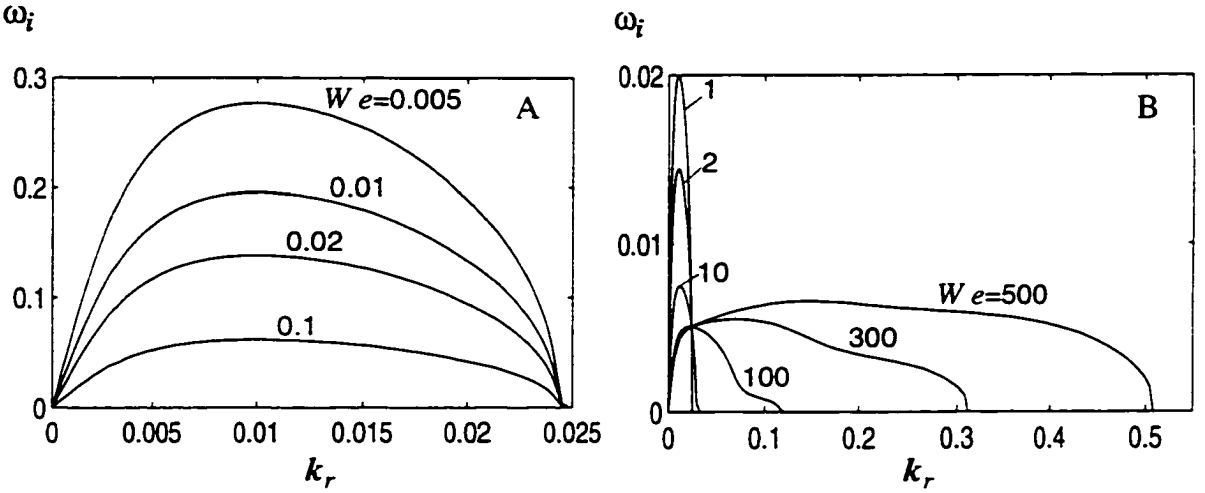

Figure 5.11: Surface tension effects on the para-sinuous wave growth rate for $r_a = 40.12$, $Re = 1000$ and $\rho = 0.001$. A: without velocity discontinuity, $U_a = U_b = 1$ and B: with velocity discontinuity, $U_a = 0$ and $U_b = 1$.

the droplet sizes. There is no significant changes with the dominant wave number between the case of the gas stream inside of the liquid jet and that of the gas outside of the jet under the conditions considered, unlike wave growth rate. The co-flowing gas streams increase the dominant wave number significantly when the gas-to-liquid velocity ratio is higher than 2 (see Figure 5.7).

Further results concerning the dominant wave number are presented in Figure 5.12. The dominant wave number $k_{r,m}$ is plotted with the inner gas stream velocity U_a for three different density ratios ρ in Figure 5.12A. It is seen that at a constant density ratio $k_{r,m}$ decreases slightly first for $U_a < 1$, and then increases with U_a for $U_a > 1$. Clearly, a minimum dominant wave number occurs at about $U_a = 1$, showing that the droplet size may have a maximum if the gas velocity is the same as the jet velocity. When $U_a > 1$, the dominant wave number increases smoothly with the gas velocity until a sudden increase in $k_{r,m}$ at a fixed U_a, e.g., $U_a \approx 6$ for $\rho = 0.00129$, is reached. Beyond this point, the dominant wave number increases sharply with U_a. The double

value of $k_{r,m}$ at certain U_a and ρ suggests that broader distribution of droplet sizes in a spray may occur at a practical condition. It can also be seen from Figure 5.12A that the dominant wave number $k_{r,m}$ always increases as the gas-to-liquid density ratio ρ increases, and the occurrence of the double-value $k_{r,m}$ depends not only on the gas velocity but also the density ratio, as shown earlier in Figures 5.6B and 5.9B. Therefore, it is the inertia of the gas stream that mainly affects the uniformity of droplet sizes in sprays.

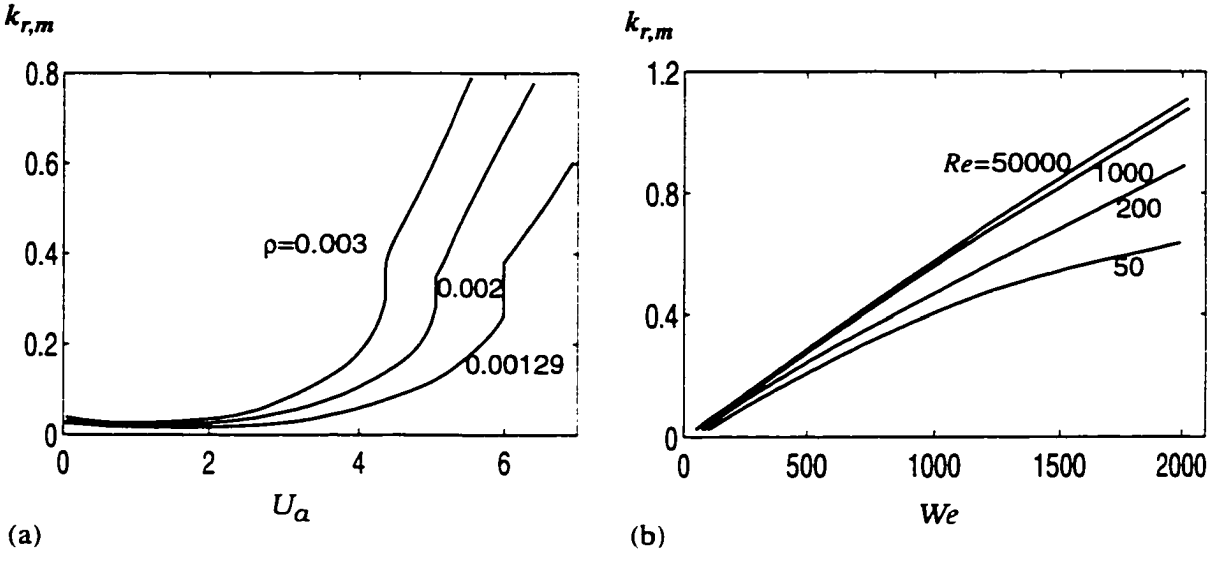

Figure 5.12: Dominant wave number for the para-sinuous mode with $r_a = 40.12$ and $U_b = 0$. (a) $Re = 4112$, $We = 19.25$ and (b) $\rho = 0.001$, $U_a = 2$.

Different from the effect of the gas inertia on the dominant wave number $k_{r,m}$, Weber number We and Reynolds number Re exhibit monotonic variation influence on the dominant wave number. As shown in Figure 5.12B, $k_{r,m}$ increases with We for a constant Re, and increases also with Re at a fixed We. This indicates that both surface tension and liquid viscosity may reduce the dominant wave number. That is the wavelength linked to the droplet size in liquid jet atomization may be increased, showing that to improve liquid atomization performance, less viscous liquid and small

surface tension fluid should be utilized in practice.

5.2 Absolute Instability

Absolute instability is presented in this section for an annular viscous liquid jet with its inner and outer sides exposed to inviscid gas streams of unequal velocities. The dispersion relation is solved by using Muller's method. An efficient mesh-searching method is used to find absolute instabilities for both para-varicose and para-sinuous modes of instability (See Appendix D for details about the method). The critical Weber numbers, which separate the region of convective from absolute instability, are presented under various flow conditions. The effects of various flow parameters are examined, especially the effects of the inner gas velocity on the jet instability. A liquid jet is of absolute instability if disturbances grow in the flow system not only through spatial locations but also with time. In another words, the imaginary part k_i of complex wave number k must be negative and the imaginary part ω_i of corresponding complex wave frequency ω positive. As the temporal growth rate ω_i varies from a positive to negative value with the Weber number increased and all the other flow parameters fixed, the instability mode of the jet will change from absolute to convective. The Weber number at which $\omega_i = 0$ is then a boundary separating absolute from convective instability, and therefore defined as critical Weber number We_c. It is found that under certain flow conditions, finite critical Weber numbers exist for both para-sinuous and -varicose modes for annular liquid jets. Unlike plane liquid sheets, there is no absolute instability ($We_c = 0$) at all for para- varicose mode [37].

The critical Weber numbers shown in Figure 5.13 are obtained under various flow conditions for para-varicose mode. Figure 5.13A illustrates the dependence of the

critical Weber number We_c on the dimensionless inner radius r_a of the annular jet. To demonstrate how We_c for a cylindrical liquid jet is approached as the inner radius r_a^* vanishes by keeping the outer radius r_b^* constant, r_b^* is selected as the reference length scale and the liquid velocity U_ℓ^* is used as the reference velocity scale. When the Weber number of the system is larger than the critical Weber number We_c, the jet is of convective instability while when it is smaller than We_c the jet is absolutely unstable. The critical Weber number We_c shows complex variation as r_a decreases with the Reynolds numbers Re fixed. However as r_a approaches zero, the critical Weber number for a cylindrical liquid jet is obtained [53]. The increase in We_c with Re implies that the liquid viscosity reduces the region of absolute instability and hence enlarges the region of convective instability.

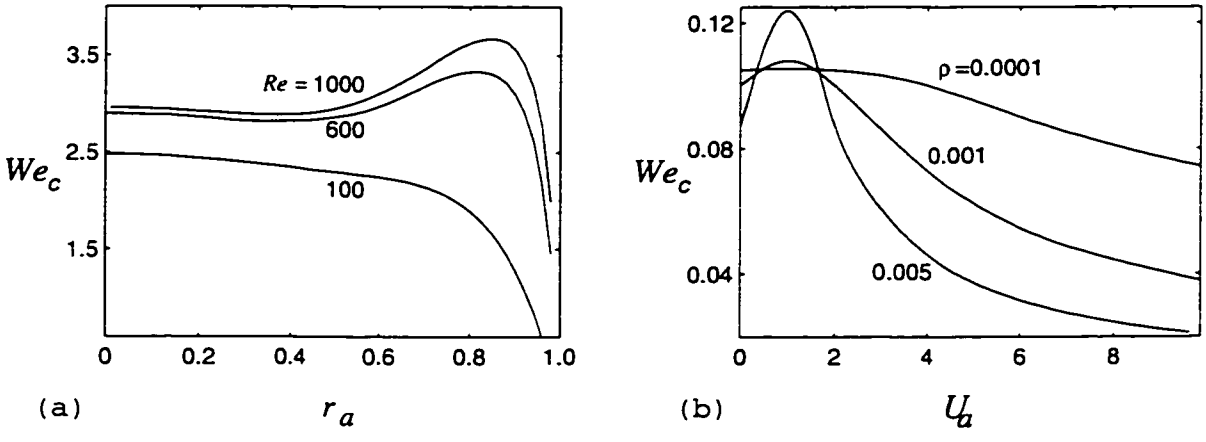

Figure 5.13: Critical Weber number with various flow parameters for para-varicose mode. $U_\ell = 1$ and $U_b = 0$. (a) $r_b = 1$, $U_a = 0$ and $\rho = 0.001$; (b) $r_a = 40$ ($r_b = r_a + 2$) and $Re = 100$.

Figure 5.13B presents the dependence of the critical Weber number We_c on the inner gas velocity U_a for three fixed density ratios ρ. The reference length and velocity scale in this case are chosen as the half jet thickness $(r_b^* - r_a^*)/2$ and the liquid velocity U_ℓ^* respectively. As shown in Figure 5.13B, We_c increases with the inner gas velocity U_a, reaches a maximum and then decreases monotonically for sufficiently large U_a.

The critical Weber numbers We_c are finite even at $U_a = 0$, different from that for para-sinuous mode to be discussed below. It is also seen that the curves of We_c is almost symmetric about $U_a = 1$. This implies that the relative velocity between liquid and gas determines the absolute instability for para-varicose mode at different density ratios, although the gas inertial force seems to have very complicated effects on the absolute instability.

For the para-sinuous mode of annular liquid jet instability, the critical Weber numbers We_c are shown in Figure 5.14 for various flow parameters and fixed jet dimensions. The half jet thickness and liquid velocity U_l^* are chosen as the reference length and velocity scale for this result. It is seen from Figure 5.14A that the critical Weber number We_c increases with the Reynolds number Re for fixed inner gas velocities U_a. The result indicates that the liquid viscosity has stabilizing effect on the absolute instability of para-sinuous mode as for para-varicose mode for annular liquid jets and cylindrical liquid jets [57].

The effects of the inner gas velocity U_a on the critical Weber number We_c can be clearly seen from Figure 5.14B. For fixed three constant density ratios ρ and the other parameters, We_c approaches infinity at both $U_a = 0$ and $U_a = 2$. On the other hand, as U_a increases, but well within the range of $0 < U_a < 2$, the jet can be of either absolute or convective instability. The We_c curves are not exactly symmetric about $U_a = 1$, indicating that it is absolute velocity of, rather than relative velocity between, liquid and gas flow that determines the absolute instability of the jet. The effects of gas-to-liquid density ratio ρ can also be seen from Figure 5.14B. For $0 < U_a < 2$, the critical Weber number We_c decreases as ρ increases while for $U_a < 2$ but close to 2 ρ presents a tendency to increase We_c. This dual-effect of ρ, or opposing and promoting absolute instability of annular liquid jets, is similar to that for cylindrical liquid jets [57].

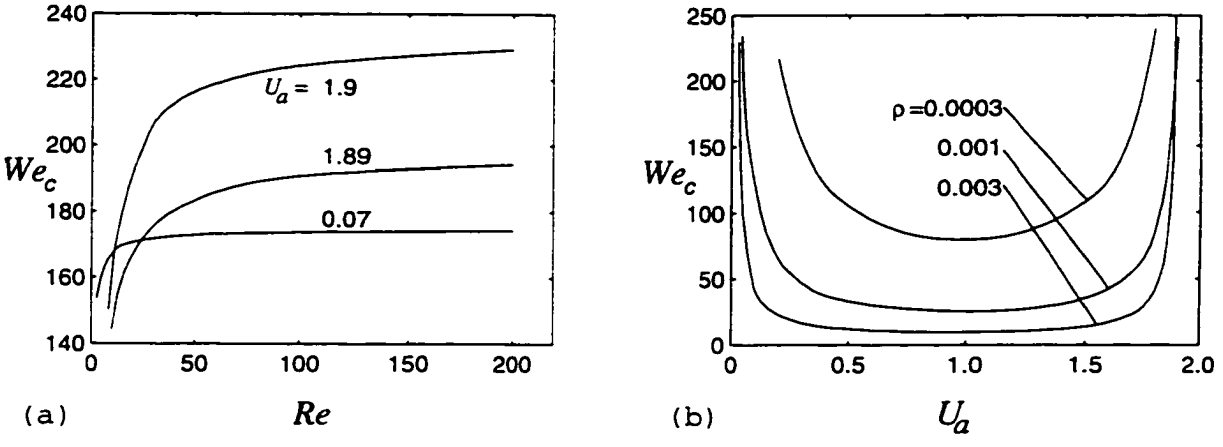

Figure 5.14: Critical Weber number with various flow parameters for para-sinuous mode. $r_a = 40$ ($r_b = r_a + 2$), $U_t = 1$ and $U_b = 0$. (a) $\rho = 0.001$; (b) $Re = 1000$.

Comparison between Figure 5.13 and Figure 5.14 shows that the critical Weber number for para-sinuous mode is one or two orders of magnitude larger than that for para-varicose mode. This means that under one condition, e.g., $U_a = 0$, $We = 1$ and the same other parameters as in Figure 5.14B, the para-varicose solution predicts convective instability for the jet while the jet is of absolute instability for para-sinuous mode. Apparently in this case, it is the para-sinuous mode or absolute instability that dominates the jet breakup process rather than the para-varicose mode or convective instability when the Weber number is smaller than the critical Weber number for para-sinuous mode.

5.3 Convective Instability

An annular liquid jet is of convective instability when the Weber number of the system is larger than the critical Weber number. A typical example for the convective growth rates k_i are shown in Figure 5.15, illustrating the effects of the inner gas velocities U_a based on both para-sinuous and para-varicose solutions. It is seen from Figure 5.15A

that k_i for para-sinuous mode possesses a minimum at $U_a = 1$ or without a velocity difference between the liquid and inner gas stream, and increases generally as the velocity difference increases. However, the growth rates k_i are different even for the same velocity difference, e.g. $U_a = 0.5$ and 1.5 as well as $U_a = 0.3$ and 1.7. This implies that not only the velocity difference but also the absolute velocity controls the convective instability for the para-sinuous mode. For the para-varicose mode as in Figure 3b, however, it is the velocity difference rather than the absolute velocity that determines the convective instability. The aerodynamic interaction between the liquid and gas basically enhances the jet breakup process for both modes. The results from Figures 5.15A and B also indicate that k_i for para-sinuous mode is at least one order of magnitude larger than that for para-varicose mode, showing that the para-sinuous mode outgrows the para-varicose one for convective instability, just as for

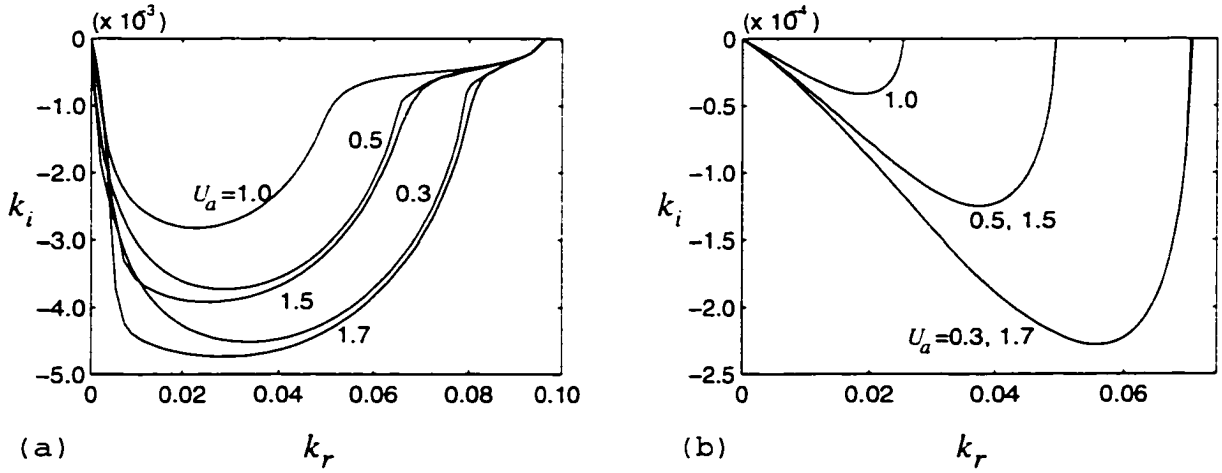

Figure 5.15: Convective wave growth rate at different velocities of the inner gas stream. $r_a = 40$ ($r_b = r_a + 2$). $U_\ell = 1$, $U_b = 0$, $Re = 1000$, $We = 100$ and $\rho = 0.001$. (a) para-sinuous mode; (b) para-varicose mode.

5.4 Summary

The linear instability analyses have been carried out for an annular viscous liquid jet exposed to both inner and outer gas streams of unequal velocities. Numerical results from solving the dispersion relations by Muller's method were presented for various flow conditions. The effects of the geometrical and various flow parameters were examined based on temporal, absolute and convective instability analyses.

The temporal instability analysis shows that there exist two independent unstable modes, para-sinuous and para-varicose, for the annular jet instability. The para-sinuous mode of interfacial waves outgrows the para-varicose one at relatively low gas-liquid density ratios and large Weber numbers. For the practical importance of large Weber numbers such as related to liquid atomization, the para-sinuous mode is always predominant. The curvature effects in general increase disturbance growth rate, and may not be neglected for the breakup process of an annular or conical liquid sheet. An annular jet with a sufficiently small thickness tends to break up much faster than the corresponding plane liquid sheet, in accordance with existing experimental observations. It is seen that not only the velocity difference across each gas-liquid interface but also the absolute velocity of each fluid phase is important for jet instability, although the effect of absolute velocity is secondary compared to that of relative velocity. Co-flowing gas at high velocities is found to significantly improve atomization performance while a low velocity co-flowing gas stream has little effect on jet instability when compared with the case where a gas stream of the same velocity is applied only on one side of the liquid jet. A high velocity gas inside of the annular liquid jet promotes the jet breakup processes more than gas outside of the jet with equivalent velocity. When there is a velocity difference across any of two gas-liquid interfaces, the presence of ambient gas medium always enhances the annular jet instability. The liquid viscosity has a stabilizing effect at high Weber numbers, while

at low Weber numbers it enhances the instability for para-sinuous disturbances under certain conditions. It is found that there exists a critical limit for Weber number, below which the surface tension is the source of instability. Whereas above it, the jet instability is suppressed by surface tension effect, and is promoted by the aerodynamic interaction between the liquid and gas phase. On the other hand, when there is no velocity difference across any of two gas-liquid interfaces or equal liquid and gas velocities, liquid and gas density as well as surface tension exhibit effects completely opposite to those with velocity discontinuity across interfaces. However, the viscous damping effect on jet instability always exists for the cases with and without the velocity differences at high Weber numbers. In practical twin-fluid atomization, where there always exists a velocity difference between liquid and gas , the atomization performance is therefore enhanced by an increase in the liquid inertia, density ratio and relatively large gas velocity, and hindered by the effect of surface tension and liquid viscosity.

A mesh-searching technique has been developed in this thesis to determine the absolute mode of instability. The critical Weber numbers are obtained under different flow conditions. It is found that the annular liquid jet has absolute instability when the Weber number for the flow system is smaller than the critical Weber number while it is of convective instability if the system Weber number is larger than the critical Weber number. The instability analyses indicate that both absolute and convective instability exist for para-sinuous and para-varicose modes under certain flow conditions. For para-sinuous mode, the annular liquid jet with an inner gas moving at relatively small velocity could have convective or absolute instability depending on specific flow conditions. However, the jet is of only absolute instability if the inner gas is either stationary or moves at sufficiently large velocity. Para-sinuous unstable waves outgrow para-varicose ones, and hence dominate the jet instability according

to both absolute and convective instability analysis. The liquid viscosity has a simple stabilizing effect on the jet instability while the gas inertial force shows fairly complex influence on the absolute instability of the jet. The convective growth rates for various inner gas velocities indicate that not only the velocity difference between, but also the absolute velocity of the liquid and gas, determines the jet breakup process.

PART II: EXPERIMENTAL INVESTIGATION

Chapter 6

Introduction

Sprays have been used in a wide range of practical applications. There are, for example, combustion sprays in the combustors of gas turbine aircraft engines, and non-combustion sprays for drying, food processing as well as painting and coating. Due to the increasing demand on not only combustion but also non-combustion sprays of high quality in diversity of practical applications, the design, testing and analysis of sprays have reached the highest levels in the overall field of spray science and technology. Large amounts of experiments are necessary to provide desired spray characteristics for different usage. For each specific design of an atomizer, the manufacturers conduct on-site testing of individual nozzles by measuring detailed spray characteristics such as spray angles, shape, penetration, size, velocity, number density and liquid flux distributions under different liquid and gas flow rates. The measured data are then analyzed, compared and used to modify the atomizer design. There are various means to take these measurements, which are developed with one having different emphases from the others. The most versatile and reliable one in recent years is Phase Doppler Particle Analyzer (PDPA) based on laser light scattering interferometry, although Laser Diffraction Particle Analyzers still plays an important role in

spray measurements. The two-component PDPA makes simultaneous measurements of size and velocity of individual droplets possible. The technique is similar to conventional dual-beam Laser Doppler Velocimeter (LDV) except that four photo-detectors are located in separate places of the receiving optics assembly. Coupled with photographic and imaging techniques, quantitative and qualitative information can be obtained for the liquid jet breakup process or early stage of spray formation.

6.1 Basic Concepts

A liquid jet can be formed by injecting liquid through a nozzle into a surrounding gaseous environment. Regardless of its geometric shape, it always breaks up immediately at the nozzle exit or some distance downstream from the nozzle due to its inherent instability. How fast it collapses depends on what instability mode disturbance waves at the gas-liquid interface(s) have and how fast the disturbances grow. If the jet is of convective instability, the disturbances will grow downstream through space until the disturbance amplitude is large enough to cause necking of the liquid jet. In this case, bubbles may be formed after the jet is pinched-off if there exists a gas core inside of the liquid as in an annular liquid sheet. The length from the nozzle exit to the point of pinching-off is defined as **breakup length**. The length in axial direction of the flow between two adjacent peak or valley of the disturbance wave is known as **wave length**, and the corresponding radial change of the interface off the jet equilibrium position is related to **wave growth rate**. Usually bubble diameter, jet breakup length, disturbance wave length and growth rate are the main parameters considered to characterize jet breakup processes. The state that there is wave-type of disturbance growth present at the gas-liquid interface is named **bubble formation regime** of jet breakup process. Whereas the state for which an irregular

annular liquid sheet is formed is called **annular jet formation regime**. However, if the liquid jet disintegrates immediately at the nozzle exit into a train of droplets, the jet breakup process is in **atomization regime**. The instability mode for this case is hard to identify. The jet might have absolute instability or perhaps non-linear effect becomes dominant.

Liquid atomization is a process that a liquid jet breaks up immediately at a nozzle exit into a train of drops of fine sizes. The clouds of drops is called a **spray**. There are many different parameters that characterize sprays depending on what applications the sprays are used for. Basically, the parameters listed below are considered important and universal for almost every application.

(a) Mean velocity: $\bar{U} = \sum N_i U_i / \sum N_i$

(b) RMS velocity: $\sqrt{\sum (U_i - \bar{U})^2 / N}$

(c) Turbulent intensity: the ratio of RMS to mean velocity, indicating the velocity fluctuation of the flow

(c) Mean diameter, arithmetic average diameter of drops passing through the measurement volume: $D_{10} = \sum N_i \sum D_i / \sum N_i$

(d) Sauter Mean Diameter: $D_{32} = \sum N_i D_i^3 / \sum N_i D_i^2$

(e) Number density: the number of drops passing through per unit measurement volume.

where i denotes the velocity or size range considered, N_i is the number of drops in velocity or size range i.

The most reliable instrument, which can provide both droplet velocity and size information simultaneously, is Phase Doppler Particle Analyzer (PDPA), or Particle

Dynamics Analyzer as it is often called as well. The principles of PDPA is described briefly in the following section.

6.2 Phase Doppler Technique for Spray Characterization

The Phase Doppler Particle Analyzer (PDPA), which is developed based on the principles of Laser Doppler Anemometers, is one type of non-intrusive optical technique to measure the local and instantaneous velocity and size of particles suspended in flows. It has many advantages, over traditional measurement techniques (e.g. Malvern Laser Diffraction), which are:

(a) No probe in flow (non-intrusive)

(b) High spatial resolution

(c) Velocity components can be measured precisely.

The disadvantages of this technique are:

(a) The accuracy of measurements depends on the degree of particle sphericity

(b) The apparatus and flow field must be transparent

(c) System is quite expensive.

The operation principle of PDPA for velocity measurements are based on the theory developed by an Austrian physicist, Christian Doppler. In 1842, when he began to review the wave theory of light, by which color perceived by the eye is

dependent on the frequency of pulsation which stimulates it. he found that anything, which changes the interval between these pulsation. changes the perceived color. If the light source and observer are both at rest. then the observed and the emitted frequency are the same. If the observer moves towards the source. however. the frequency will increase. and if he moves away it will decrease. Movement of the source will produce the similar effects. This thought becomes Doppler's theory today and is used for measurement of motion by comparing the frequency of scattered light to the frequency of light incident on the scattering particles.

For simultaneous particle size and velocity measurements. a receiving optics unit is needed in addition to what a convectional Laser Doppler Velocimeter (LDV) has. The familiar dual-beam scattering arrangement for LDV is used. The two beams of equal intensity but different frequency intersect and form an interference fringe pattern or measurement volume. When a transparent spherical particle passes through the measurement volume. the scattered light from the particle will form a moving interference fringe pattern. Since the Doppler frequency shift of this scattered light interference fringe pattern is a function of the beam intersection angle. light wave length. and velocity of the particle. the velocity of the particle can be obtained by measuring the Doppler frequency shift using a photodetector to collect the scattered light and convert the light signals into electric signals. Two or more photodetectors. placed at separate places. will get the scattered light signals of the same Doppler frequency shift but with a relative phase shift. The phase shift contains the information on drop size. and therefore can be used to determine the diameter of the drop.

In this work. annular water jets exposed to air streams inside of the water jets are investigated experimentally by two means. One is photographic technique. and the other laser Doppler interferometry. In the first part of the experiment by photographic technique. a number of photographs are taken at different water and air flowrates for

a fixed nozzle dimension using Pentax-A 135 camera. The bubble diameters, jet breakup lengths, disturbance wave length and growth rates are then measured from the magnified projections of the negatives using a slide projector. In the second part of the experiment, Dantec Particle Dynamic Analyzer (PDA), one type of Phase Doppler Particle Analyzer, is utilized to measure spatial distributions of droplet sizes and velocities for various water and air flowrates. SIZEware software provided by Dantec company is used on a PC computer to control the entire process of setting up the tests, acquiring and processing data. The droplet size and velocity data after data processing are analyzed and typical results are presented in the next chapter.

Chapter 7

Literature Review

The current industrial applications of sprays are almost exclusively based on extensive experimentation for a given fluid and nozzle to obtain empirical correlations of spray characteristics under certain flow conditions. Since empirical correlations are different from one nozzle to another and one fluid to another, and depend on specific flow conditions, considerable amounts of experiments are necessary. Previous works available in the literature in this research area fall into two main categories: liquid jet breakup processes, and characterization of the resultant sprays from the jet breakup. The studies of liquid jet or sheet breakup can provide fundamental physical insights for spray formation and characteristics, and are usually taken as the first step for the studies of sprays.

Over the years, the breakup of liquid jets or sheets and characteristics of the resultant sprays in twin-fluid atomization have attracted considerable attention because of their wide applications in power and propulsion systems. Diverse experimental investigations have been conducted using different structures of atomizers under various flow conditions. Regardless of the complexity of the structure of real atomizers, there are basically three types of nozzles which can produce different geometrical shapes of

liquid jet or sheet, such as cylindrical jet, plane sheet and annular jet or sheet. Previous experiments available in the literature are mostly about the breakup processes of cylindrical liquid jets and plane liquid sheets as well as the characteristics of the resultant sprays. There are only a few works directed at the breakup processes and spray formation of annular liquid jets. Especially, there are no works reported so far for simultaneous drop size and velocity measurements using Phase Doppler Particle Analyzers, which has become almost a standard instrument to characterize sprays in recent years. However, the review about those works for cylindrical liquid jet and plane liquid sheet are necessary because the fundamental physics of these three types of jets or sheets are the same.

As Lefebvre summarized in his article [1], the principle factors governing the mean drop sizes produced by twin-fluid atomization are the air velocity, air-to-liquid ratios, and surface tension, based on experimental data obtained on many different types of atomizers in which air is used as the principle driving force for atomization. For the classical mechanism of jet breakup, involving flow instabilities and wave formation, atomization occurs slowly and is strongly influenced by variations in liquid viscosity, air density, and the initial diameter (or thickness) of the liquid jet (or sheet). However, if atomization occurs very rapidly, these parameters have little effect on mean drop sizes of sprays.

7.1 Previous Experiments on Cylindrical Jets and Plane Sheets

The instability of capillary liquid jets or cylindrical liquid jets was studied by Sterling and Sleicher [10]. Weber's theory [9] based on the linear stability theory was modified by considering velocity-profile relaxation due to fully developed laminar flow inside

the nozzle passage. The continuous jet lengths predicted by the modified theory were compared with the experimental measurements using photographic techniques. They found that the jet length increases with the jet velocity and reaches a maximum at some critical jet velocity. The predicted values of the maximum jet length and critical velocity by Weber's theory disagree with the experiments. But those predicted by the modified theory agree well with the experiments.

Focusing on cylindrical liquid jets in the atomization regime, Reiz and Bracco conducted the experiments using fourteen sizes of cylindrical nozzles for five mixtures of water and glycerol as working liquids and three kinds of gases as the ambience [64]. Spray angles were measured from the photographs taken under various conditions, and compared with the predictions by linear instability theory. A mechanism that combines liquid-gas aerodynamic interaction with nozzle geometry effects was identified to be compatible with their experiments.

Another work by Shavit and Chigier studied the disintegration processes of cylindrical liquid jets surrounded by annular air jet in an airblast coaxial atomizer [65]. Fractal dimensions of gas-liquid interfaces were measured in the breakup region of disintegrating liquid jets by photographic techniques. The liquid intact length or jet breakup length and drop sizes of sprays were also measured. Their results showed that increasing the air velocity results in a higher fractal dimension and lower intact length as well as smaller drop size. Whereas the increase in the liquid velocity causes the breakup point and the location of the peak value of the fractal dimension are relatively far downstream from the nozzle exit.

A recent work by Lai et. al [66] presented an experimental study of drop transport phenomena in a research simplex atomizer with and without atomizing air. The working liquid used was methanol atomized in air. A two-component Phase Doppler Particle Analyzer was utilized to measure droplet sizes and velocities at different spa-

tial locations in the spray with a fixed air-to-liquid mass ratio. For each measurement at one location, 30,000 validated samples were collected except at a few locations near the outer boundary of the spray. The analysis of the histogram data showed that the transport of part of the smaller drops from the outer region to the central region was the key process responsible for the increase in Sauter Mean Diameter, the drop number density and velocity fluctuation downstream.

As for the disintegration of plane liquid sheets, a number of workers have been studying the Kelvin- Helmholtz wave growth on liquid sheets [32, 33, 67], the breakup processes and liquid atomization [49, 68, 44, 69] using either photographic techniques or phase Doppler interferometry. Starting from Squire [32] in 1953, a linear instability analysis was conducted for a two-dimensional moving film, and the predicted wave lengths were compared with the measured values from photographic measurements. The comparison showed that the predicted wave lengths were of the same order as the measured value.

Rizk and Lefebvre performed an experimental investigation on airblast liquid atomization [68]. Droplet sizes were measured using the light-scattering or Laser diffraction technique. Two prefilming airblast atomizers were specially designed to produce a flat liquid sheet with both sides of the sheet exposed to high velocity air. By one of them, a thin liquid film of uniform thickness can be produces while in the other one the film thickness can be adjusted. It was found that the initial liquid film thickness plays an important role on mean drop size and drop-size distribution. High values of liquid viscosity and liquid flow rate result in thicker films. Whereas high air velocity and density are conducive to thinner films which are better for liquid atomization.

The development, stability and disintegration of plane liquid sheets exposed to high-velocity air streams on both sides were studied by Mansour and Chigier [44]. Microphotography was used to assess the global structure of the spray. Detailed

measurements of mean drop size (SMD) and velocity for sprays were made using a phase Doppler particle analyzer. Without air flow the liquid sheet converges toward the axis as a result of surface tension forces. The convergence length increases with the liquid flow rate. With air flow a quasi-two-dimensional expanding spray is present. The air flow was found to be responsible for large ordered and small chaotic cellular structures. These structures are bounded by large diameter ligaments containing thin membranes inside. The ligaments break up into large drops in the spray and the membranes contribute to the formation of the small droplets. The characteristics of these drops in sprays were then examined by using a phase Doppler spray analyzer. The measurements of Sauter mean diameters (SMD) and mean velocities were taken at different locations for various liquid and air flow rates. The results showed that for a fixed liquid flow rate, the SMD decreases gradually as the air/liquid mass ratio is increased. However, for each liquid flow rate, there is a limit to the effectiveness of the increased air flow rates. The SMD shows an initial decrease followed by a gradual increase along the spray axis. The droplet velocity profiles were found to be mainly dependent of the air velocity profiles and to be Gaussian in form with velocity maxima on the spray axis. A similar work was also presented by Stapper and Samuelsen [69], for the breakup of a two-dimensional liquid sheet in the presence of co-flowing air shear.

7.2 Previous Experiments on Annular Jets

Motivated by scientific interest in the fluid motion of a hollow jet, and by the potential utility of a method for the mass production of rigid shells of high quality, Kendall [20] conducted an experiment on an annular water jet formed by an annular nozzle of $4.0mm$ in diameter with a air flow at its core. The photographs taken for the jet

showed that periodic, axisymmetric oscillations arise spontaneously within the liquid sheet emerging from the annular section of the nozzle and grow rapidly along the axial direction such that a sealing-off and encapsulation of the core gas occurs within a few jet diameters, followed by a pinchoff of the liquid between adjacent bubbles. However, this experiment of bubble formation was carried out for relatively low liquid and gas velocities such that uniform spherical liquid shells or bubbles occur as the results of annular sheet breakup, and no sprays of a multitude of droplets with various sizes were produced.

Lee [70] studied the interfacial instabilities on the breakup of annular liquid sheets subject to internal and/or external gas flows. The experiments were conducted for a liquid sheet emerging from an annulus of $12.7mm$ in inner diameter and $22.2mm$ in outer diameter formed by two concentric tubes. A linear temporal instability analysis was carried out for a better understanding of air-assisted atomization. Three flow regimes, i.e., Rayleigh, intermittent and atomization, were identified and a flow map was constructed based on the photographic measurements. The comparison of the predicted bubble formation frequencies with the measured values indicated reasonable agreement of theory with experiment except when the air velocity was increased where the intermittent regime was approached.

To explore experimentally the mechanisms of annular liquid sheet instability and spray formation, Lavergne et al. [71] investigated an annular liquid sheet, $400\mu m$ thick, breaking up in two co-flowing air streams. The experiments were conducted using a high-speed video camera for the jet breakup characteristics and Phase Doppler Particle Analyzer (PDPA) for the characterization of the resultant sprays. They confirmed that there exist three different flow structures or atomization processes under various air flow conditions as Lee [70] observed. The observed wave frequencies, amplitudes, and breakup lengths were found to be dependent on the flow conditions

for each flow regime. The PDPA measurement indicated the representative spray behavior of an airblast atomizer. The mean axial velocity profile far down stream was found to be similar to that for plane liquid sheets. The Sauter Mean Diameters measured for droplets exhibited a modified size distribution due to the swirl effect, and larger diameters were present near the spray boundaries than near the spray centerline. However, very limited data were present in their work.

It is evident that the existing experimental investigations on the annular liquid sheet breakup are very limited. The available information is insufficient to understand overall mechanisms of annular liquid sheet disintegration and the spray formation. In this work, a moving annular liquid sheet injected from well-designed annular nozzles of different sizes into surrounding gas streams is investigated experimentally. Photographic technique and the Phase Doppler Particle Analyzer are applied to study the liquid sheet disintegration process and characterize the resultant sprays.

Chapter 8

Experimental Facilities and Techniques

Annular nozzles, liquid and gas supply facilities are designed and constructed in this work. Two annular nozzles are made with the same structure but different sizes. The one with a larger diameter is mainly for the investigation of the liquid jet breakup mechanism by photographic technique while the other is for the study of characteristics of the liquid spray by applying Laser-Doppler shift principle. The instruments used are a photographic camera, Pentax-A 135, for the former, and a phase Doppler particle analyzer, Dantec Particle Dynamics Analyzer, for the latter. The experimental configuration, operating principles of the instruments, test conditions and procedures are described in this chapter.

8.1 Design and Structure of Nozzle

The nozzle used in this work is the one with an annular section for liquid flow, which is formed by inserting a tube in the center of a large pipe. It is designed specially with a contraction for the liquid flow to reduce non-uniformity in the mean flow and also the turbulence level of the flow. For the purpose of this experimental investigation, the contraction is essential for the annular nozzle to generate liquid jets, and form nice bubbles or sprays with fine sizes of droplets after the jets break up.

8.1.1 Nozzle Design

The method for the design of the nozzle contraction in this work is based on the study on the design of three-dimensional wind tunnel contractions by Downie et al. [72]. In their study, it was shown that producing an optimal geometric shape for the flow channel is important since the shape of the contraction has a critical effect on the velocity distribution. Pairs of matched elliptic arcs were used and proved to be a simple way of achieving satisfactory profiles for the contraction. However in this work, this is modified to meet special requirement of large contraction ratio, e.g., 15.7. As shown in Figure 8.1, two elliptic arcs (AB and CD) are connected in between by a straight line (BC), and this is seen to produce also a very smooth contraction.

8.1.2 Nozzle Structure

Shown in Figure 8.1 is the sectional view of annular nozzles. The annular section for the liquid flow is formed by inserting a pipe in the center of the outer one. With the size of the outer pipe fixed, the thickness of the annular liquid sheet can be adjusted by using different sizes of central core pipes. The dimensions of the two nozzles used

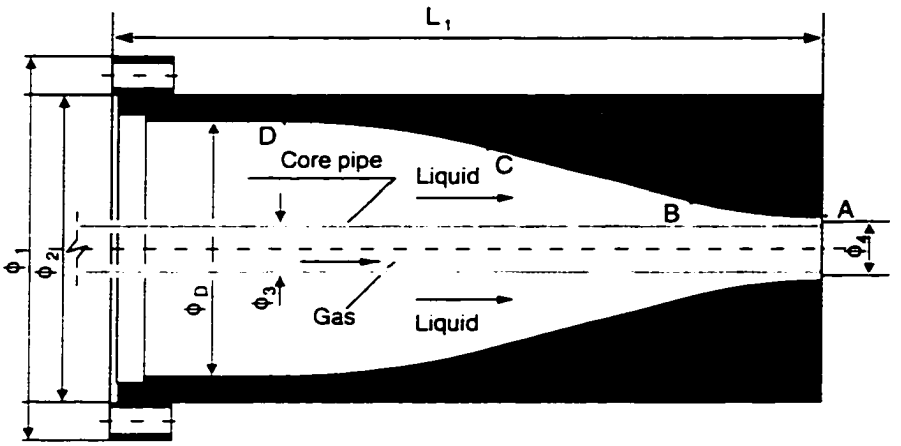

Figure 8.1: Sectional view of annular nozzle

in this work are listed in Table 8.1. Note that L_B, L_C and L_D denote the lengths from Point B, C and D to the nozzle exit respectively, and Φ_A, Φ_B, Φ_C and Φ_D are the corresponding diameters.

Table 8.1: Main Dimensions of the two Annular Nozzles (Unit: mm)

Dimensions	L_1	Φ_1	Φ_2	L_D	Φ_D	L_C
Nozzle A	105	60	48	80	40	50
Nozzle B	105	60	48	80	40	58
Dimensions	Φ_C	L_B	Φ_B	Φ_A	Φ_3	Φ_4
Nozzle A	32	20	15.4	10.00	9.525	8.83
Nozzle B	33	25	10.8	2.54	2.375	1.5875

The uniformity of the flow and turbulence level in the test section are also improved by placing a honeycomb and fine wire-mesh screens upstream of the inlet to the nozzle.

8.2 Setup of Test Apparatus

The experimental apparatus shown in Figure 8.2 consists of a nozzle (see Figure 8.1 for the nozzle structure) with its annular section connected to the water supply facility and the central core pipe linked to the compressed air supply. The water in the water tank is pressurized by the compressed air in order to maintain as steady as possible flowrates during tests. When this pressurized water flows through the annular section of the nozzle, an annular water sheet (also called jet) or water spray is formed with its inside surface exposed to the air stream. A floating flowmeter is mounted on each pipeline connected to the nozzle to measure the water and air flow rates. Both water and air flow rates are adjusted roughly by using the choke valves upstream of the flowmeters, and then regulated finely by the standard valves built in with the flow meters. The water during the experiment is collected by an open tank and then drained out directly after the test is completed every time.

8.3 Instrumentation for Measurements

The experiments performed in this thesis contain two parts. For the first part, a Pentax-A 135 camera is used to take directly photographs of the water jets at relatively low water and inner air velocities. In the second part, a Dantec Particle Dynamics Analyzer (PDA) is the instrument utilized to characterize the sprays formed after the break up of water jets in the case of relatively high water and air velocities. The specifications for all the instruments and auxiliary are presented in Appendix E.

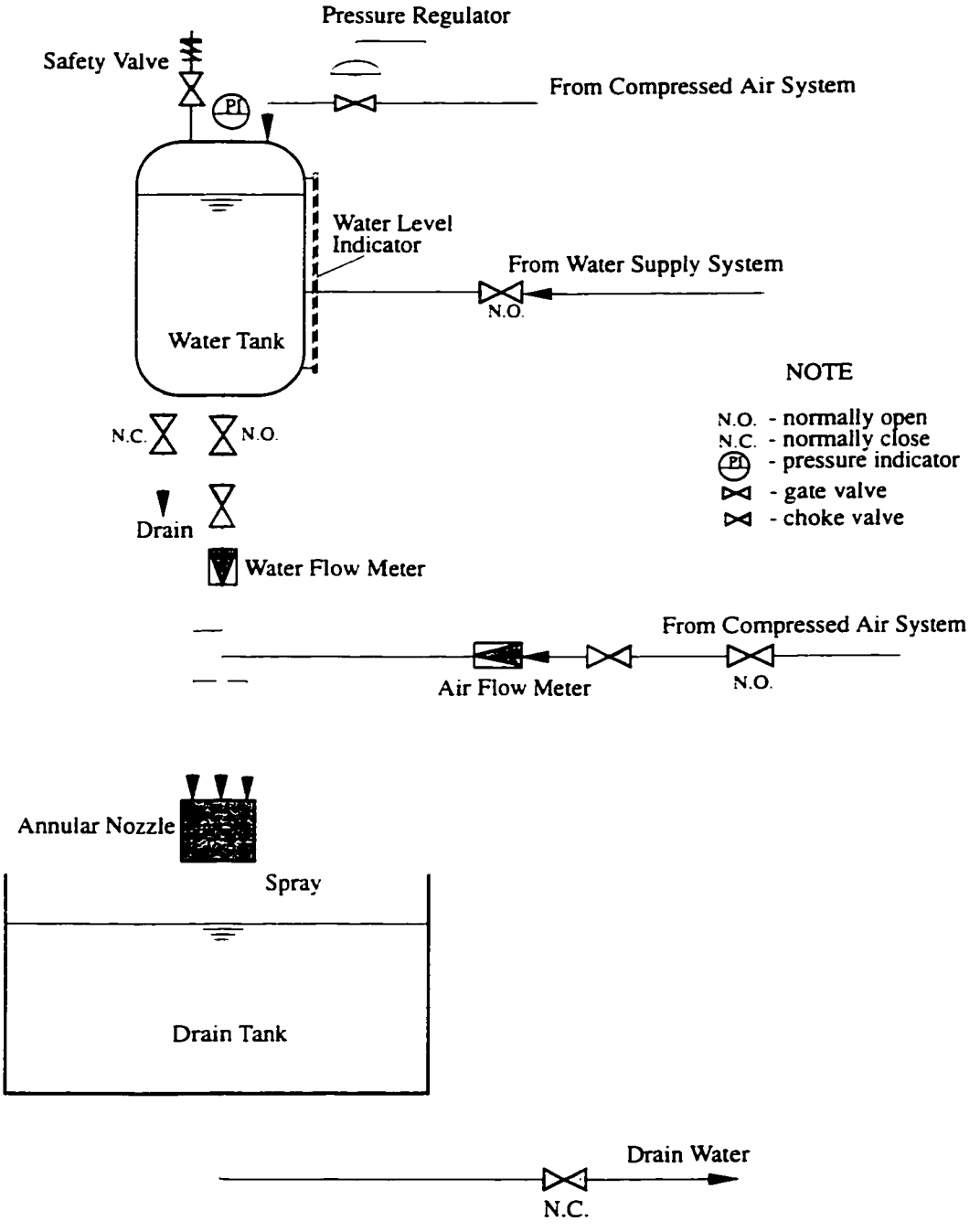

Figure 8.2: Experimental setup for the formation of liquid jets or sprays

8.3.1 Photographic Technique

In this experiment, the annular nozzle is held vertically so as to form the liquid jets in the vertical direction. The Pentax-A camera is then set at certain height in the plane orthogonal to the jet center plane to avoid deflection of the jet image as much as possible. When taking photographs, the bulb shutter speed is selected for the camera. Therefore, a strobe is necessary to produce light pulses of adjustable time duration and to allow single short exposure photograph of an instantaneous water jet to be taken. In addition, to improve the quality of the jet photos, the maximum aperture of the camera is used to gather as much light reflected from the jets as possible. Since the grain size of ISO 400 black and white 35 mm films is estimated to be $O(5\mu m)$, no blurring due to the motion of the liquid sheet should be present.

The simplest way to make measurements of the jet is to use a slide projector to magnify the negatives, and then take measurements from the magnified projections. By this method, the bias errors from human eyes could be reduced.

8.3.2 Particle Dynamics Analyzer System

The Dantec Particle Dynamics Analyzer (PDA) used in this work is similar to a conventional laser Doppler velocimeter (LDV) except that three photo-detectors are used in the receiver unit to measure droplet sizes and velocities simultaneously. It consists of three units, Transmitting Optics, Receiving Optics and Signal Processor as shown in Figure 8.3. The operation principle of this PDA and its three units are described in the following section.

(a) PDA Operating Principle

In the PDA transmitting optics unit, a linearly polarized helium-neon laser gun provides the coherent light source. This beam is split into two parallel beams of

equal intensity with one beam frequency-shifted by a Bragg cell. The resulting pair of beams pass through a spherical lens and intersect at the focal point where the measurements are to be taken. A set of plane parallel interference fringes with a spacing determined by the laser wavelength and the angle between the two beams is produced in the crossing region, and forms an measurement volume in the shape of a three-dimensional ellipsoid.

When a droplet passes through the measurement volume, the scattered light forms an interference fringe pattern that sweeps past the detectors in the PDA receiving optics unit at the Doppler frequency, which is a unique function of the beam intersection angle, laser wavelength and droplet velocity. Thus the droplet velocity is determined from the Doppler frequency. Each detector produces a similar Doppler burst but with phase shift between them. For a given optical configuration and droplet index of refraction, this phase shift is proportional to the droplet diameter. Three detectors are used to ensure that diameter ambiguity does not occur in sprays where phase shifts greater than 360 degrees may occur. By the means of three detectors, the droplet size and velocity are able to be measured simultaneously.

The optical signal collected by the receiving optics unit is converted into electric signal by a photomultiplier. The resulting Doppler signal is then processed by a signal processor, and downloaded into a computer for data storage and analysis. Meanwhile, the Doppler signal can be monitored graphically in real time on an oscilloscope. The detailed theoretical description of PDA principle can be found elsewhere [73].

(b) PDA Hardware and Auxiliary

The Dantec PDA system used in this experiment is shown in Figure 8.3. It is operated in near backward backscatter mode with the receiving optics unit located on the same side as the transmitting optics unit. The Dantec 55X transmitting optics provides a $10mW$ helium-neon laser as the coherent light source. By a beam splitter,

this laser beam is split into two beams of equal intensity. After one of them is shifted by a frequency of $+40MHz$ through a Bragg cell, the two parallel beams are focused and the measurement volume is formed by the Dantec 55X57 front lens of $310mm$ focal length. In the Dantec 57N10 PDA receiving optics unit, the scattered light from a particle at the intersection point or in the measurement volume is collected by the Dantec 55X57 front lens and then focused at a slit aperture by a focusing lens of $310mm$ focal length. This aperture restricts the detection of light scattered from other than the sample volume. There are three 55X08 photomutipliers located separately in the receiving optics unit, which convert the light signal into electric signal or Doppler signal. The Doppler signal is then transferred into Dantec 58N10 PDA Signal Processor, processed there and downloaded into a PC-AT type of computer for the data storage and analysis. On the other hand, the Doppler signal from the Signal Processor can also be transferred to an oscilloscope for graphical monitoring. For the detailed specifications of each unit, refer to Appendix E.

The traversing system used in this work was originally designed by Billenness [74]. It is a three-dimensional manual system made of rigid $13mm$ thick aluminum and precision lead screws with anti-backlash nuts. The axis in each direction is equipped with a steel rule to locate the measurement volume to the nearest millimeter. The total length of traverse is $600mm$ in x', $350mm$ in y' and $270mm$ in z' direction. By using a graduated dial built on the lead screw, the measurement volume could be positioned with a resolution of $0.05mm$ in x' direction and $0.013mm$ in y' and z' directions. The accuracy of the movement was checked with a dial indicator, and was generally better than $0.025mm$ [74]. The position of the nozzle relative to the traverse is shown in Figure 8.4. x' and y' axis of the traverse are along two orthogonal radial directions of the spray, and z' axis is along the spray axis and opposite to the flow direction.

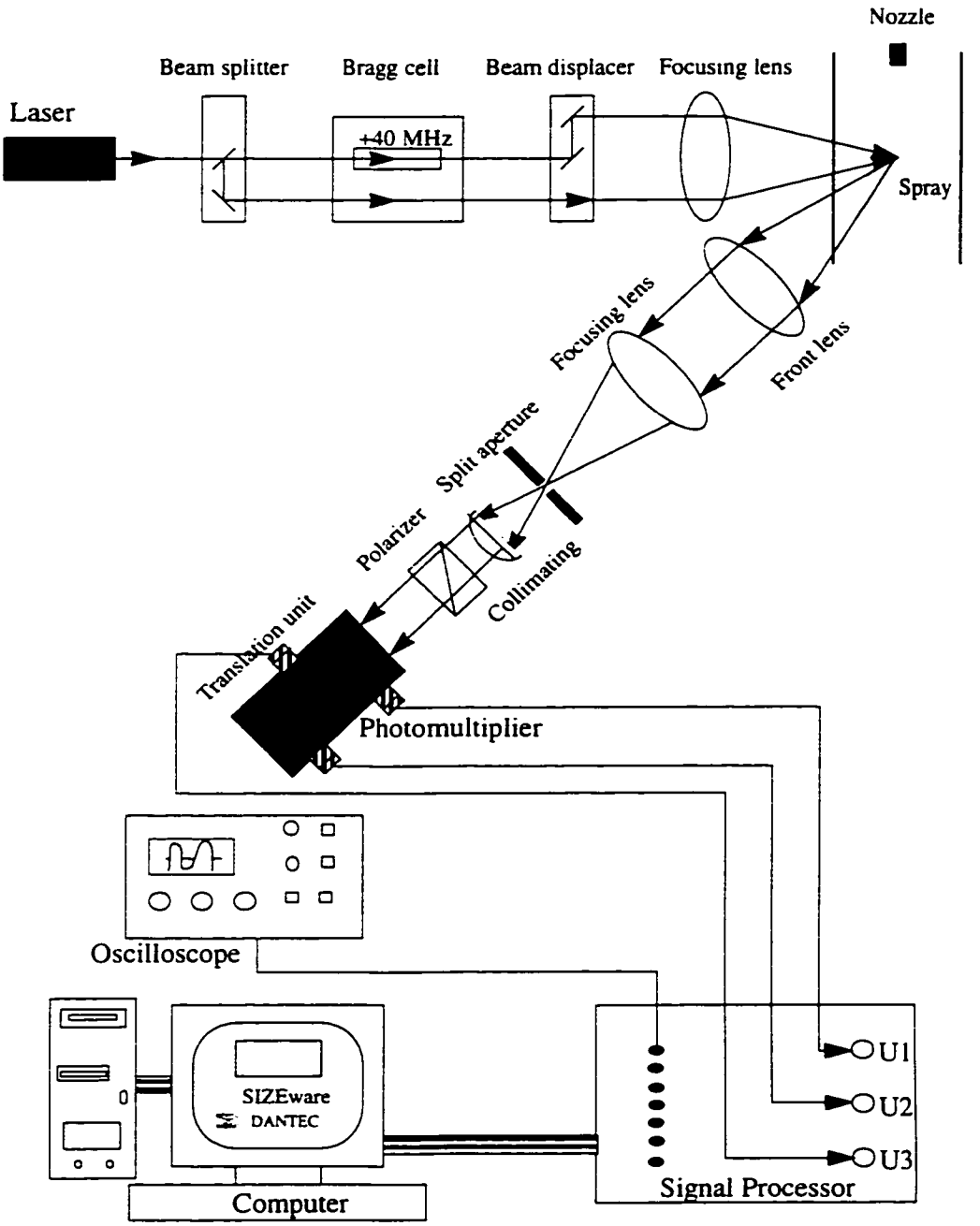

Figure 8.3: Schematic of the PDA setup

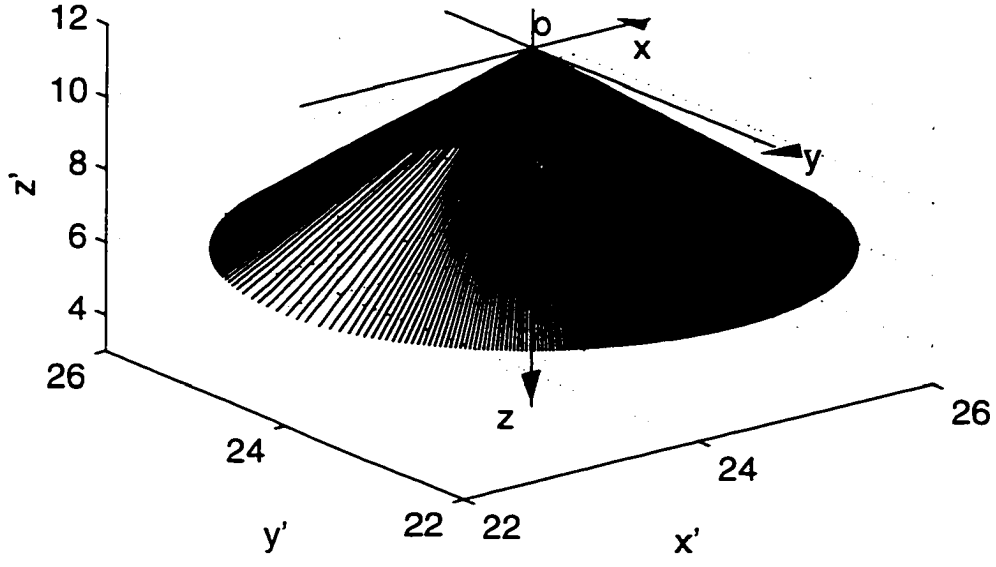

Figure 8.4: Sampling positions for PDA measurements

(c) PDA Software

The software, named SIZEware, is written in Fortran 77 language and runs on PC-AT type computers supported by DOS. It controls PDA setup, data acquisition and processing. Specifically, it has six main functions: instrument control, data acquisition, file creation and maintenance, conversion of raw data, processing of converted data and graphic output of results. The statistical results provided by SIZEware are mean, RMS skewness and flatness of measured velocity; cross moments of velocities; mean, area, volume and Sauter mean diameter; as well as concentration, volume fraction, void fraction and volume flux.

8.4 Test Procedure and Conditions

The experiment conducted in this work consists of two parts. In the first part, the breakup process of the annular water jet exposed to the moving air stream in its centre is studied by photographic technique. In the second part, characteristics of non-burning annular water sprays in air is examined by applying Phase Doppler diagnostics. For each part of the experiment, one annular nozzle of the fixed geometry and size is used to produce water jets or sprays under various flow conditions. As shown in Table 8.1, there are two sizes of annular nozzles. Nozzle A is for study of the jet breakup process while Nozzle B is for the spray characterization.

The test procedure for both parts of the experiment is almost the same except that for the laser Doppler measurements, the traverse system is needed to locate the measurement volume at different positions within the spray. The procedure listed below is common to both parts of the experiment before the measurements are taken.

(1) Clean the water tank using the compressed air and ensure there is no rust remaining in the test facilities shown in Figure 8.2.

(2) Check the flow path inside of the nozzle and connect a right size of nozzle to the pipelines

(3) Mount a pair of flowmeters with right flow ranges upstream of the nozzle

(4) Fill the water tank by the tap water to about two thirds of the total water volume

(5) Check the pressure of the compressed air supply and set it at a desired value

(6) Open the valve at the pipeline from the compressed air supply to the water tank and leave it open during the test to maintain the pressure inside of the water tank

(7) Wait for about 30 *min* for the pressure in the water tank to be stabilized.

8.4.1 Flow Visualization--Photography

Flow visualization is achieved by photographing the water jets generated by Nozzle A (see Table 8.1 for its detailed dimensions) at relatively low water and air velocities. After following the test procedure described in the previous section, it is necessary to turn off all the lights and turn on the strobe with a desired light frequency and intensity. Then numbers of photographs can be taken by Pentax-A 135 camera, which is set at the bulb shutter speed, for various water and air flow rates. The camera shutter and strobe are synchronized. When the negatives of the photos are ready, the measurements are made from the magnified projections of the negatives by a slide projector. The detailed test conditions are summarized in Tables 8.2 to 8.4.

Table 8.2: Working Fluids and Conditions for Photographic Measurements

Liquid	tap water
Gas	compressed air
Room Temperature	$21°C$
Pressure in Water Tank	40 *psig*
Pressure of Compressed Air	20 *psig*

Table 8.3: Working Conditions for Pentax-A 135 Camera

Focus Length	0.6 m
Aperture	3.5
Shutter Speed	bulb
Film Speed	ISO 400

Table 8.4: Water and Air Flowrates Used for Photographic Measurements

Water Flow Rate (10^{-5} m^3/s)	Air Flow Rate (10^{-4} m^3/s)
1.262 (0.2 GPM)	2.360, 4.720 (0.5, 1.0 $SCFM$)
1.577 (0.25 GPM)	2.360, 4.720, 7.080 (0.5, 1.0, 1.5 $SCFM$)
1.893 (0.3 GPM)	2.360, 4.720, 7.080 (0.5, 1.0, 1.5 $SCFM$)
2.524 (0.4 GPM)	2.360, 4.720, 7.080, 9.440 (0.5, 1.0, 1.5, 2.0 $SCFM$)

8.4.2 Droplet Size and Velocity Measurements

At relatively high water and air velocities, water sprays are produced by using Nozzle B (see Table 8.1 for its dimensions). The Dantec Particle Dynamics Analyzer (PDA) needs to be aligned up, and the system to be checked following the procedure on Page 92 prior to making measurements. During the test, the traverse is used to move the PDA measurement volume through the space within the spray so that Doppler frequencies are measured at different spatial locations for each pair of water and air flow rates. SIZEware software is running on the PC-AT type computer during the test for the data acquisition. According to the size range of droplets to be measured, the angular separation of detectors indicated by reading on the micrometer dial on back of 57N10 PDA Receiving optics should be adjusted and match that is set for Angle Adjustment in Receiving Optics Setup window of SIZEware. The Bandwidth parameter in Bandwidth setup window should also be selected corresponding to the velocity range for every test. The key parameters set for PDA system and test conditions for the Doppler frequency measurement are presented as follows. For details about how to use SIZEware, refer to SIZEware User's Guide [75].

(a) Key Parameters Set for PDA System

The parameters listed in Table 8.5 are main parameters set for all the PDA measurements in this work. The other parameters, such as Angle Adjustment and Bandwidth, need to be selected whenever the test conditions are changed, which affect the droplet sizes and velocities. The available option for Angle Adjustment is any one number in the range of 0 to 2 mm corresponding to a maximum diameter. The Bandwidth parameter can be any one number of 0.12, 0.40, 1.20, 4.0, 12.0 and 36.0 corresponding to velocity range of -21.4 to 107.4 m/s.

Table 8.5: Key Parameters Set for PDA System

Laser light	Type	He-Ne
	Power	10 mW
	Wave length	632.8 nm
	Diameter of focused Laser beam	0.25 mm
	Laser beam intersection	5.53°(half angle)
Measuring volume	Diameter	0.25 mm
	Length	2.6 mm
Transmitting optics	Fringe spacing	3.5807 μm
	Number of fringes	70
	Beam separation	55 mm
	Focus length of front lens	310 mm
	Bragg cell	40 MHz
	Polarization angle	90°
Receiving optics	Focus length of front lens	310 mm
	Polarization angle	90°
	Scattering angle (effective)	150
	Particle density	1 g/cm^3
	Particle/medium refractive index	1.334/1.0
	Polarization orientation	perpendicular
	Fringe rotation angle	0

(b) Working Fluids and Test Conditions

The PDA measurements in this part of the experiment are performed for different water and air flow rates at different spatial locations within the water sprays, which

are determined by the coordinates in the x', y' and z' direction of the traverse. The relative position of Nozzle B or the resulting spray to the Cartesian (x', y', z') coordinate is shown in Figure 8.4. The other coordinate (x, y, z) with its origin at the center of the nozzle exit ($x' = y' = 623.82\ mm$ (24.56 in) and $z' = 278.57\ mm$ (10.968 in)) is also used for the purpose of plotting and analyzing the test data (see Figure 8.4 for the relative position of two coordinates). The working fluid and test conditions are summarized in Tables 8.6 to 8.9.

Table 8.6: Working Fluids and Conditions for PDA Measurements

Liquid	tap water
Gas	compressed air
Room Temperature	$21°C$
Pressure in Water Tank	60 $psig$

Table 8.7: Test Conditions for PDA Measurements in two Orthogonal Radial Directions

$z' = 128.016\ mm$ (5.040 in) $z = 151.575\ mm$			$Q_f = 388\ ml/min$ $Q_a = 26200\ ml/min$		
x' (mm)			y' (mm)		
Starting	Ending	Increment	Starting	Ending	Increment
598.424 (23.560 in)	654.304 (25.760 in)	2.540 (0.100 in)	598.424 (23.560 in)	659.384 (25.960 in)	2.540 (0.100 in)
x (mm)			y (mm)		
Starting	Ending	Increment	Starting	Ending	Increment
-25.400	27.940	2.540	-25.400	35.560	2.540

Table 8.8: Test Conditions for PDA Measurements at Different Locations

$y' = 143.581\ mm\ (5.6528\ in)$	$Q_\ell = 388\ ml/min$
$y = 0.000\ mm$	$Q_a = 26200\ ml/min$

$z'\ (mm)$	Range for $x'\ (mm)$
101.600 ($4.000\ in$)	593.344 – 659.384 ($23.360 - 25.96\ in$)
127.00 ($5.000\ in$)	593.344 – 654.304 ($23.360 - 25.760\ in$)
165.100 ($6.500\ in$)	603.504 – 649.224 ($23.760 - 25.560\ in$)
203.200 ($8.000\ in$)	608.584 – 641.604 ($23.960 - 25.260\ in$)
241.300 ($9.500\ in$)	613.664 – 633.984 ($24.160 - 24.960\ in$)

$z\ (mm)$	Range for $x\ (mm)$
176.9745	-30.480 – 35.560
151.5745	-25.400 – 30.480
113.4745	-20.320 – 25.400
75.3745	-15.240 – 17.780
37.2745	-10.160 – 10.160

Table 8.9: Test Conditions for PDA Measurements at Various Water and Air Flowrates

$x' = 623.824\ mm\ (24.560\ in)$ $x = 0.000\ mm$		$y' = 143.581\ mm\ (5.6528\ in)$ $y = 0.000\ mm$					
Q_ℓ	Q_a	$z'\ mm\ (in)$			$z\ mm\ (in)$		
(ml/min)	(ml/min)	Starting	Ending	Increment	Starting	Ending	Increment
207	22900	248.095 (9.7675)	103.315 (4.0675)	-7.620 (-0.300)	30.480	175.260	7.620
	26200	240.475 (9.4675)	103.315 (4.0675)	-7.620 (-0.300)	38.100	175.260	7.620
	29500	240.475 (9.4675)	103.315 (4.0675)	-7.620 (-0.300)	38.100	175.260	7.620
	32745	240.475 (9.4675)	103.315 (4.0675)	-7.620 (-0.300)	38.100	175.260	7.620
388	22900	232.855 (9.1675)	103.315 (4.0675)	-7.620 (-0.300)	45.720	175.260	7.620
	26200	245.555 (9.6675)	103.315 (4.0675)	-7.620 (-0.300)	33.020	175.260	10.160
	29500	225.235 (8.8675)	103.315 (4.0675)	-7.620 (-0.300)	53.340	175.260	7.620
	32745	225.235 (8.8675)	103.315 (4.0675)	-7.620 (-0.300)	53.340	175.260	7.620
580	26200	240.475 (9.4675)	103.315 (4.0675)	-7.620 (-0.300)	38.100	175.260	7.620
	29500	232.855 (9.1675)	103.315 (4.0675)	-7.620 (-0.300)	45.720	175.260	7.620
	32745	232.855 (9.1675)	103.315 (4.0675)	-7.620 (-0.300)	45.720	175.260	7.620
	35722	232.855 (9.1675)	103.315 (4.0675)	-7.620 (-0.300)	45.720	175.260	7.620

Chapter 9

Results and Discussion

In this chapter, two parts of experimental results are presented and discussed for an annular water jet with its inside surface exposed to an air stream. In the first part, the jet breakup characteristics are examined by taking photographs using Pentax-A 135 camera. The measurements from the photographs are compared with the predictions by the linear instability theory. In the second part, the resultant sprays from the disintegration of the water jets are investigated by using Dantec Particle Dynamics Analyzer (PDA). The size and velocity measurements for water drops are obtained and discussed.

9.1 Mechanism of Jet Breakup

An annular nozzle, Nozzle A, of 10 mm outside diameter is used for generating an annular water jet of 0.1187 mm in thickness with an air core inside of the jet. A set of photographs are taken for the water jet at four fixed water flow rates (1.262, 1.577, 1.893 and 2.524 $\times 10^{-5}$ m^3/s) and various inner air flow rates (see

the test conditions in Chapter 8). The measurements are made from the magnified images of the negatives using a slide projector. The original data obtained are presented in Tables F.1 to F.4 in Appendix F.

9.1.1 Flow Regimes

As discussed in Part I of this work, annular liquid jets always break up in the gaseous surrounding due to capillary force and aerodynamic interaction between liquid and gas. The gas stream inside of the liquid jet is found to play an important role in the jet breakup process. When this gas core is stationary, the annular liquid jet may converge to its centerline some distance from the nozzle exit if the liquid velocity is relatively small. Further downstream, the annular liquid jet becomes similar to cylindrical liquid jet and will break up into a train of liquid drops. However, if the gas core is moving, as the case discussed here, bubbles will be formed periodically. The photographs shown in Figures 9.1, 9.2 and 9.3 are some typical examples to indicate different phases of the jet breakup. Three flow regimes, named bubble formation, annular jet formation and atomization regime, are identified similar to others [43, 20].

Figure 9.1 indicate the periodic wave motion of the water jet. Under the same flow conditions with a relatively low air-to-water velocity ratio, the unstable interfacial wave at the water-air interface grows while it spreads downstream in the axial direction of the water flow. As the wave amplitude becomes sufficiently large, the water sheet contracts toward its central line and a water neck emerges (see the first wave valley in Frame A and B). The neck then collapses and an irregular spherical bubble is sealed off due to surface tension effect as shown in Frame C. After this, next period of the wave motion starts. As it is clear in Figures 9.1, successive nodules of encapsulated air are temporarily interconnected by a filament of water which breaks subsequently, setting free the individual bubble. This process is referred to as bubble

formation. This phase of jet breakup process is therefore defined as bubble formation regime.

As the air-to-water velocity ratio increases, it is observed from Figure 9.2 that an irregular annular jet is formed. The breakup point of the jet occurs closer to the nozzle exit. This phase of the jet breakup process is named as annular jet formation regime. The wavy jet surface and segmented thin liquid columns are typical for the flow in this regime.

For a further increase in the air-to-water velocity ratio, neither bubbles nor an annular jet is observed (see Frame G and H in Figure 9.3). The water-air interface inside of the nozzle becomes highly irregular and the wavy hollow-cone liquid sheet disintegrates into ligaments at the nozzle exit. Small drops of water, which are much smaller than the nozzle diameter, are formed. This regime is called atomization regime.

A schematic diagram, Figure 9.4, which indicates the three regimes described above, is constructed according to the water and air velocities corresponding to different flow regimes. However, Figure 9.4 is only a qualitative description of the flow regimes. The bubble formation regime refers to the flow pattern consisting of individual bubbles. Surface tension is thought to be responsible for the bubble formation in this regime. The aerodynamic interaction between liquid and gas may, however, be a dominant effect for droplet formation in the atomization regime. The annular jet formation regime, corresponding to the flow pattern with onset of wavy gas-liquid interfaces, is one type of flow in between the bubble formation and atomization regime.

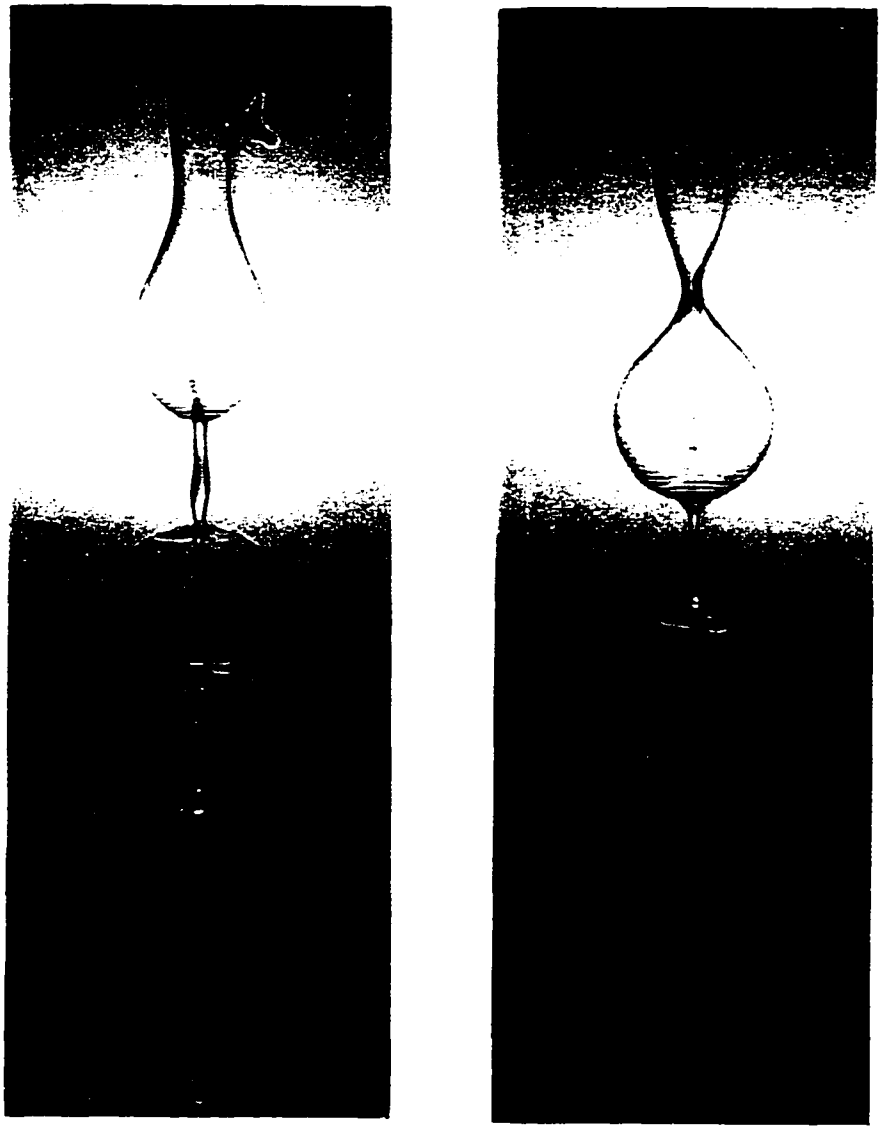

(A) (B)

Figure 9.1: Different phases of breakup for annular water jets-bubble formation. Nozzle dimensions: I.D.=9.525 mm, O.D.=10.000 mm; Water velocity: 2.165 m/s; Air velocity: 3.854 m/s.

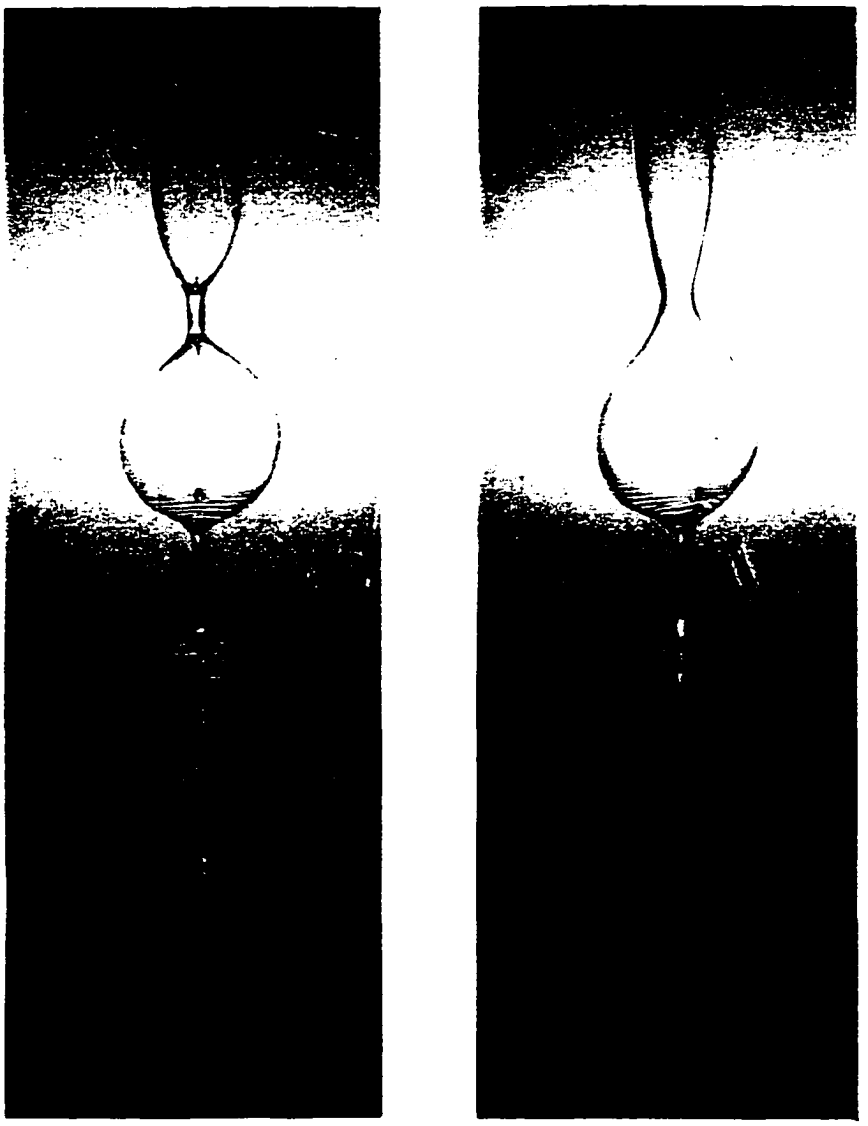

(C) (D)

Figure 9.1: Different phases of breakup for annular water jets-bubble formation. Nozzle dimensions: I.D.=9.525 mm, O.D.=10.000 mm; Water velocity: 2.165 m/s; Air velocity: 3.854 m/s.

(E) (F)

Figure 9.2: Different phases of breakup for annular water jets-annular jet formation. Nozzle dimensions: I.D.=9.525 mm, O.D.=10.000 mm; Water velocity: 2.165 m/s; Air velocity: 20.000 m/s.

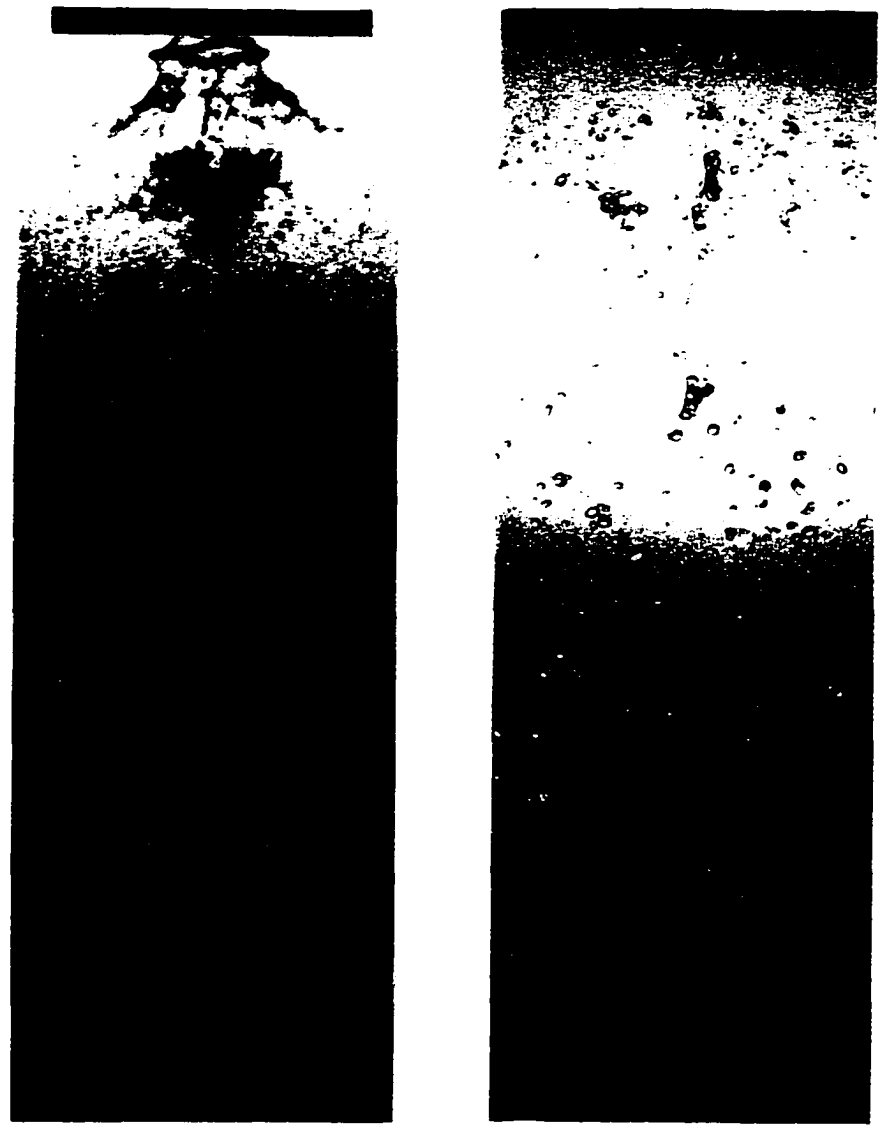

(G) (H)

Figure 9.3: Different phases of breakup for annular water jets-atomization. Nozzle dimensions: I.D.=9.525 mm, O.D.=10.000 mm; Water velocity: 2.165 m/s; Air velocity: 45.000 m/s.

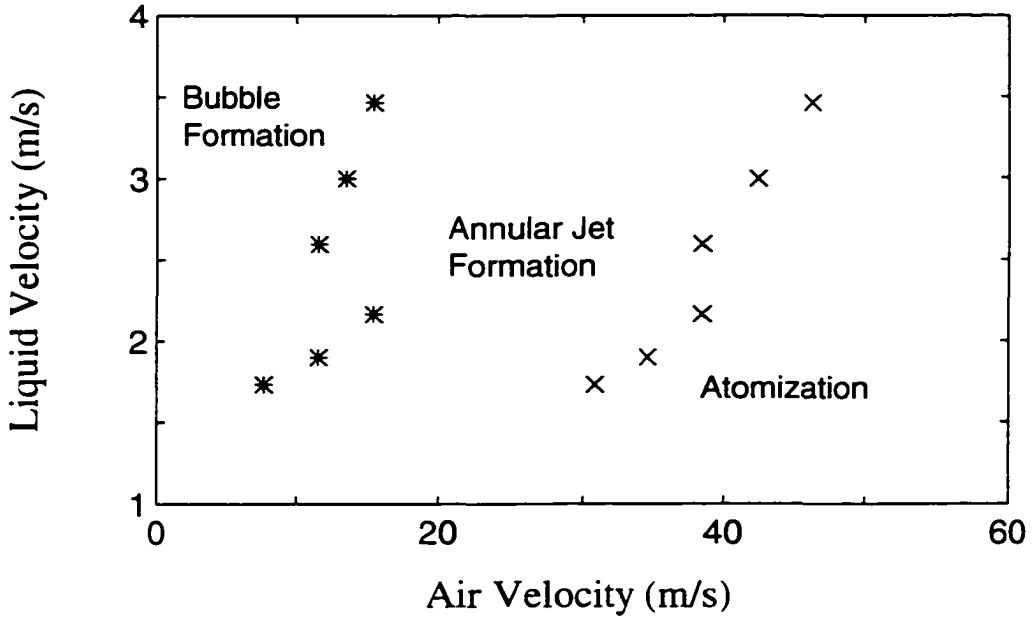

Figure 9.4: Schematics of three flow regimes for annular water jets

9.1.2 Jet Breakup Characteristics from Photography

An annular liquid jet in the bubble formation regime presents periodical wave motion at its gas-liquid interfaces, as mentioned in the above section. It is the interfacial wave growth that causes the pinchoff of bubbles and the jet breakup. To characterize the jet breakup process in this regime, bubble diameters, wave lengths and wave growth rates of unstable interfacial waves as well as jet breakup lengths are estimated from the photographic measurements, and also from the temporal instability analysis. The comparison between the experimental and theoretical results are presented below.

Tables 9.1 to 9.2 shown below are the jet breakup characteristics and their standard deviations due to multi-photo measurements in real dimensions. The bubble diameters D_b in Table 9.1 are obtained by taking the arithmetical average of the short $D_{i,S}$ and long axial length $D_{i,L}$ of all bubbles on all the photos taken at one flow condition and reducing by the corresponding magnification rate mr. The jet

breakup length L_B is the arithmetical average of those in Tables F.1 to F.4 at one flow condition and dividing by the corresponding magnification rate mr. The wave length L_w is the arithmetical average of $(z_3 - z_1)$ in Tables F.1 to F.4 for all photos taken at one flow condition and dividing by mr. To be compared with the temporal instability analysis, the wave growth rate Ω_i here is determined by $[U_\ell^*/(z_3 - z_1)\ \ln(\eta_3/\eta_1)]$ based on the interface deformation η_1 and η_3 at z_1 and z_3 locations in Table F.5. The notations of the variables discussed here are shown in Figure 9.5.

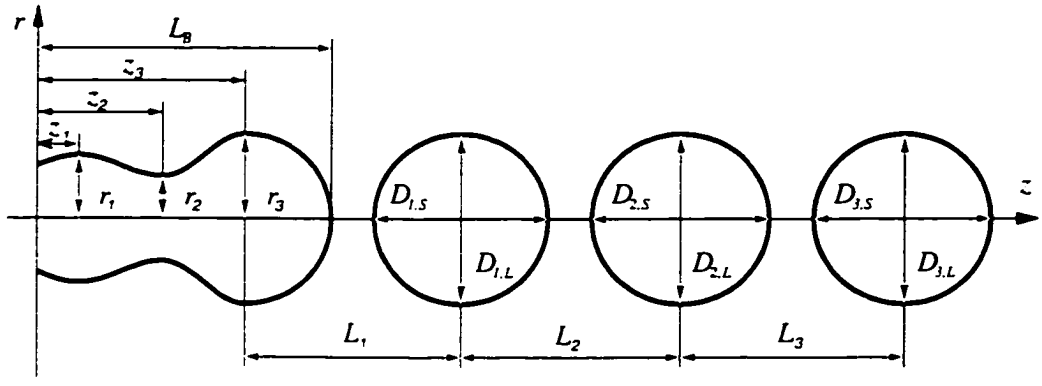

Figure 9.5: Schematic of bubbles formed after the jet breakup

The test conditions used are summarized in the tables in Chapter 8. Four water velocities (1.732, 2.165, 2.598 and 3.465 m/s) and various inner air velocities ranging from 3.854 to 15.412 m/s for each fixed water velocity are tested. It is found that the estimated bubble diameters D_b in Table 9.1 are nearly uniform for the water and air velocities considered. The variation between the largest and smallest diameter is 16%, in the same order as the standard deviation (15.79%) of the bubble diameter shown in Table 9.2. The mean diameter is 24.61 mm or 2.46 times the nozzle diameter ($O.D.$ = 10 mm and $I.D.$ = 9.525 mm), different from the prediction of 1.891 times of the nozzle diameter for cylindrical liquid jets by Rayleigh [8] but the observed value is almost the same as other measurements [43, 20].

The measured wave length L_w, jet breakup length L_B and wave growth rate Ω_i

Table 9.1: Jet Breakup Characteristics Estimated from Photographic Measurements

U_l^* (m/s)	U_a^* (m/s)	D_b (mm)	L_w (mm)	L_B (mm)	Ω_i $(1/s)$
1.732	3.854	27.117	47.459	77.622	0.7346
	7.708	25.997	40.175	74.543	0.8060
2.165	3.854	23.784	42.386	66.125	1.6388
	7.708	24.285	43.888	72.275	1.3993
	11.562	24.303	37.606	58.475	2.4596
2.598	3.854	23.738	54.779	63.381	1.9523
	7.708	24.548	39.505	51.424	3.5783
	11.562	24.475	35.270	58.621	2.2169
3.465	3.854	22.769	72.410	137.189	0.8319
	7.708	23.462	53.785	95.385	2.5629
	11.562	24.169	38.862	76.215	3.3677
	15.416	26.615	36.646	49.815	

are all dependent on specific water and air velocities. The wave length L_w decreases in general with the air-to-water velocity ratio, and so does the jet breakup length L_B. The relative errors for L_B, L_w and Ω_i are up to 23.75%, 8.1% and 46.8%, respectively. The large uncertainty for L_B measurement is because of the periodic wave motion of the water jet. To predict L_B more accurately, continuous photos are necessary for estimating the variation in L_B within one period. However, qualitatively, the predicted L_B increases with the liquid velocity and decreases with the air velocity as the others have observed [44, 65]. Large errors occur for the measurements of the wave amplitudes since they are two orders of magnitude smaller than the jet dimensions.

9.1.3 Predictions by Temporal Instability Analysis (T.I.A.)

To make comparison, the bubble diameters, unstable wave lengths, jet breakup lengths and unstable wave growth rates are calculated based on the temporal in-

Table 9.2: Standard Deviation of Multi-photo Measurements

U_ℓ^* (m/s)	U_a^* (m/s)	Sd_{D_b} (mm)	Sd_{L_w} (mm)	Sd_{L_B} (mm)	Sd_{Ω_*} $(1/s)$
1.732	3.854	4.281	1.674	4.440	0.2622
	7.708	2.851	3.252	7.630	0.3773
2.165	3.854	1.140	2.790	8.917	0.4428
	7.708	0.8671	2.017	9.168	0.3719
	11.562	2.289	2.112	7.015	0.9855
2.598	3.854	1.345	3.920	11.703	0.0000
	7.708	1.881	2.087	9.817	0.3294
	11.562	3.553	1.717	13.921	0.3737
3.465	3.854	1.853	4.295	4.512	0.3883
	7.708	2.438	1.664	1.088	0.062412
	11.562	1.455	1.654	7.627	1.0548
	15.416	4.213	1.339	7.253	

stability analysis under the conditions comparable with the experiment.

(a) Dimensionless Parameters Used for T.I.A.

The dimensional parameters presented in Table 9.3 are used to estimate the non-dimensional parameters, which are comparable with the experimental conditions. The

Table 9.3: Dimensional Parameters Corresponding to the Test Conditions

Nozzle Dimensions	$r_a^* = 9.525/2\ mm$ $r_b^* = 10.00/2\ mm$
Reference Length Scale	$r_h = (r_b^* - r_a^*)/2 = 0.1187\ mm$
Reference Velocity Scale	$U_\ell^* = 1.7323, 2.1653, 2.5984, 3.4645\ m/s$
Water density	$\rho_\ell = 1000\ kg/m^3$
Air density	$\rho_g = 1.29\ kg/m^3$
Water viscosity	$\mu_\ell = 0.001\ N\ m/s$
Surface tension	$\sigma = 0.074\ N/m$

non-dimensional parameters estimated are shown in Table 9.4.

Table 9.4: Dimensionless Parameters for T.I.A. Calculations

Radii for Annular Cross Section	$r_a = r_a^*/r_h = 40.12$ $r_b = r_b^*/r_h = 42.12$
Density Ratio	$\rho = \rho_g/\rho_\ell = 1.29 \times 10^{-3}$
Water Velocity	$U_\ell = U_\ell^*/U_\ell^* = 1$

U_ℓ^* (m/s)	U_a^* (m/s)	$U_a = U_a^*/U_\ell^*$	$Re = \rho_\ell U_\ell^* r_h/\mu_\ell$	$We = \rho_\ell U_\ell^{*2} r_h/\sigma$
1.732	3.854	2.225	205.62	4.81
	7.708	4.450		
2.165	3.854	1.780	257.02	7.52
	7.708	3.560		
	11.562	5.339		
2.598	3.854	1.483	308.43	10.83
	7.708	2.966		
	11.562	4.449		
3.464	3.854	1.112	411.24	19.25
	7.708	2.225		
	11.562	3.337		
	15.416	4.450		

(b) Predictions by Temporal Instability Analysis (T.I.A.)

By the linear instability theory, a dominant unstable wave mode, which has maximum wave growth rate, outgrows the other modes, and is the one to be observed in reality. Therefore, to compare with the experimental results, the dominant wave number $\alpha_{r,max}$ are used to estimate the wave length L_w and bubble diameter D_b by considering the conservation of the entrapped gas. The maximum wave growth rate $\Omega_{i,max}$ is utilized to calculate the jet breakup length L_B based on the assumption that the pinchoff of bubbles occurs when the amplitude of the dominant unstable wave becomes equal to the mean jet radius. Table 9.6 gives the equations for the calculations of various jet breakup characteristics from T.I.A., where ϵ_0 in the formula for L_B is the amplitude of initial disturbances, which depends on the noise level in

the physical system under investigation, and one typical values used is 64.74 μm in this experimental setup. This value of ϵ_0 is obtained by forcing L_B from the photo measurements to satisfy the relation to estimate the jet breakup length by the linear instability theory.

Table 9.5: Jet Breakup Characteristics Estimated from T.I.A.

U_l^* (GPM)	U_a^* (SCFM)	D_b (mm)	L_w (mm)	L_B (mm)	$\Omega_{i,max}$ $(1/s)$
1.732	3.854	19.954	58.328	66.632	154.34
	7.708	16.835	35.062	36.421	291.32
2.165	3.854	20.068	59.547	82.302	146.75
	7.708	17.038	36.343	46.523	274.79
	11.562	13.753	19.117	25.817	464.42
2.598	3.854	20.260	61.108	98.032	141.46
	7.708	17.251	37.721	57.904	258.86
	11.562	14.224	21.149	32.032	443.53
3.464	3.854	20.178	60.366	126.126	137.35
	7.708	17.630	40.266	82.312	230.54
	11.562	14.614	22.937	47.135	404.07
	15.416	10.837	9.352	27.347	653.22

Table 9.6: Comparison of Photo Measurements with Temporal Instability Analysis

Jet Breakup Characteristics	Temporal Instability Analysis	Photographic Measurements
Bubble Diameter	$(12\pi/\alpha_{max})^{1/3}(r_a^*)^{2/3}$	D (measured directly)
Breakup Length	$(U_l^*/\Omega_{i,max})$ $\times \ln[(r_a^* + r_b^*)/(2\epsilon_0)]$	L_B (measured directly)
Wave Length	$2\pi/\alpha_{r,max}$	L_w (measured directly)
Wave Growth Rate	$\Omega_{i,max}$	$U_l^*/(z_3 - z_1)\ln(\eta_3/\eta_1)$

9.1.4 Comparison of Measurements with T.I.A. Results

The bubble diameter D_b, unstable wave length L_w and jet breakup length L_B estimated from the photographic measurements and the temporal instability analysis are presented in Figures 9.6 to 9.8 with the air-to-water velocity ratio U_a as the abscissa. The solid lines represent the predicted values by the temporal instability analysis while the dash lines stand for those from photographic measurements for four water velocities of 1.732, 2.165, 2.598 and 3.465 m/s, respectively. The standard deviations for each measured data are also indicated in the figures.

Figure 9.6 shows the measured and predicted bubble diameter D_b for different air-to-water velocity ratios U_a. The bubble diameters measured from the photographs are almost uniform for all the water and air flowrates considered, as discussed in the above section. The average bubble diameter is 24.61 mm, which is 2.46 times of the nozzle diameter. The observation that the bubble size is independent of the flow conditions is consistent with that for cylindrical liquid jets by Rayleigh [8]and for annular liquid jets by others [43, 20]. However, the predicted bubble diameter is dependent on the flow conditions, and decreases with the air-to-water velocity ratio. Better agreement of the measurements with the predictions occurs only for low air-to-water velocity ratios. For example, at U_a = 1.112, 1.48 and 1.78, the linear instability theory under-estimates the bubble diameter by up to 15.8%. For larger velocity ratios, the theory does not predict the bubble diameter well. The reason for this might be that the air pressure inside of the annular sheet increases with the air velocity. In the experiment, this pressure increase due to the increase of the air velocity results in larger bubble diameters. However, since this pressure increase is not taken into account in the predictions by the linear instability theory, the predicted bubble diameters are smaller than the experimental ones when the air velocity is high.

The jet breakup lengths L_B observed from the experiment and estimated by the

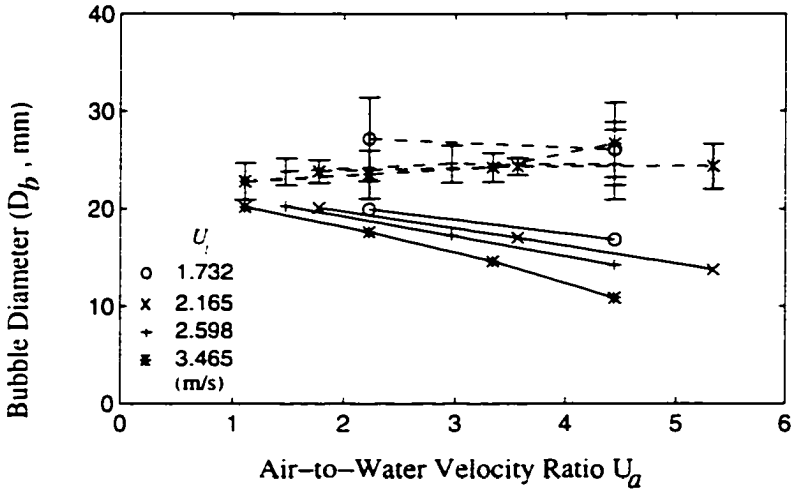

Figure 9.6: Bubble diameter versus air-to-water velocity ratio. Nozzle mean diameter: 9.7625 *mm*. Dash line: experiment; Solid line: linear theory.

linear instability theory are shown in Figure 9.7. It is seen that the measurements are consistent with the predictions. Both the measured and predicted L_B decreases with the air-to-water velocity ratio, indicating that the presence of gas stream promotes the jet instability. Increase in the air velocity may cause the jet to break up closer to the nozzle exit. The large discrepancy of 56% between the measurements and predictions exists at the largest air-to-water velocity ratio of 5.339 considered in this work. The reason for this might be that from one side, the measured L_B has larger uncertainty due to its periodic variation within one wave length. From the other side, the way to predict the wave length by the linear instability theory may require certain modification at larger air-to-water velocity ratios, such as non-linear effect or gas compressibility effect.

Shown in Figure 9.8 is the comparison between predicted and experimental wave lengths L_w. It is seen that both experimental and theoretical wave lengths decrease with the air velocity. This implies that utilization of high velocity air in atomization may reduce the size of liquid droplets, and therefore can improve the atomization per-

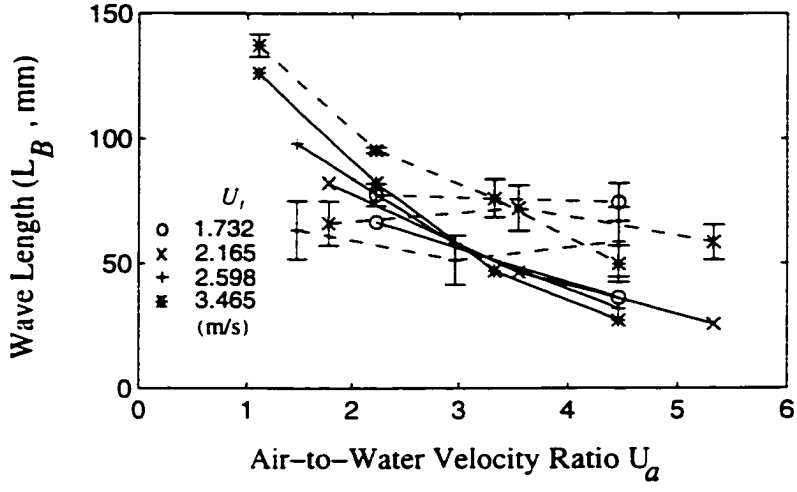

Figure 9.7: Jet breakup length versus air-to-water velocity ratio. Nozzle mean diameter: 9.7625 *mm*. Dash line: experiment; Solid line: linear theory.

formance. The discrepancy between the measurements and the estimations become greater as the air velocity increases, or when the flow approaches the intermittent regime. The onset of flow turbulence (Reynolds number of the air flow is about 10000) and the thinning of liquid sheets are a potential cause for this discrepancy.

The wave growth rates predicted by the linear instability theory (Table 9.1) are two orders of magnitude different from those estimated from the photographs, although the general trend of variation that the increase of the air velocity enhances the jet instability agrees with each other. The reason for this large discrepancy is the larger uncertainty of the growth rate measurements from the photos since compared with the jet dimensions the wave growth rates is more than one order smaller. In addition, the way to predict the wave growth rate by the linear instability theory need be improved.

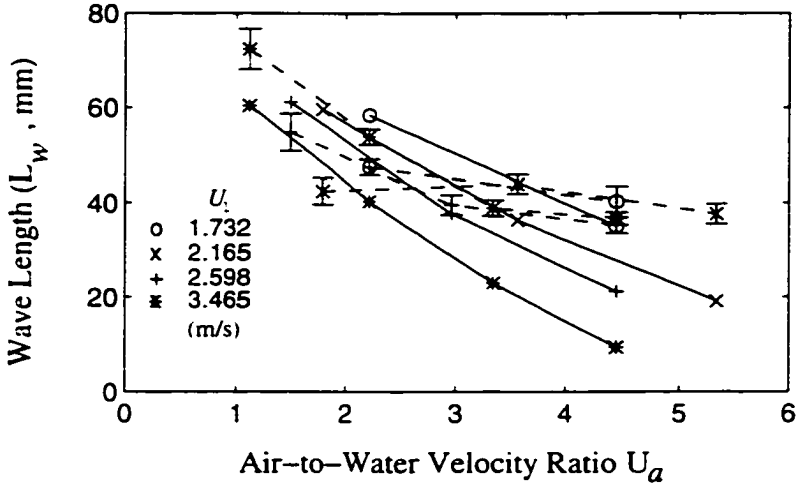

Figure 9.8: Unstable wave length versus air-to-water velocity ratio. Nozzle mean diameter: 9.7625 mm. Dash line: experiment; Solid line: linear theory.

9.2 Spray Characteristics

The test apparatus described in Chapter 8 produces sprays of fine droplets with Nozzle B ($O.D. = 2.54mm$ and $I.D. = 2.375mm$ for the annular liquid sheet; core pipe $I.D. = 1.588mm$ for air). The sprays generated at the four water flowrates (207, 388, 580 and $780ml/min$) and various air flowrates ranging from 22, 900 to 35, 722 ml/min are measured by using Dantec Particle Dynamics Analyzer (PDA). To examine the spray symmetry, measurements are made along the spray radial direction ox and orthogonal direction oy on the spray cross section at $z = 151.57$ mm. The size and axial velocity distributions are obtained at up to 25 different locations along the radial direction ox at five different cross sections located at $z = 37.27, 75.37, 113.47, 151.57$ and 176.97 mm. To examine the effects of the water and air velocities, the spray characteristics are measured at up to 20 locations along the spray axis oz for each pair of water and air flowrates mentioned above.

At each location within the spray measured, the Dantec PDA and the accompany-

ing SIZEware software provide detailed data and graph options such as various mean droplet sizes and velocities as well as their histograms. For example, the histograms shown in Figure 9.9 for the droplet diameter and velocity provide the detailed information about counts of droplets per size class for the diameter histogram and per velocity class for the velocity histogram. However, in this work, only the data, which are representative of spray characteristics often considered in spray application, are presented. The original measurements are listed in Tables F.6, F.7 and F.8 in Appendix F in details. The general observation of spray characteristics are described below.

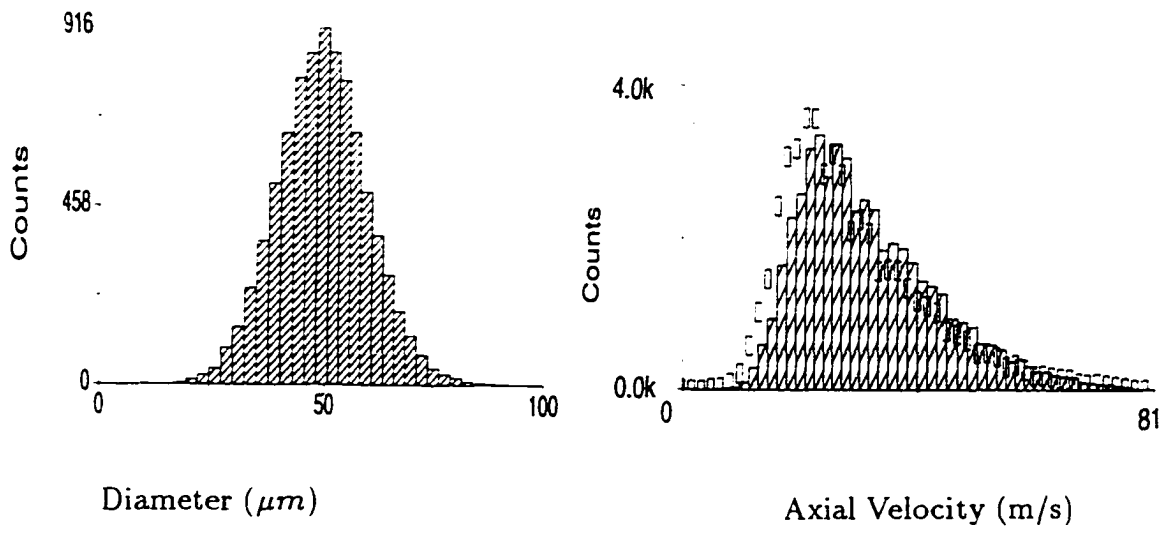

Figure 9.9: Examples of drop velocity and size histograms

9.2.1 Symmetry of the Spray Structure

(a) Symmetry of Mean Axial Velocity Distribution

Figure 9.10 shows the arithmetic mean axial velocity measured along two orthogonal radial directions at the axial plane of 151.57 *mm* from the nozzle exit in the spray field. It is seen that the mean axial velocities along both directions have a typical Gaussian-type variation, as observed for the spray formed from the plane liquid sheet breakup [44] and from the annular liquid sheet breakup [71]. The mean velocity reaches the maximum value at the spray centerline, and decreases from the spray center to the edges as the spray spreads out. The air entrainment from the surrounding to the spray edges should be responsible for this decrease of the mean velocity at the spray edges. The velocity profile is nearly symmetric about the spray axis parallel to the nozzle axis, which is off the nozzle axis by about 2.54 *mm* along the *ox* direction, and 5 *mm* along *oy* axis. The reason for this discrepancy might be the annular section for water being eccentric with the core pipe for air since the dimensions of the annular nozzle are quite small, especially the annular gap being only 0.08*mm*. The error may also occur because the nozzle positions were not exactly the same before and after it was rotated by 90° during the tests, although much attention was paid to it.

(b) Symmetry of Sauter Mean Diameter Distribution

The Sauter Mean Diameters (SMD) shown in Figure 9.11 are nearly symmetric about the spray axis, and are off the nozzle axis as the velocity profiles are. The measurements along two orthogonal directions differ from each other, showing certain degree of non-symmetry of the spray. The SMD increases from the spray central region to the edges. The larger droplet sizes near the spray edge is probably due to the collision and coalescence of drops. However, in a small region close to the

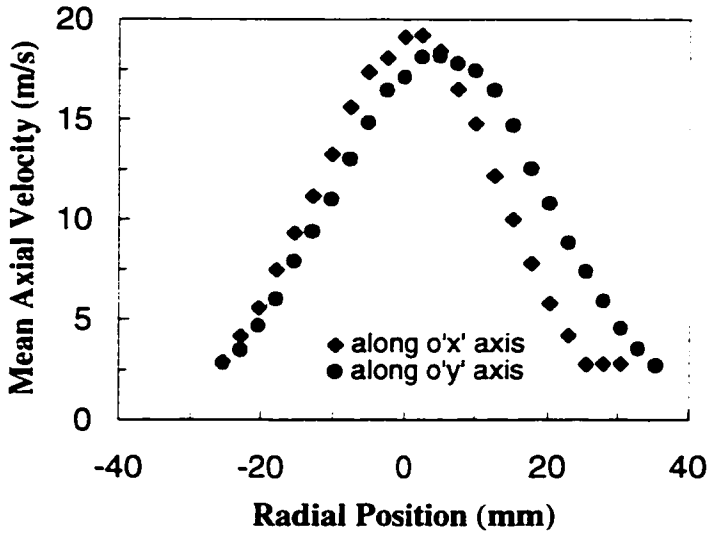

Figure 9.10: Drop mean axial velocities along two orthogonal radial directions. Water velocity: $U_\ell^* = 10.15\ m/s$, air velocity $U_a^* = 220.61\ m/s$, axial location $z = 151.57\ mm$.

center, certain increase in the droplet size is noticed as reported for annular liquids in co-flowing air streams by Lavergne [71]. This differs from what was observed for a cylindrical liquid jet surrounded by an air stream [66] and for "sandwich" type of plane liquid sheets [44], in which the smallest droplets are always present in the center of the spray. The reason for this difference is the presence of air cores. If there is no air stream inside of a liquid jet, there will be no any relative increase of droplet sizes in the central region of sprays. However if there is an air core, some relatively large droplets will be observed in the central region. This is to be identified by combining the variations of the drop size and the number density later.

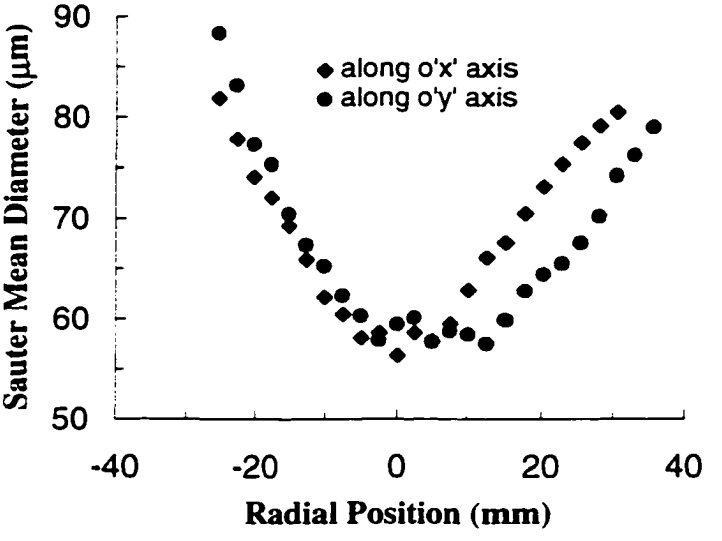

Figure 9.11: Drop Sauter Mean Diameter along two orthogonal radial directions. Water velocity $U_l^* = 10.15\ m/s$, air velocity $U_a^* = 220.61\ m/s$, axial location $z = 151.57\ mm$.

9.2.2 Spatial Distribution of the Drop Velocity and Size

The spatial variations of the spray characteristics are presented in Figures 9.12 to 9.17. In each figure, one of the typical spray characteristics (mean axial velocity, turbulent intensity, Sauter Mean Diameter, and number density) is presented for various radial positions along ox axis at five axial planes under fixed flow conditions. It is seen from the figures that all the spray characteristics are essentially symmetric about the spray axis.

(a) Spatial Distribution of Mean Axial Velocity

The spatial distribution of mean axial velocity is shown in Figure 9.12 in the radial direction. In the center of the spray, the velocity reaches maximum and then decreases from the center to the spray boundary. Along the spray axis downstream, the velocity profile indicates the expansion of the spray region. The variation of the

velocity near the central region is opposite to that near the edge. Near the center the axial mean velocity decreases as the distance from the nozzle increases, while close to the edge it increases along the axis downstream. In another words, the droplets closer to the nozzle exit have higher velocities than those farther downstream in the central region. Whereas near the spray boundary, the droplets closer to the nozzle exit have lower velocities than those farther downstream. This is a typical plane-sheet type of velocity variation [44]. At the nozzle exit, the initial larger velocity difference (e.g. $211m/s$) between the liquid jet and the air core results in high velocities of the droplets due to strong momentum transfer. As the droplets transport downstream and spread out, they are decelerated in general because of the air entrainment from the surrounding. By taking account of droplet sizes, the smaller drops in the central region decelerate faster and move down while near the spray edge, the larger drops decelerate slower and move outwards when they move down. As a result, the velocities of the droplets decrease quickly in the central region, but increase slightly near the boundary. In general, the velocity profile flattens to a small value downstream along the spray axis.

Figure 9.13 shows self-similarity of the drop axial velocity profile. When the drop axial velocity U_z normalized by the drop maximum velocity U_{max} on each corresponding spray plane is plotted with the radial coordinate x normalized by the axial coordinate z, the normalized velocity profiles collapse together reasonably well on the velocity correlation for a turbulent cylindrical jet [3]. The velocity profile does not become self-similar until the distance from the nozzle exit z is about 30.67 times the nozzle diameter D. This implies that the liquid drops follow primarily the air motion in the central region, and have a jet-type of velocity distribution along the spray radial direction.

The turbulent component (RMS) of drop axial velocity takes longer to develop

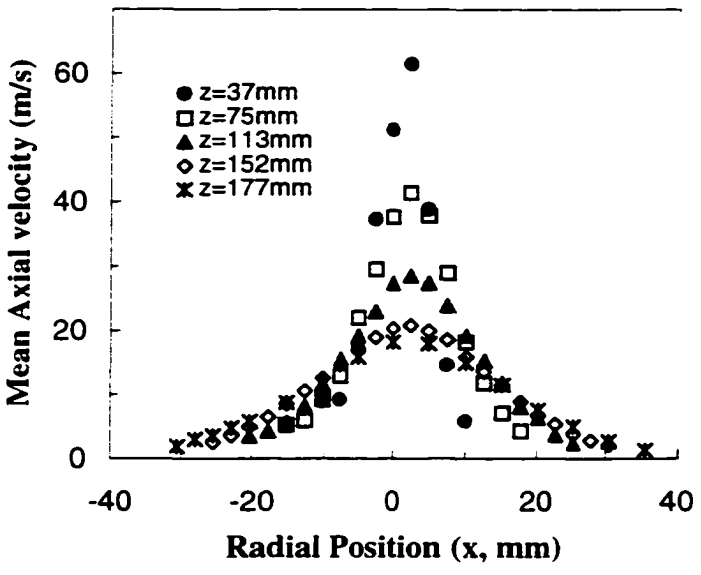

Figure 9.12: Spatial distribution of drop mean axial velocity. Water velocity $U_l^* = 10.15\ m/s$, air velocity $U_a^* = 220.61\ m/s$.

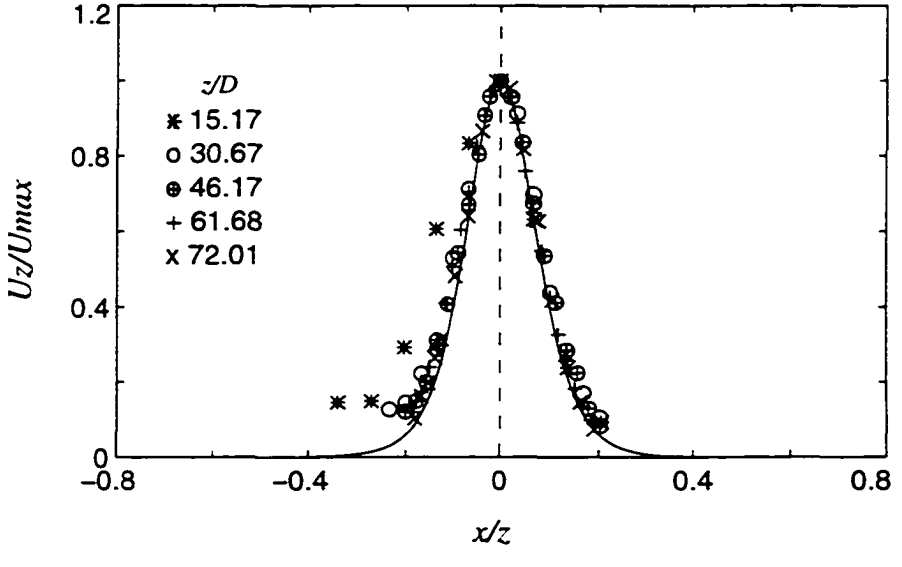

Figure 9.13: Self-similarity of drop mean axial velocity. Water velocity $U_l^* = 10.15\ m/s$, air velocity $U_a^* = 220.61\ m/s$. Solid line: correlation for cylindrical jet flow; Symbols: PDA measurements.

than the mean velocity. As shown in Figure 9.14, it is non-similar at $z/D = 30.67$, and does not become similar until $z/D = 46.17$. Note that non-similar variation of the turbulent component occurs in the spray central region.

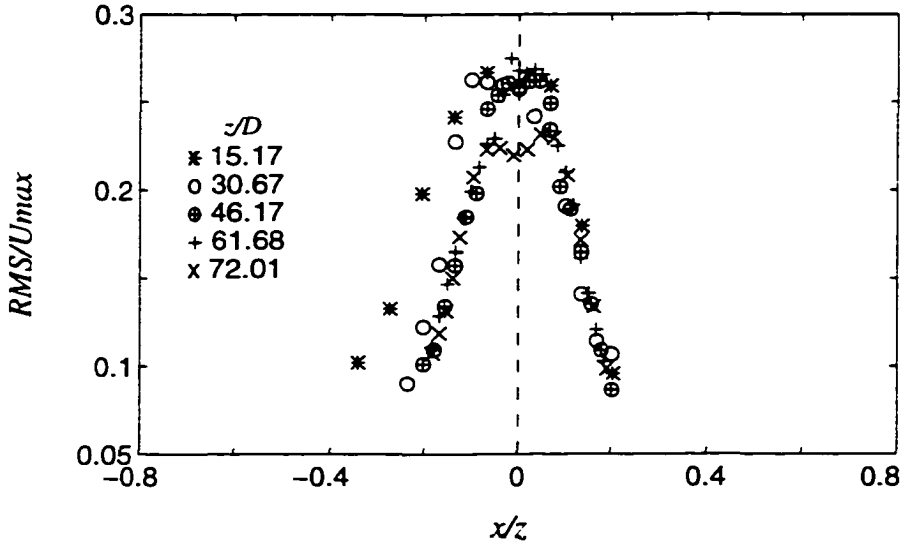

Figure 9.14: Self-similarity for the turbulent component of drop axial velocity. Water velocity $U_\ell^* = 10.15\ m/s$, air velocity $U_a^* = 220.61\ m/s$.

The turbulent intensity in Figure 9.15 shows the lowest value in the center and increases from the center to the spray edge at every spray cross section, although the RMS of the mean axial velocity has similar variation with the mean velocity (see Table F.7). The turbulent intensity at every radial position decreases as the measurement plane moves far from the nozzle exit. This variation is mainly because of aerodynamic interaction between the atomizing air and the dispersed phase. In the central region, the dispersed phase follows, to a certain degree, the air motion so that the dispersed phase flow is relatively stable compared with the outer region. The strong turbulent fluctuation near the spray edge is probably due to the air circulation around the spray.

(b) Spatial Distribution of Sauter Mean Diameter

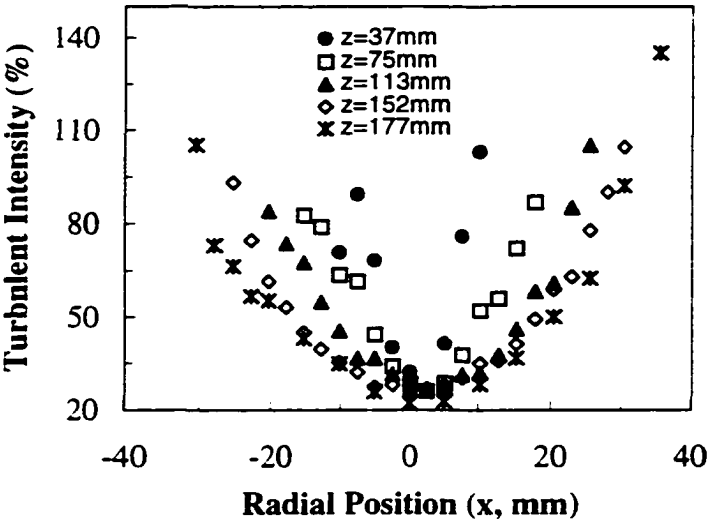

Figure 9.15: Spatial distribution of turbulent intensity. Water velocity $U_\ell^* = 10.15\ m/s$, air velocity $U_a^* = 220.61\ m/s$.

Figure 9.16 shows the Sauter Mean Diameter (SMD) versus the radial position corresponding to the measurements at five axial spray planes. Coupled with the variation of the axial mean velocity (see Figure 9.12), it is seen that the variation of drop sizes and the drop velocities are consistent with each other in the sense that smaller drops have higher velocities (as in the central region of the spray) and larger drops have smaller velocities (as in the outer region of the spray). The high mean RMS velocities caused by the high-velocity air motion in the spray central region results in small droplets there because high shear and aerodynamic interaction between the liquid and gas phase is known to be beneficial for the production of small droplets, as predicted by the linear instability theory presented earlier.

It is seen that some increase in the drop size (the SMD) with the axial distance exists in the central region, similar to that observed by Lavergne [71]. To explain this, it is better to take account of the number density variation versus the radial

position at five axial spray planes shown in Figure 9.17. The variation of the number density is found to be very similar to that for the droplet size. This means that at each axial spray plane, there are always less small drops in the central region than near the boundary. The reason for this is that there is an air core inside of the annular liquid sheet. The presence of the air core results in dilute spray in the central region. Meanwhile, the air core dominates the drop motion so that the small drops in the center transport to the boundary due to high RMS velocities near the spray centerline. As a result, the increase of the SMD may occur in the spray central region occasionally, and the number density decreases in the center.

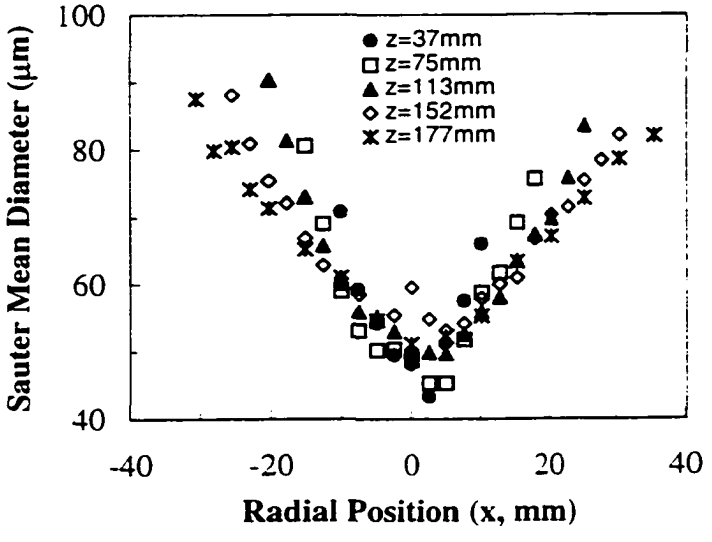

Figure 9.16: Spatial distribution of drop Sauter Mean Diameter. Water velocity $U_l^* = 10.15\ m/s$, air velocity $U_a^* = 220.61\ m/s$.

Near the spray edge, there exist more larger drops closer to the nozzle exit than farther downstream at a fixed radial position. This can be explained by the spray expansion in the downstream direction. Since the trajectory of drops is outward and downward at the same time, the drop size on the lower plane is smaller than on the

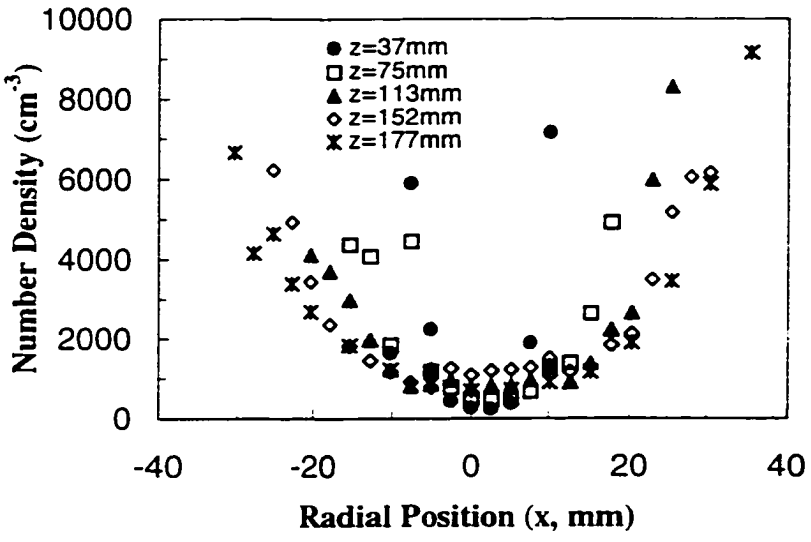

Figure 9.17: Spatial distribution of number density. Water velocity $U_\ell^* = 10.15\ m/s$, air velocity $U_a^* = 220.61\ m/s$.

upper plane, so is the number of drops.

9.2.3 Effects of the Liquid and Gas Velocities

To further investigate the characteristics of the hollow-cone sprays formed from the annular liquid sheets breakup, the mean axial velocity, the turbulent intensity, Sauter Mean Diameter and number density are also presented in Figures 9.18 to 9.25 for different axial locations and various water and air velocities. In each figure, the variation of the spray characteristics along the spray axis is shown for a pair of water and air velocity (U_ℓ, U_a).

(a) Effects on Mean Axial Velocity

The mean axial velocity shown in Figure 9.18 all decreases downstream along the spray axis although the velocity gradient in z direction depends on the water and

air velocities. This decrease in the axial velocity results mainly from the boundary growth and the entrainment of the ambient air. Rapid mixing of the spray droplets with the ambient air and the resulting momentum exchange lead to the deceleration of drops in the spray center. At a fixed axial position, the mean velocity increases generally with the air velocity for a fixed water velocity. For example, at the water velocity of $U_\ell = 5.41\ m/s$, the mean velocity curve in Figure 9.18 moves up as the air velocity increases from 192.83 to 276.72 m/s. Clearly, when the air velocity is higher, the momentum transferred from the air to the dispersed phase or droplets is larger. Therefore, the drop velocity is higher. However, the axial velocity does not increase linearly with the increase of the air velocity. There is an uplimit for the drop axial velocity at each fixed water velocity. When the air velocity is of certain high value, no further increase in the drop velocity is obtained. Besides, the effect of the air velocity on the drop velocity becomes small when the water velocity is high. This is because the momentum transfer depends on not only air but also water flow, and the momentum for water is fixed when the nozzle cross section area and water flow rate are fixed.

On the other hand, the similar variation exists for the drop axial mean velocity with the water velocity at a fixed air velocity. That is for a fixed air velocity (e.g., $U_a = 220.60\ m/s$), the increase in the water velocity (e.g., $U_\ell = 5.41, 10.15$ and $15.17\ m/s$) causes the drop velocity to increase significantly for low values of the water velocity and gradually approaches an up limit when the water velocity is high. The effect of the water velocity becomes small when the air velocity is high. It is also noticed from Figure 9.18 that at some axial locations close to the nozzle exit, the drop velocity decreases with the air or water velocity. The reason for this might be that there are relatively strong flow fluctuation close to the nozzle exit. The turbulent intensities listed in Table F.8in Appendix F vary from 35 to 20% for the axial location

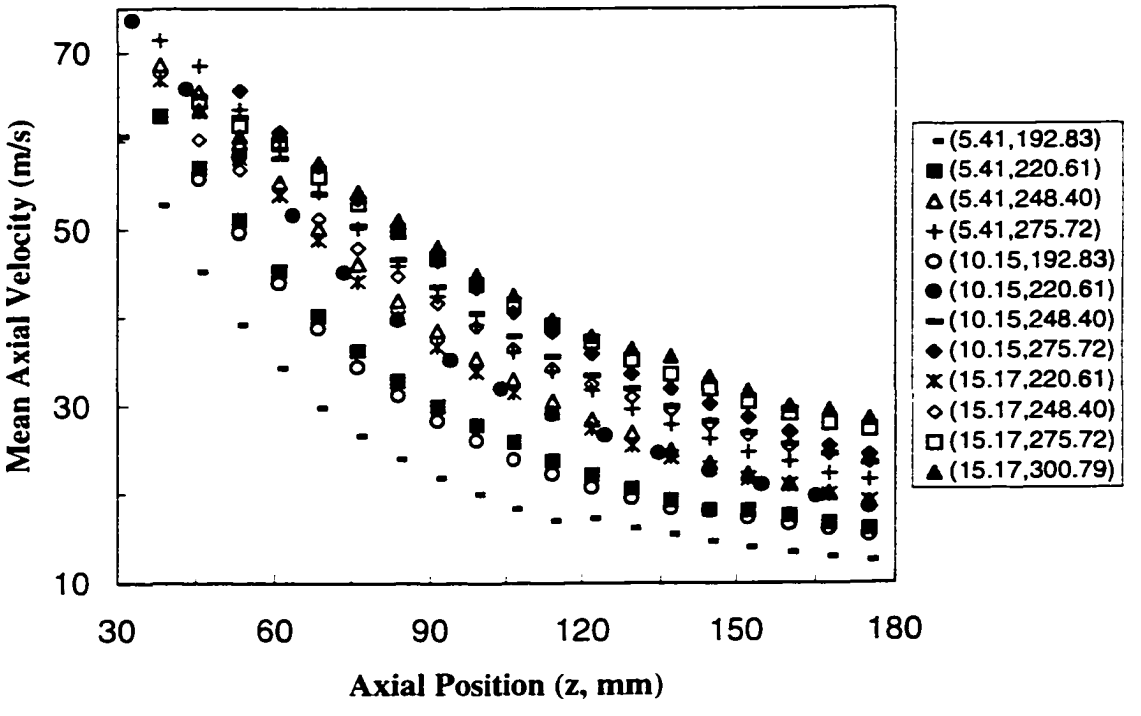

Figure 9.18: Effects of water and air velocities on drop mean axial velocity along the spray axis.

from the nozzle exit to downstream at all water and air velocities considered. The higher values of turbulent intensity occur near the nozzle exit.

According to the conservation of momentum, the momentum of a spray J must remain constant at each cross section of the spray. That is:

$$J = \int \varphi_a \rho_a u^2 dA + \int \varphi_\ell \rho_\ell u^2 dA \tag{9.1}$$

$$\frac{J}{\rho_a} = \int \left[1 + \varphi_\ell \left(\frac{\rho_\ell}{\rho_a} - 1\right)\right] u^2 dA \tag{9.2}$$

Based on self-similarity of the drop axial velocity profiles discussed earlier, we can assume:

$$\frac{u(r,z)}{u_{max}(z)} = f\left(\frac{r}{z}\right) \tag{9.3}$$

where $u(r,z)$, the axial velocity for both liquid and gas; $u_{max}(z)$ maximum velocity at each spray cross section; r and z, radial and axial coordinate respectively.

Substituting Eq. (9.3) into Eq. (9.2) and re-arranging the equation, it gives:

$$\frac{u_{max}(z)}{(J/\rho_a)^{1/2}} = \frac{1/z}{\left\{\int_0^b \left[1 + \varphi_\ell \left(\frac{\rho_\ell}{\rho_a} - 1\right)\right] f^2(\frac{r}{z})\, 2\pi \left(\frac{r}{z}\right) d(\frac{r}{z})\right\}^{1/2}} \tag{9.4}$$

where b, the radius of spray at each cross section; φ_ℓ, liquid volume fraction. When $\varphi_\ell = 0$ in Eq. (9.4), the inverse of the denominator at the right hand side of Eq. (9.4) becomes a constant of 7.4 approximately which is for cylindrical gas jet flow [3]. For the spray studied in this work, φ_ℓ has a value between zero and one, and the integral in Eq. (9.4) will depend on the profile of φ_ℓ. The drop axial velocities in the spray center for various water and air velocities shown in Figure 9.18 (except for those measurements very close to the nozzle exit) are correlated according to Eq. (9.4) by assuming the profile for φ_ℓ is self-preserving, so that

$$\frac{u_{max}(z)}{(J/\rho_a)^{1/2}} = \frac{c}{z} \tag{9.5}$$

The correlation coefficient and deviations from the experimental data are presented in Table 9.7 for different flow conditions of water and air velocity. It is seen that the correlation coefficients c vary with the water and air velocity slightly, and are in the same order as the value for a cylindrical gas jet. This indicates that the motion of liquid droplets in the spray is dominated by the air motion in the central region. The velocity profile for the droplets is self-similar when the distance is far enough from the nozzle exit. The correlation curves shown in Figures 9.19, 9.20 and 9.21 indicates a very good agreement with the experimental data.

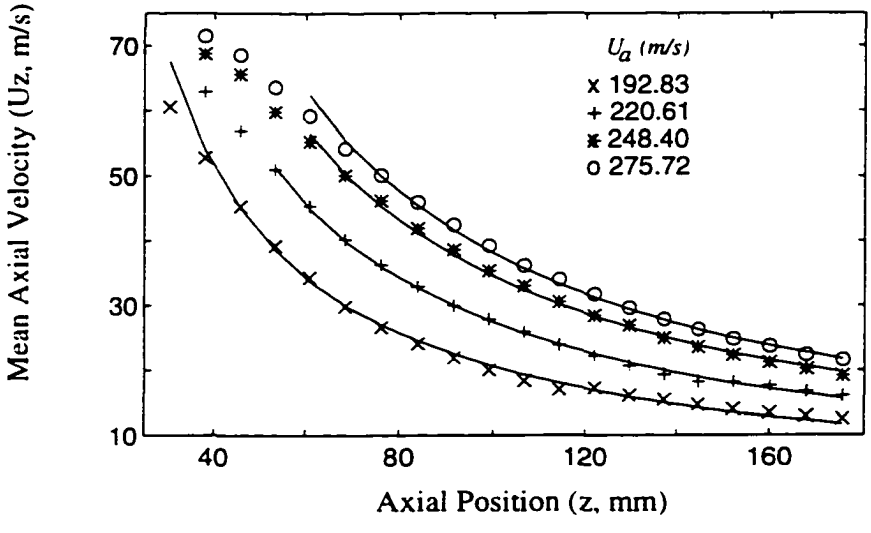

Figure 9.19: Correlation for drop mean axial velocity. $U_\ell^* = 5.41 m/s$; Solid line: correlation Eq. (9.5); Symbol: measurement.

(b) Effects on Sauter Mean Diameter

Figure 9.22 indicates the Sauter Mean Diameters for spray droplets at different axial locations for three fixed water velocities ($U_\ell = 5.41, 10.15$ and $15.17\ m/s$) and four air velocities ($U_a = 192.83, 220.61, 248.04, 275.72$ and $300.79\ m/s$). The effects

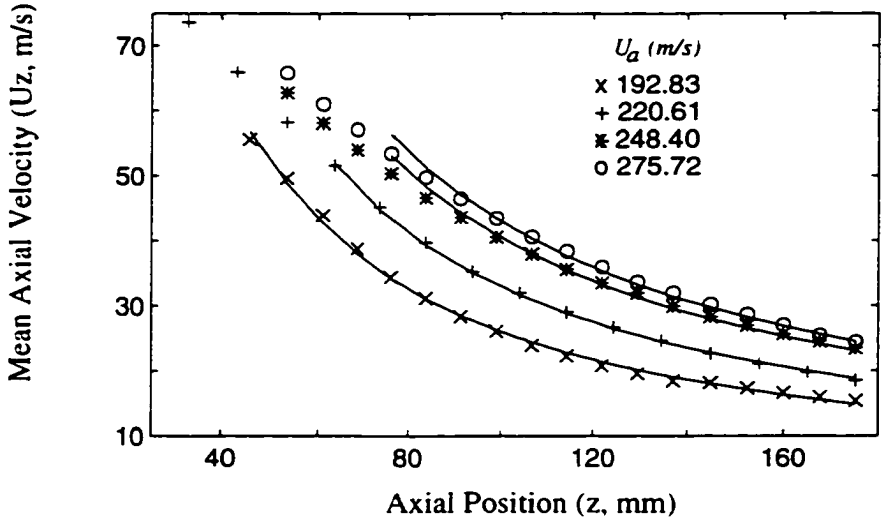

Figure 9.20: Correlation for drop mean axial velocity. $U_\ell^* = 10.15 m/s$; Solid line: correlation Eq. (9.5); Symbol: measurement.

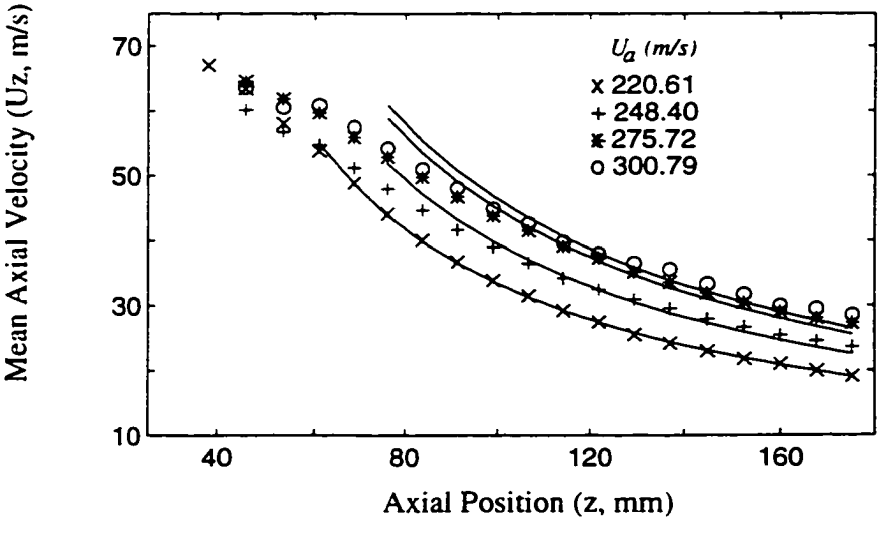

Figure 9.21: Correlation for drop mean axial velocity. $U_\ell^* = 15.17 m/s$; Solid line: correlation Eq. (9.5); Symbol: measurement.

Table 9.7: Correlation Coefficient and Uncertainty for Drop Axial Mean Velocity

Water velocity U_l^* (m/s)	Air velocity U_a^* (m/s)	Coefficient c	Deviation (%)
5.41	192.83	6.943	7.25
	220.61	8.240	1.98
	248.40	9.340	2.60
	275.72	9.380	2.75
10.15	192.83	7.385	3.28
	220.61	8.594	1.32
	248.40	9.740	2.67
	275.72	9.590	2.66
15.17	220.61	7.293	1.03
	248.40	8.140	4.57
	275.72	8.735	5.74
	300.79	8.583	6.86

of the water and air velocity on the SMD are not as obvious as on the mean axial velocity. However, the data points shown in Figure 9.22 can be classified into three groups. One group of lowest SMD values are obtained for the water velocity of 5.41 m/s. Another group of data point in the up part of the figure are for the water velocity equal to 15.17 m/s. The group between them is the one for the water velocity of 10.15 m/s. Obviously, the SMD has a global increase with the increase in the water velocity among three groups, and in each group, the air velocity shows a small effect on the SMD. However, the SMD is reduced in general by increasing the air-to-water velocity ratio. For all the water and air velocities (air-to-water velocity ratio $U_a^* = 14.57$ to 50.96) and at all the axial locations ($z = 30.48$ to 175.26 mm) considered here, the SMD, ranging from 27 to 45 μm, indicates that using atomizing air produces fine size of droplets for the spray and improve atomization performance significantly. The reason for this reduction effect of the atomizing air on the drop size is that the presence of air stream enhances the liquid jet instability and energy

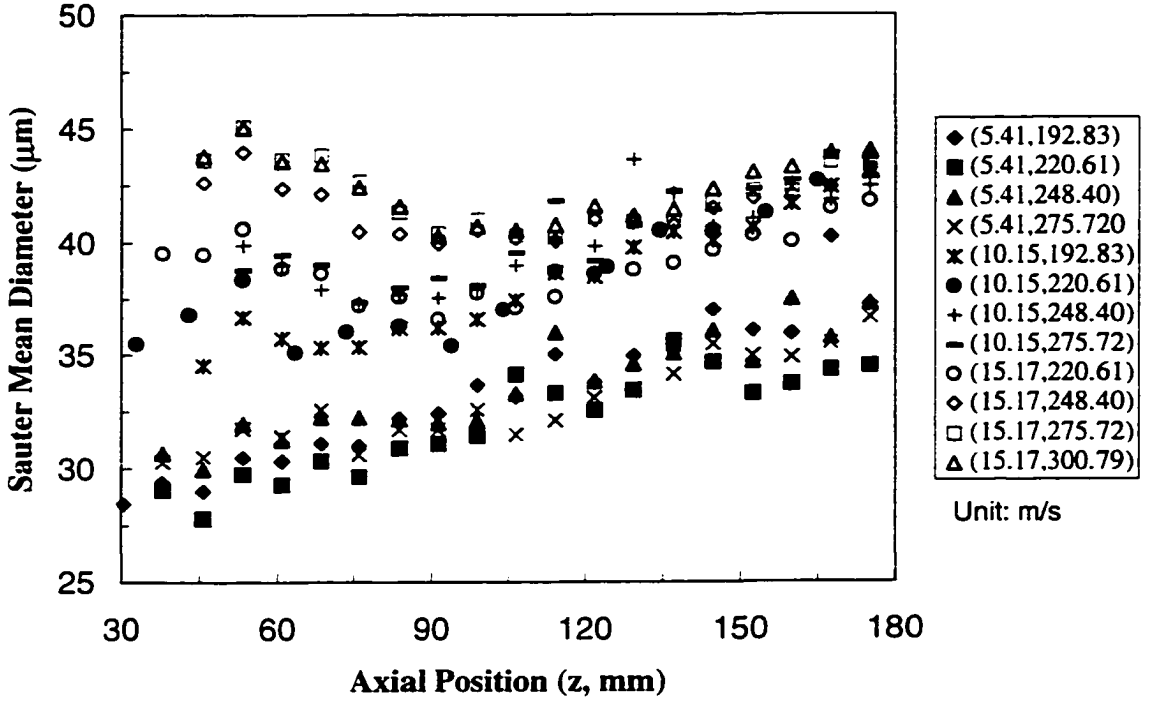

Figure 9.22: Effects of water and air velocities on drop Sauter Mean Diameter along the spray axis.

transfer.

On the other hand, the SMD increases generally with the distance from the nozzle exit for a low liquid velocity $U_\ell = 5.41\ m/s$. For the higher liquid velocities, the value of SMD shows an initial decrease followed by a gradual increase along the spray axis. The initial decrease in SMD with z is probably due to secondary atomization and the subsequent increase is due to droplet coalescence [44]. The consideration of the number density could be more helpful to explain this complex variation of droplet sizes. The number density in Figures 9.23 to 9.25 indicates that at a lower liquid velocity, there are larger amounts of drops with smaller sizes. The general increase of the number density with the axial location may be explained by secondary atomization and radial droplet migration which occur progressively along the spray centerline downstream. The initial decrease of the SMD due to the secondary atomization results in an increase in the number density. However, the subsequent increase of the SMD and the number density is the result of the balance between the drop coalescence and secondary atomization effects.

9.2.4 Uncertainty of Measurements

There is a certain degree of uncertainty for the photographic and PDA measurements in this work, just like any other experiments. To estimate this uncertainty, it is necessary to consider all the uncertain effects on the measurements. Then the combined effect can be assessed. Typical uncertainties in the present measurements are described below.

(1) Photographic Measurements

The sources, which may cause uncertainty for the photographic measurements, are:

a. Flowmeter readings for both water (Q_ℓ) and air flowrates (Q_a);

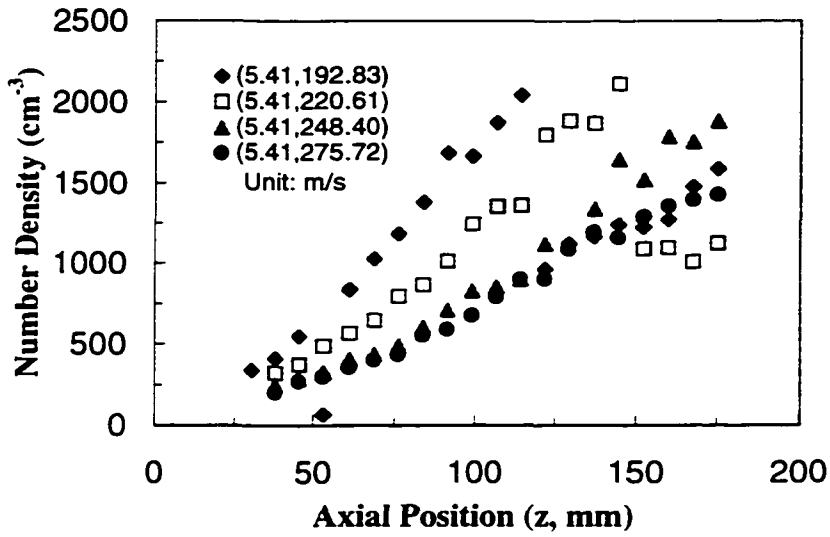

Figure 9.23: Effects of water and air velocities on number density along the spray axis. Water velocity $U_l^* = 5.41\ m/s$.

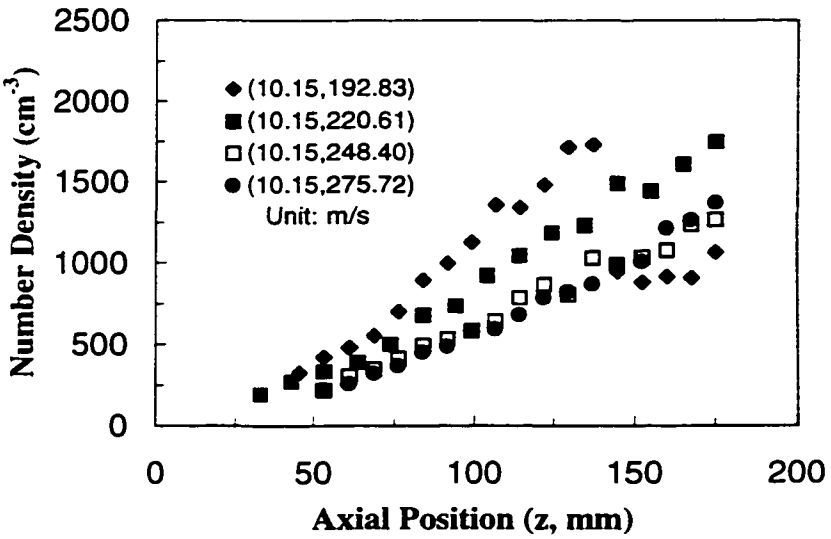

Figure 9.24: Effects of water and air velocities on number density along the spray axis. Water velocity $U_l^* = 10.15\ m/s$.

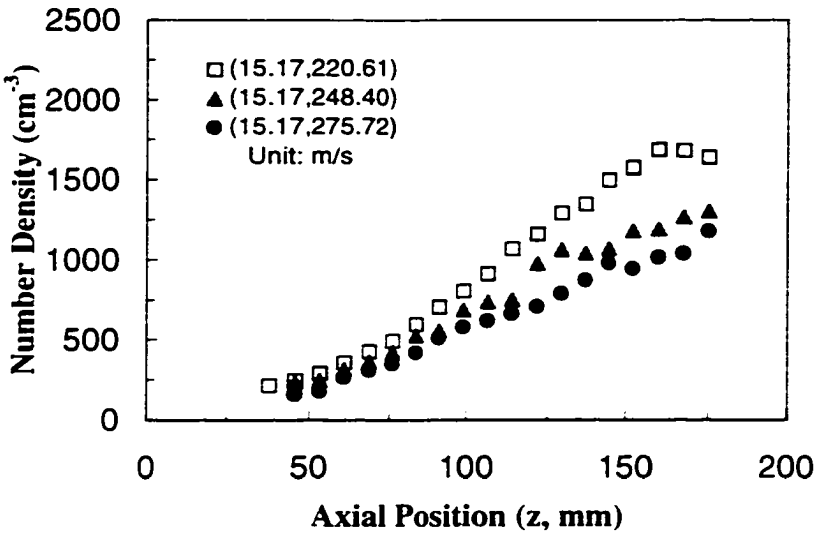

Figure 9.25: Effects of water and air velocities on number density along the spray axis. Water velocity $U_\ell^* = 15.17\ m/s$.

b. Nozzle dimensions causing an uncertainty for the estimation of flow cross section areas (A_ℓ, A_a):

c. Pressure fluctuation in the supply lines:

d. Alignment of the camera relative to the nozzle assembly or annular jets:

e. Sensitivity and resolution of the photographic films and papers:

f. Systematic bias in taking measurements from the magnified projections.

The accuracy of both the water and air flowmeters is ±2.5% of the flowmeter full scale (see Appendix E for the flowmeter specifications). Therefore, the maximum absolute error for the water flowrate is $\delta_{Q_\ell} = 0.025\ GPM$ or $1.58 \times 10^{-6}\ m^3/s$, and $\delta_{Q_a} = 0.15\ SCFM$ or $7.08 \times 10^{-5}\ m^3/s$ for the air flowrate. The absolute error for the nozzle dimensions is $0.01\ mm$ for every diameter measurement, and this yields a

maximum absolute error of $\delta_{A_\ell} = 0.307\ mm^2$ for the water flow cross section area and $\delta_{A_a} = 0.138\ mm^2$ for the air flow cross section area. The estimation of the uncertainty for the water and air velocities is as follows:

$$U_\ell^* = \frac{Q_\ell \pm \delta_{Q_\ell}}{A_\ell \pm \delta_{A_\ell}} \approx \frac{Q_\ell}{A_\ell}\left[1 \pm \left(\frac{\delta_{Q_\ell}}{Q_\ell} + \frac{\delta_{A_\ell}}{A_\ell}\right)\right] \tag{9.6}$$

$$U_a^* = \frac{Q_a \pm \delta_{Q_a}}{A_a \pm \delta_{A_a}} \approx \frac{Q_a}{A_a}\left[1 \pm \left(\frac{\delta_{Q_a}}{Q_a} + \frac{\delta_{A_a}}{A_a}\right)\right] \tag{9.7}$$

The relative errors estimated by the above equations are ±9.2% for the water velocity and ±12% for the air velocity.

Unfortunately, the other error sources are difficult to estimate quantitatively. Therefore, their estimations are not given here.

(2) PDA Measurements

The sources causing uncertainty for PDA measurements are:

a Flowmeter readings for both water (Q_ℓ) and air flowrates (Q_a);

b Nozzle dimensions causing an uncertainty of the estimation of flow cross section areas (A_ℓ, A_a);

c Pressure fluctuation in the supply lines;

d Optical alignment of the PDA instrument;

e Accuracy of PDA instrument;

f Random errors in taking measurements.

The uncertainties for the water and air velocity can be estimated similarly to the previous case for the photographic measurements. Since the accuracy of the water and air flowmeters is ±2.0% of the flowmeter full scale, the maximum absolute errors

are $\delta_{Q_\ell} = 23.72\ ml/min$ for water flowrate readings and $\delta_{Q_a} = 778\ ml/min$ for the air flowrate. The absolute error for the nozzle dimensions is 0.01 mm for every diameter measurement, and this yields a maximum absolute error of $\delta_{A_\ell} = 0.0772\ mm^2$ for the water flow cross section area and $\delta_{A_a} = 0.025\ mm^2$ for the air flow cross section area. The maximum relative errors estimated by Eqs. (9.6) and (9.7) are $\pm 17\%$ for the water velocity and $\pm 4.66\%$ for the air velocity in the PDA measurements.

The PDA based on laser Doppler interferometry almost becomes a standard instrument to characterize the sprays in recent years. It has self-calibration built in the system, and is verified to have high accuracy for measurements by the manufacture. Besides, the PDA used in this work has been calibrated using a single droplet generator [76]. The droplet size measured was compared with the theoretical prediction by Rayleigh [8], and the accuracy is 0.6%.

9.3 Summary

The experimental investigations for the jet breakup characteristics and spray formation mechanism of annular water jets exposed to inner air streams have been presented in this chapter. The photographic measurements identify three regimes, bubble formation, annular jet formation and atomization regime, for the jet disintegration process. Within the bubble formation regime, the jet breakup characteristics are measured from the photographs taken under various liquid and gas velocities. The results show that a uniform size of bubbles are observed for various air-to-water velocity ratios. This bubble size, almost independent of the air-to-water velocity ratio, has an average diameter of 24.61 mm or 2.46 times of the nozzle mean diameter. The jet breakup and wave lengths are found to decrease with the air-to-water velocity ratio. This means that they both increase as the liquid flowrate increases or as the

air flowrate decreases. However, the effectiveness of the air-to-water velocity ratio is limited. Under certain conditions, further increase in the liquid velocity or decrease in the air velocity has no effect on the jet breakup and wave length. The comparison of the photographic measurements with the predictions by the linear instability analysis shows certain degree of agreement. However, the linear instability theory may be necessary to be modified with non-linear effects for the better predictions of the experimental results in future works.

The study of the formation mechanism of the sprays by a Phase Doppler Particle Analyzer indicates that using atomizing air enhances the jet breakup process and improves the atomization performance by producing fine sizes of droplets and increasing the uniformity of drop sizes. The spray characteristic parameters, such as drop mean diameter, velocity, velocity fluctuation and number density, are symmetric about the spray axis. At each plane perpendicular to the spray axis, the mean axial velocity measured reaches the maximum value in the spray center and decreases from the spray center to the edge. The drop axial velocity has a jet-type self similar spatial distribution according to the velocity correlations. Along the spray axis at the different axial locations, the drop axial mean velocity increases with the water and air flowrates or velocities. But the effect of the water and air velocities becomes small when either water or air flowrate is high. A monotonic decrease is found for the axial mean velocity as the distance from the nozzle exit increases along the spray axis. The SMD is a minimum in the spray center and has global increase from the spray center to the edge. Along the spray axis, the SMD has a more complex variation. The water and air flowrates also have complex effects on the SMD. Generally, the SMD is reduced by increasing the air flowrate or velocity and increased with the liquid flowrate or velocity.

Chapter 10

Conclusions

The interfacial instability and breakup process of annular viscous liquid jets subjected to inner and/or outer gas streams and the characteristics of the resultant sprays have been investigated in this thesis. The thesis contains two parts. In the first part, a theoretical analysis based on the linear instability theory is carried out for the instability of annular liquid jets. In the second part, an experimental investigation is conducted out for the formation and characteristics of the sprays from the annular liquid jet breakup. The flow visualization by photography is performed to assess the jet breakup mechanism, and a Phase Doppler Particle Analyzer is used to characterize the resultant sprays.

10.1 Linear Instability Analysis

A general form of dispersion relation, which states the relation between the complex wave number and frequency of disturbances, has been derived for the annular viscous liquid jet exposed to both internal and external inviscid gas streams of unequal velocities by applying the linear instability theory. The equations for the amplitude ratio

of initial disturbances at the two gas-liquid interfaces are also obtained. As a check to the equations derived, the dispersion relations for three limiting cases of plane liquid sheets, cylindrical gas jets and cylindrical liquid jets are retrieved from that for the annular liquid jet by using appropriate approximations for the radii of the annular jet. The dispersion relations are then solved numerically by using Muller's method.

The numerical results based on the temporal analysis reveal the effects of the jet geometric parameters and various flow parameters on the jet breakup processes. It is found that there exist two independent unstable modes, para-sinuous and para-varicose, for the annular jet instability. The para-sinuous mode of interfacial waves outgrows the para- varicose one at relatively low gas-liquid density ratios and large Weber numbers. For the practical importance of large Weber numbers such as related to liquid atomization, the para-sinuous mode is always predominant. The curvature of the annular jet in general promotes the jet instability, and may not be neglected for the breakup processes of annular liquid jets. Not only the velocity difference across each interface but also the absolute velocity of each fluid is important for the jet instability, although the effect of absolute velocity is secondary compared to that of the relative velocity. Co-flowing gas at high velocities is found to significantly improve atomization performance. A high velocity gas inside of the annular liquid jet exhibits a larger effect on the jet breakup process than a gas stream outside of the jet with the equivalent velocity. The velocity difference across any of two gas-liquid interfaces also plays an important role in other parametric effects on the jet instability. In practical twin-fluid atomization, where there always exists a velocity difference between liquid and gas, the atomization performance is therefore enhanced by an increase in the liquid inertia, density ratio and relatively large gas velocity, and suppressed by the effect of surface tension and liquid viscosity.

A mesh-searching method has been developed in this thesis to determine absolute

mode of instabilities. Absolute and convective instabilities are identified, for the first time, for annular liquid jets in moving gas streams. Two solutions, para-sinuous and para-varicose, exist for both absolute and convective instability under certain flow conditions. For para-sinuous mode, the annular liquid jet with an inner gas moving at relatively small velocity could have convective or absolute instability depending on specific flow conditions. However, the jet is of only absolute instability if the inner gas is either stationary or moves at sufficiently large velocity. Para-sinuous unstable waves outgrow para-varicose ones, and hence dominate the jet instability according to both the absolute and convective instability analysis. The liquid viscosity has a simple stabilizing effect on the jet instability while the gas inertial force shows fairly complex influence on the absolute instability of the jet. The convective growth rates for various inner gas velocities shows that not only the velocity difference between, but also the absolute velocity of the liquid and gas, determines the jet breakup process.

10.2 Experimental Measurements

In the second part of this thesis, experimental investigations have been performed for the breakup process of an annular water jet exposed to an inner air stream and for the formation and characteristics of the resultant sprays. Two annular nozzles of the same structure but different dimensions are designed and constructed with smooth contraction for the liquid flow. The test apparatus constructed in this work consists of the water and air supply system, flowmeters and pressure regulating systems. It is used, when a nozzle is connected to the water and air pipelines, to produce the annular liquid jets or sprays of good quality.

Photographic measurements have identified three regimes, i.e., bubble formation, annular jet formation and atomization regime, for the jet breakup process. Within

the bubble formation regime, the jet breakup characteristics are measured from the photographs taken under various liquid and gas velocities. The results show that a uniform size of bubbles is observed for various air-to-water velocity ratios. This bubble size, almost independent of the air-to-water ratio, has an average diameter of 24.61 *mm* or 2.461 times of the nozzle diameter. The jet breakup and wave lengths are found to decrease with the air-to-water velocity ratio. However, the effectiveness of the air-to-liquid ratio is limited. Under certain conditions, further increase in the liquid velocity or decrease in the air velocity has no effect on the jet breakup and wave length. The comparison of the photographic measurements with the predictions by the linear instability analysis indicates a certain degree of agreement. However, the prediction of the jet breakup characteristics by the linear instability theory needs to be modified by including non-linear effect and gas compressibility effect in the future work.

The study of the formation mechanism of the sprays from annular liquid jet breakup by a Phase Doppler Particle Analyzer indicates that using atomizing air enhances the jet breakup process and improves the atomization performance by producing fine sizes of droplets and increasing the uniformity of drop sizes. Spray characteristic parameters, such as drop mean diameter, axial mean velocity, velocity fluctuation and number density, are symmetric about the spray axis. The drop axial velocity has a jet-type self-similar spatial distribution in the radial direction, and decreases monotonically along the spray axis. Increase in the water and air velocities results in higher drop axial velocity. But the effect of the water and air velocities has a certain limit. The droplet size described by its Sauter mean diameter (SMD) reaches a minimum value at the central region of the spray and increases towards the spray edge. The SMD has a complex variation along the spray axis. Under the conditions of relatively low water flowrates, it increases as the distance from the nozzle exit

increase. However at relative high water flowrates, the SMD decreases initially and then increases along the spray axis downstream. The results also suggest that the aerodynamic interaction between the liquid and gas, drop collision and coalescence and transport may be important for the liquid atomization using atomizing air.

Chapter 11

Recommendations for Future Works

Based on both the theoretic and experimental investigations that have been done for the annular liquid jets and the resultant sprays in this thesis, the further works on the following aspects are recommended:

(a) The gas compressibility and non-linear effects may be considered in instability analyses so that the agreement of the predictions by the theory with experiments can be improved;

(b) More annular nozzles with different dimensions are necessary to examine the geometric effects of nozzles on the bubble formation and spray characteristics;

(c) Working fluids other than water as the dispersed liquid and air as the atomizing gas may be tested;

(d) The test apparatus can be modified to provide more flexibilities for the selection of the liquid and gas flowrate ranges.

References

[1] A. H. Lefebvre. Twin-fluid atomization: Factors influencing mean drop size. Keynote Lecture ICLASS-91, Paper D, School of Mechanical Engineering, Purdue University, Gaithersburg, MD, U.S.A., July 1991.

[2] N. Chigier. Spray science and technology. *Fluid Mechanics and Heat Transfer in Sprays, ASME*, FED-Vol. 178/HTD-Vol. 270:1–18, 1993.

[3] F. M. White. *Viscous Fluid Flow*. 2nd ed., McGraw-Hill, Inc., New York, 1991.

[4] R. J. Briggs. *Electron Stream Interaction with Plasmas*. MIT Press, Cambridge, MA, U. S., 1964.

[5] A. Bers. Space-time evolution of plasma instabilitys-absolute and convective. *Handbook of Plasma Physics*, 1:451–517, 1983.

[6] L. Rayleigh. On the instability of jets. *Proceedings of London Mathematical Society*, 10:4–13, 1879.

[7] L. Rayleigh. A cylinder of viscous liquid under capillary force. *Philosophical Magazine*, Vol. 34:145–154, 1892.

[8] L. Rayleigh. On the instability of cylindrical fluid surfaces. *Scientific Papers, Cambridge, England*, Vol. III:594–596, 1902.

[9] C. Weber. Zum zerfall eines flussigkeitsstrahles (disintegration of a liquid jet). *Zeitschrift Fu Angewandte Mathematik Und Mechanik*, 11:136–154, 1931.

[10] A. M. Sterling and C. A. Sleicher. The instability of capillary jets. *Journal of Fluid Mechanics*, 68(3):477–495, 1975.

[11] S. P. Lin and D. J. Kang. Atomization of a liquid jet. *Physics Fluids*, 30(7):2000–2006, 1987.

[12] C. Chandrasekhar. *Hydrodynamic and Hydromagnetic Stability*. New York: Oxford University Press., 1961.

[13] J. B. Keller, S. I. Rubinow and Y. O. Tu. Spatial instability of a jet. *Physics Fluids*, 16(12):2052–2055, 1973.

[14] L. D. Landau and E. M. Lifshitz. *Fluid Mechanics*. Pergamon Press, London, 1959.

[15] R. Betchov and W. O. Criminale. *Stability of Parallel Flows*. Academic Press, New York, 1967.

[16] G. E. Mattingly and W. O. Criminale. Disturbance characteristics in a plane jet. *Physics of Fluids*, 14:2258–2264, 1971.

[17] S. C. Crow and F. H. Champagne. Stability of an incompressible two-dimensional wake. *Journal of Fluid Mechanics*, 51:233–272, 1971.

[18] J. M. Kendall. Hydrodynamic performance of an annular liquid jet: Production of spherical shells. In D. H. LeCroissette, editor, *Proceedings of 2nd International Colloquium on Drops and Bubbles*, number 19-21, pages 79–87, Monterey, CA, 1982. Jet Propulsion Laboratory Publication.

[19] C. P. Lee and T. G. Wang. A theoretical model for the annular jet instability. *Physics Fluids*, 29(7):2076–2085, 1986.

[20] J. M. Kendall. Experiments on annular liquid jet instability and on the formation of liquid shells. *Physics Fluids*, 29(7):2086–2094, July 1986.

[21] C. P. Lee and T. G. Wang. The theoretical model for the annular jet instability-revised. *Physics Fluids A*, 1(6):967–974, 1989.

[22] A. M. Binnie and H. B. Squire. Liquid jets of annular cross section. *The Engineer*, 171:236–238, 1941.

[23] G. N. Lance and R. L. Perry. Water bells. In *Proceedings of Physics Society*, volume B66, pages 1067–1072, 1953.

[24] M. H. I. Baird and J. F. Davidson. Annular jets-I: Fluid dynamics, -II: Gas absorption. *Chemical Engineering Science*, 17:467–479, 1962.

[25] G. Walker and R. A. East. Shock tube studies of a water sheet inertial energy absorber to reduce blast overpressure. In *Proceedings of Shock and Blast Wave Phenomena Symposium*, Paper C-2, page 16, Cranfield, U. K., 1984.

[26] K. Masters. *Spray Drying Handbook*. John Wiley, New York, 4th edition, 1985.

[27] A. H. Lefebvre. *Atomization and Sprays*. Hemisphere, New York, 1989.

[28] E. O. Tuck. Annular water jets. *IMA Journal of Applied Mathematics*, 29:45–58, 1982.

[29] C. H. Hertz and B. Hermanrud. A liquid compound jet. *Journal of Fluid Mechanics*, 131:271–287, 1983.

[30] A. Sanz and J. Meseguer. One-dimensional linear analysis of the compound jet. *Journal of Fluid Mechanics*, 159:55–68, 1985.

[31] G. C. Gardner and T. Lloyd. Annular buoyant jets. *International Journal of Multiphase Flow*, 10(5):635–641, 1984.

[32] H. B. Squire. Investigation of the instability of a moving liquid film. *British Journal of Applied Physics*, 4:167–169, June 1953.

[33] W. W. Hagerty and J. F. Shea. A study of the stability of plane fluid sheets. *Journal of Applied Mechanics*, 22:509–514, 1955.

[34] N. Dombrowski and W. R. Johns. The aerodynamic instability and disintegration of viscous liquid sheets. *Chemical Engineering Science*, 18:203–214, 1963.

[35] G. D. Crapper, N. Dombrowski and G. A. D. Pyott. Large amplitude Kelvin-Helmholtz waves on thin liquid sheets. *Proceedings of Royal Society, London*, A342:209–224, 1975.

[36] X. Li and R. S. Tankin. On the temporal instability of a two-dimensional viscous liquid sheet. *Journal of Fluid Mechanics*, 226:425–443, 1991.

[37] X. Li. Spatial instability of plane liquid sheets. *Chemical Engineering Science*, 48:2973–2981, 1993.

[38] X. Li. On the instability of plane liquid sheets in two gas streams of unequal velocities. *Acta Mechanica*, 106:137–156, 1994.

[39] G. I. Taylor. Formation of thin flat sheets of water. In *Proceedings of Royal Society*, volume A 259, pages 1–17, 1960.

[40] D. Weihs. Stability of thin, radially moving liquid sheets. *Journal of Fluid Mechanics*, 87:289–298, 1978.

[41] G. D. Crapper, N. Dombrowski and G. A. D. Pyott. Kelvin-Helmholtz wave growth on cylindrical sheets. *Journal of Fluid Mechanics*, 68(3):497–502, 1975.

[42] J. Meyer and D. Weihs. Capillary instability of an annular liquid jet. *Journal of Fluid Mechanics*, 179:531–545, 1987.

[43] J. G. Lee and L. D. Chen. Linear stability analysis of gas-liquid interface. *AIAA Journal*, 29(10):1589–1595, 1991.

[44] A. Mansour and N. Chigier. Disintegration of liquid sheets. *Physics of Fluids A*, 2(5):706–719, 1990.

[45] H. Hashimoto and T. Suzuki. Experimental and theoretical study of fine interfacial waves on thin liquid sheet. *JSME International Journal*, Ser. II, 34(3):277–283, 1991.

[46] P. Huerre and P. A. Monkewitz. Local and global instabiities in spatially developing flows. *Annual Review of Fluid Mechanics*, 22:473–537, 1990.

[47] J. Shen and X. Li. Instability of an annular viscous liquid jet. *Acta Mechanica*, 114:167–183, 1996.

[48] J. Shen and X. Li. Breakup of annular viscous liquid jet in two gas streams. *Journal of Propulsion and Power*. Published in 1997.

[49] G. D. Crapper, N. Dombrowski, W. P. Jepson and G. A. D. Pyott. A note on the growth of Kelvin-Helmholgz waves on thin liquid sheets. *Journal of Fluid Mechaincs*, 57(4):671–672, 1973.

[50] M. Gaster. A note on the relation between temporally-increasing and spatially-increasing disturbances in hydrodynamic stability. *Journal of Fluid Mechanics*, 14:222–224, 1962.

[51] S. J. Leib and M. E. Goldstein. The generation of capillary instabilities on a liquid jet. *Journal of Fluid Mechanics*, 168:479–500, 1986.

[52] S. J. Leib and M. E. Goldstein. Convective and absolute instability of a viscous liquid jet. *Physics Fluids*, 29(4):952–954, 1986.

[53] S. P. Lin and Z. W. Lian. Absolute instability of a liquid jet in a gas. *Physics Fluids A*, 1(3):490–493, 1989.

[54] S. P. Lin and B. Creighton. Energy budget in atomization. *Aerosol Science and Technology*, 12:630–636, 1990.

[55] E. A. Ibrahim. Spatial instability of a viscous liquid sheet. *Journal of Propulsion and Power*, 11(1):146–152, 1995.

[56] J. Shen and X. Li. Absolute and convective instability of annular liquid jets. In *Proceedings of Combustion Institute*, Waterloo, Ontario, Canada, 1990. Combustion Institute, Canadian Section, 1996 Spring Technique Meeting.

[57] X. Li and J. Shen. Breakup of cylindrical liquid jets in co-flowing gas streams. In *The Symposium on Emerging Energy Technology, Energy Week'96 Conference and Exhibition*, Houston, Texas, Jan. 22-Feb. 2, 1996. API/ASME.

[58] V. G. Levich. *Physicochemical Hydrodynamics*. Prentice-Hall, New York, 1962.

[59] D. E. Muller. A method for solving algebraic equations using an automatic computer. *Mathematical Tables and Aids to Computation*, 10(5):208–215, 1956.

[60] M. Abramowitz and I. A. Stegun. *Handbook of Mathematical Functions*. Applied Math Series 55. Dover Publication, 1965.

[61] D. W. Lozier and F. W. J. Oliver. Numerical evaluation of special functions. In W. Gautschi, editor, *Proceedings of Applied Mathematics Symposia, Mathematics of Computation 1943-1993: A half-century of Computational Mathematics.* American Mathematical Society, 1994.

[62] R. H. Rangel and W. A. Sirignano. The linear and nonlinear shear instability of a fluid sheet. *Physics Fluids A*, 3(10):2392–2400, 1991.

[63] S. P. Lin and Z. W. Lian. Mechanisms of the breakup of liquid jets. *AIAA Journal*, 28(1):120–126, 1990.

[64] R. D. Reitz and F. V. Bracco. Mechanism of atomization of a liquid jet. *Physics of Fluids*, 25(10):1730–1742, 1982.

[65] U. Shavit and N. Chigier. Fractal dimension measurements of disintegrating coaxial liquid jets. *Fluid Mechanics and Heat Transfer in Sprays, ASME*, FED-Vol.178/HTD-Vol. 270:35–42, 1993.

[66] W. H. Lai, K. H. Yang, C. H. Hong and M. R. Wang. Droplet transport in simplex and air-assisted sprays. *Atomization and Sprays*, 6:27–49, 1996.

[67] C. J. Clark and N. Dombrowski. Aerodynamic instability and disintegration of inviscid liquid sheets. *Proceedings of Royal Society, London*, A329:467–478, 1972.

[68] N. K. Rizk and A. H. Lefebvre. The influence of liquid film thickness on airblast atomization. *Transactions of the ASME*, 102:706–710, July 1980.

[69] B. E. Stapper and G. S. Samuelsen. An experimental study of the breakup of a two-dimentional liquid sheet in the presence of co-flow air shear. In *AIAA Paper*, number 89-0461, Reno, Nevada, 1990. 28th Aerospace Sciences Meeting.

[70] J. G. Lee. *Breakup of Cylindrical Liquid Sheets.* Ph. d. thesis, The University of Iowa, U. S. A., 1990.

[71] G. Lavergne, P. Trichet, P. Hebrard and Y. Biscos. Liquid sheet disintegration and atomization process on a simplified airblast atomizer. *Journal of Engineering for Gas Turbine and Power, Transactions of The ASME*, 115:461–466, July 1993.

[72] J. H. Downie, R. Jordinson and F. H. Barnes. On the design of three-dimensional wind tunnel contractions. *Aeronautical Journal*, Paper No. 1194:287–295, 1984.

[73] W. D. Bachalo and M. J. Houser. Phase/Doppler spray analyzer for simultaneous measurements of drop size and velocity distributions. *Optical Engineering*, 23(5):583–590, 1984.

[74] D. A. Billenness. The design of a flow channel with an investigation of lamminar flow over a square rib. Master's thesis, University of Victoria, B. C., Canada, 1995.

[75] Dantec Measurement Technology A/S. *SIZEware User's Guide.* Tonsbakken 18, 2740 Skovlunde, Denmark, 1992.

[76] T. Chen. Liquid atomization for aerosol application. Master's thesis, University of Victoria,, Victoria, B. C., Canada, 1997.

Appendix A

Comparison of Three Instability Modes

Linear instability analyses can lead to three modes of instabilities for a flow system: temporal, absolute and convective instability. The main differences among three instability modes are presented in Table A.1. When a wave form of $e^{i(\alpha z - \Omega t)}$ is assumed for the normal mode solution, the real part α_r of α represents axial wave number of a disturbance and is related to the disturbance wavelength λ by the relation of $\alpha_r = 2\pi/\lambda$; the imaginary part α_i of α represents spatial growth or decay rate of a disturbance; negative Ω_r of complex number Ω is equal to 2π times of the disturbance frequency, and $-\Omega_r/\alpha$ the wave propagation velocity of the disturbance; Ω_i stands for growth or decay rate of a disturbance with time. For all three instability modes, the numerical values of α_r from the dispersion relation must be positive for a disturbance wave to propagate from a nozzle downstream in the flow direction while the numerical values of Ω_r must be negative for any real flow system.

Table A.1: Comparison of Three Instability Modes

Instability Mode	Physical Description	Mathematical Description
Temporal	Disturbance growth with time only	$\Omega_i > 0$ $\alpha_i = 0$
Absolute	Disturbance growth not only with time but also through space	$\Omega_i > 0$ $\alpha_i < 0$
Convective	Disturbance growth through space only	$\Omega_i = 0$ $\alpha_i < 0$

Appendix B

Summary of Previous Works

B.1 Instability of Annular Liquid Jets

Previous theoretical works on the instabilities of annular liquid jets are listed in the following table. These works are all limited to **temporal instability analyses** for incompressible liquid and incompressible inviscid gas.

Table B.1: Previous Works on Temporal Instability Analyses

Reference	Liquid Jet	Gas Surrounding	Emphases
Crapper [41]	inviscid moving	static inner and outer gas	effects of sheet thickness and radius
Meyer and Weighs[42]	viscous static	moving, equal inner and outer gas velocity	critical "penetration" thickness
Lee and Chen [43]	viscous static	moving, unequal inner and outer gas velocity	effects of liquid viscosity and gas velocity
Present Work	viscous moving	moving, unequal inner and outer gas velocity	effects of liquid viscosity liquid and gas velocity, density, surface tension

B.2 Experiments for Sprays Formed by Annular Nozzles

Table B.2: Previous Experimental Works on Jet Breakup and Spray Formation

Reference	Kendall [20]	Lee [43]	Lavergne [71]	Present Work
Liquid	water, water solutions (containing alcohol, salt, and glycerin),	water	water	water
Gas	air, helium, nitrogen, Freon-12	air	air	air
Nozzle Size	4.0 *mm* O.D. 2.5 *mm* I.D.	22.2 *mm* O.D. 12.7 *mm* I.D.	0.4 *mm* sheet thickness	2.54, 10.00 *mm* O.D. 2.375, 9.525 *mm* I.D.
Technique	photography	photography	photography PDPA	photography PDPA
Emphases	bubble formation	jet breakup	jet breakup drop size and velocity (limited data	jet breakup drop size and velocity

Appendix C

Geometrical Characteristics of Various Jets

There are four types liquid or gas jets which are commonly used in connection with liquid atomization or bubble formation. These jets, cylindrical liquid jet, plane liquid sheet, annular liquid sheet or jet and cylindrical gas jet, have common geometrical characteristics. That is they all have gas-liquid interfaces no matter how many interfaces they have and whether the interfaces are flat or curved. The cylindrical liquid jet, plane liquid sheet and cylindrical gas jet can all be retrieved from an annular liquid jet by certain geometric approaching. If the inner and outer radius of an annular jet are denoted by r_a^* and r_b^* as shown in Figure 4.1, the other type of jets can have the radii as listed in the following table.

Table C.1: Geometrical Characteristics of Various Jets

Jet Type	Inner Radius	Outer Radius	Sheet Thickness
Annular Liquid Sheet	r_a^*	r_b^*	$r_h = (r_b^* - r_a^*)/2$
Cylindrical Liquid Jet	let $r_a^* \to 0$	fix r_b^*	vary r_h
Plane Liquid Sheet	let $r_a^* \to \infty$	$r_b^* \to \infty$	fix r_h
Cylindrical Gas Jet	fix r_a^*	let $r_b^* \to \infty$	vary r_h

Appendix D

Mesh-Searching Method

D.1 Introduction

It is known that in reality the instability and breakup of a liquid jet discharged from a nozzle are due to not only spatially but also temporally growing disturbances. That is the disturbances grow through spatial location and also with time. In linear instability analysis, this is called absolute instability.To find out whether an absolute instability exists for a particular system with disturbances of the form $A_0 \exp[i(kz - \omega t)]$, the analysis usually starts from the dispersion relation $\Re(k, \omega) = 0$, e.g., Eq. (4.18), which implicitly determines an analytical function $\omega(k)$. According to Briggs[4] and Bers[5], it is essential to search for pinch points on the complex k-plane with $\omega_i > 0$ for absolute instabilities. The first step is to locate double roots in k, i.e., the saddle point k_0 of the function $\omega(k)$, and the corresponding ω_0. The second step is to determine whether k_0 is a pinch point with $\omega_{0,i} > 0$, which represents absolute instability. The numerical method used is the mesh-searching technique over the k-plane, which is developed based on the principle outlined by Briggs[4] and Bers[5]. The procedure is given as follows.

D.2 Procedures to Find Pinch Points

(1) Limit the region on k-plane to be searched

This is the most important step. If the region is too small and off the right location, saddle points or pinch points may be missed. If it is too large, the grid over the k-plane may become too coarse for a saddle point to be determined. Further, since numerical solutions of $\Re(k, \omega) = 0$ are sensitive to initial guesses, it is not easy to obtain numerically the same set of solutions over a large region of k. Therefore, it is necessary to solve the equation in an appropriately selected range for the real k_r and imaginary part k_i of k.

To determine the computational region in the k-plane as shown in Figure D.1, the temporal solution need be determined first. If the imaginary part of ω, $\omega_i{}^t$, is positive for a range of real k ($k_i = 0$), the temporal instability exists in a particular flow system. The superscript t here denotes temporal mode. The estimation for the k region can be made according to the cut-off wave number $k_{r,c}{}^t$ and the maximum temporal wave growth rate $\omega_i{}^t{}_{max}$. Since if there is a pinch point k_0 and it represents an absolute instability within the region selected, the corresponding $\omega_{0,i}$ is generally smaller and at most equal to $\omega_i{}^t{}_{max}$, i.e., $0 \leq \omega_{0,i} \leq \omega_i{}^t{}_{max}$ [5]. Therefore, ω_0 must be in the first quadrant of complex ω-plane. On the k-plane, the pinch point k_0 must be in the fourth quadrant for $k_{0,i} \leq 0$ to give a spatial wave growth of the disturbances. The upper limit $k_{r,2}$ for the real part of k should be slightly larger than or at least equal to $k_{r,c}{}^t$. The lower limit $k_{i,1}$ for the imaginary part of k should be of the same order of magnitude as $\omega_i{}^t{}_{max}$ and low enough (or the absolute value is large enough) such that some mappings of the straight lines at constant k_i in the k-plane cross the mapping of the line $k_i = 0$, or the temporal growth rate curve, in the ω-plane from above. The lower limit $k_{r,1}$ may be a little smaller than 0, and the upper limit

$k_{i,2}$ is a little above the real k-axis just to ensure two branches of solutions in the k-plane are complete with the upper branch clearly starting from the upper half k-plane and the lower branch from the lower half k-plane. The grids in the k-plane and the corresponding solution domain in the ω-plane are illustrated in Figure D.1 and D.2.

(2) Determine $\omega(k)$ by solving $\Re(k,\omega)=0$ numerically

Since the dispersion relation for a cylindrical liquid jet has many solutions [13, 51, 52] and only one of them represents truly unstable solution, it is necessary to check and make sure that the unstable solution is always obtained. Usually, it is better to start from the temporal solution at $k_i = 0$, which should be known at this step, and then find all solutions ω at the selected mesh points shown in Figure D.1. The solved $\omega(k)$ at a given k should be within the region shown in Figure D.2.

(3) Locate saddle points of $\omega(k)$ by plotting ω_r or ω_i over the k-plane

Mathematically, a saddle point of $\omega(k)$ can be determined by either

$$\frac{D\omega}{Dk} = \frac{\partial\omega_r}{\partial k_r} - i\frac{\partial\omega_r}{\partial k_i} = 0 \quad \text{or} \quad \frac{D\omega}{Dk} = \frac{\partial\omega_i}{\partial k_i} + i\frac{\partial\omega_i}{\partial k_r} = 0$$

This means that both the real and imaginary part of the above derivatives must be zero. When plotting ω_r or ω_i over the k-plane, the saddle point will be the one where ω_r or ω_i shows a maximum along the k_r-axis and a minimum along the k_i-axis, or vice versa.

(4) Show whether the saddle point found in Step 3 is a pinch point

A contour plot based on the above 3-D mesh plot can be obtained at various constant ω_r or ω_i values in the k-plane. If the two k-roots originate from the opposite sides of the k_r-axis and merge to k_0 when $\omega \rightarrow \omega_0$ from above $\omega_{i,max}{}^t$ in the ω-plane, the point k_0 is a pinch point and it represents the absolute instability if $\omega_{0,i}$ is positive. Otherwise, it is not.

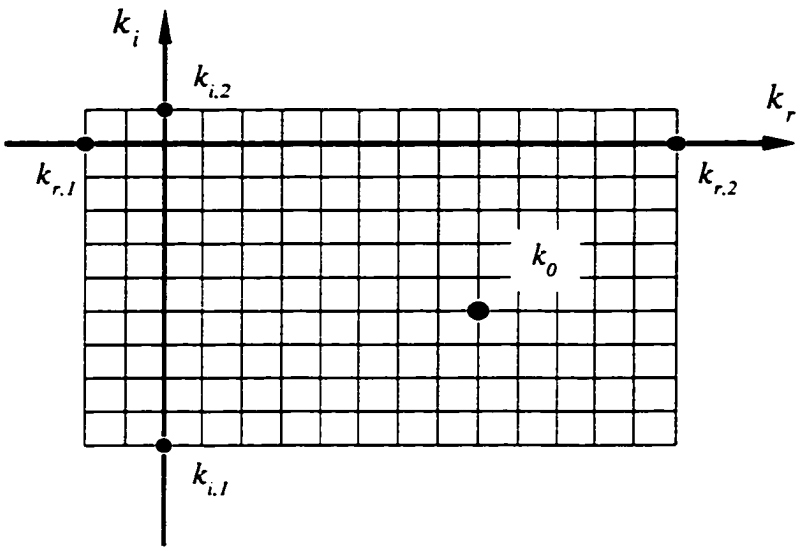

Figure D.1: Solution Domain with computational Meshes in k-plane

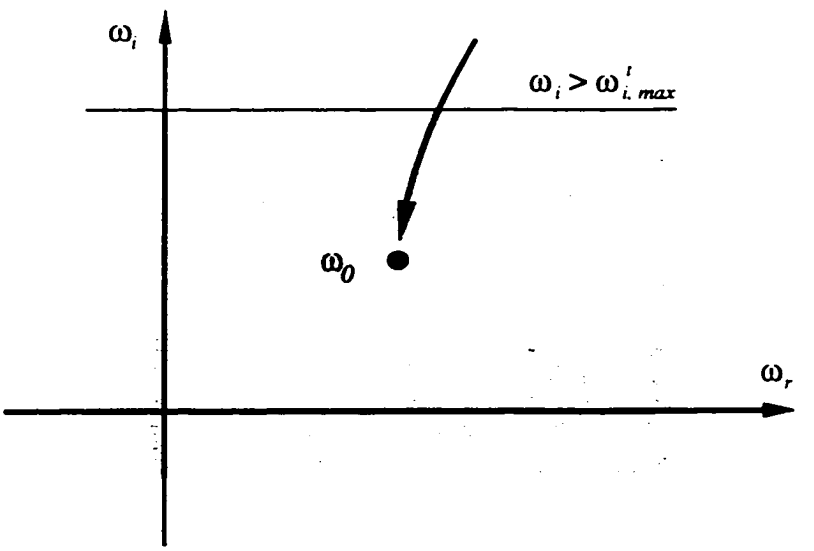

Figure D.2: Solution Domain in ω-plane

Appendix E

Specifications of Test Facilities

E.1 Test Apparatus

Table E.1: Specifications for Test Apparatus-I

Water Tank	Dimension	$\phi 0.61 \times 1.5\ m$
	Max. pressure	100 *psig*
	Material	carbon steel
Compressed Air	Maximum pressure	100 *psig*
	Pressure range	$0 - 100$ *psig*

E.2 Photographic Unit

E.3 Particle Dynamics Analyzer System (PDA)

Figure E.1: Specifications for Test Apparatus-II

Flowmeter A	Model	block-type H-03285-22
	Flowrate range	$0 - 1.0$ GPM (water)
	Max. operating press.	125 *psia*
	Max. operating temp.	54°C
	Full-scale accuracy	±2.5%
	Manufacture	King Instrument Com.
Flowmeter B	Model	block-type H-03291-18
	Flowrate range	$0 - 6$ $SCFM$ (air)
	Max. operating press.	125 *psia*
	Max. operating temp.	54°C
	Full-scale accuracy	±2.5%
	Manufacture	King Instrument Com.
Flowmeter C	Model	Cole-Parmer $65 - mm$ variable area. H-03216-38
	Flowrate range	$0 - 1261$ ml/min (water)
	Max. operating press.	200 *psia*
	Max. operating temp.	121°C
	Full-scale accuracy	±2.0%
	Manufacture	Cole-Parmer Instrument Com.
Flowmeter D	Model	Cole-Parmer 65-mm variable area. H-03216-38
	Flowrate range	$0 - 42094$ ml/min (air)
	Max. operating press.	200 *psia*
	Max. operating temp.	121°C
	Full-scale accuracy	±2.0%
	Manufacture	Cole-Parmer Instrument Com.

Table E.2: Specifications for Photographic Unit

Camera	Model	Pentax-A 135
	Zoom	1:3.5 - 1:4.5
	Lens	28 - 80 mm
	Manufacture	Taiwan
Film	Speed	ISO 400
Strobe	Model	Strobotac 1531
	Frequency range	
	Light intensity	
	Manufacture	GenRad. MA. US
Slide Projector	Model	
	Magnification rate	
	Manufacture	

Table E.3: Specifications for PDA

Transmitting Optics	Model	55X Modular LDA Optics
	Front lens	79mm dia.. 310mm focus length
	Bragg cell	+40 MHz optic frequency shift
	Polarization angle	90°
Receiving Optics	Model	57N10 PDA
	Front lens	Model 55X57. 310 mm focus length
	Polarization angle	90°
	Photomultipliers	55X08
Signal Processor	Model	58N10 PDA
	Dimensions	530 × 470 × 295 mm
Measurement range and accuracy	Size range for droplets	1-10000μm
	Size accuracy	4 %
	Size resolution	9 bits
	Max. velocity:	500 m/s
	Velocity accuracy	1 %
	Max. concentration	$10^6/cm^3$
	Concentration Accuracy:	30 %
Optics	Laser	He-Ne
	Max. Laser power	5 W
	Configuration	near backward backscatter
	Standard measuring distance	310 mm
Electronics	Max. frequency range	-6 to +30 MHz
	Max. bandwidth	36 MHz (6 selectable ranges)
	Input filter flatness	0.5 dB p-p (over 85 % of bandwidth) -1 dB at band edges
	Min. burst length	280 ns between $1/e^2$ levels
	RMS phase error	0.5° at S/N=+6 dB
		3.6° at S/N=0 dB
	Max. data rate	170000 particles/s at 100000 part/s typically less than 10 % loss of data
	Max. dead time	800 ns, typically 500 ns
	Phase resolution	8 bits
	Frequency resolution	typically 8 bits
	Arrival time resolution	1 $\mu s/bit$
	Transit time resolution	2.7 $\mu s/bit$

Appendix F

Original Experimental Data

F.1 Jet Breakup Characteristics

By using a Pentax-A 135 camera, numbers of photographs have been taken for annular liquid jets at various inner air Q_a and water flow rates Q_ℓ at a fixed nozzle dimension. The test conditions for this set of data are presented in Tables 8.2to 8.4. The original measurements from the magnified images of negatives by a slide projector are listed in Tables F.1 to F.4, only for low inner air flow rates when clear wave growth is present in the liquid jet. The magnification rates of the data are 7.99 : 1, 8.0 : 1, 6.67 : 1 and 6.5 : 1 for the water flowrates of 0.2, 0.25, 0.3 and 0.4 GPM, respectively. The variables listed in the tables are denoted in Figure 9.5.

To obtain the data in real dimensions, the arithmetical average is taken for the original measurements of all negatives at one flow condition, and dividing by the corresponding magnification rate mr. In this way, the interface deformation of the annular sheet described by η_1, η_2 and η_3 at the corresponding axial location z_1, z_2 and z_3 is estimated and presented in Table F.5, with $\eta_i = r_i - r_m^*$ $[i = 1, 2, 3;\ r_m^* = (r_b^* + r_a^*)/2]$.

The standard deviations due to multi-photo measurements are presented in Table F.5 also.

Table F.1: Measurements from Magnified Images for $Q_\ell = 0.20\ GPM$ (unit: mm)

Q_a (SCFM)	Negative Number	z_1	r_1	z_2	r_2	z_3	r_3	L_B	L_1
0.5	0.2[1] 5	83	55	351	8	536	94	660	394
	6	75	48	272	27	485	94	588	361
	7	70	49	266	19	476	95	592	376
	8	69	49	270	22	475	95	594	370
	9	89	70	347	11	539	95	667	
1.0	10	100	50	247	16	435	83	565	294
	11	135	52	259	19	459	98	598	
	12	238	71	355	9	540	92	637	
	13	80	45	190	29	416	88	500	370
	14	251	69	374	13	557	92	678	307

Q_a (SCFM)	Negative Number	$D_{1,S}$	$D_{1,L}$	L_2	$D_{2,S}$	$D_{2,L}$	L_3	$D_{3,S}$	$D_{3,L}$
0.5	0.2[1] 5	187	300		192	230			
	6	210	215						
	7	190	195	395	188	227			
	8	196	270						
	9								
1.0	10	215	240		175	186			
	11								
	12				195	220			
	13	215	250	314	185	220			
	14	175	227	320	215	190			

F.2 Spray Characteristics

The characteristics of hollow-cone sprays formed from an annular nozzle (Nozzle B) are measured at different locations within the sprays for various water and air

flowrates by using Dantec Particle Dynamics Analyzer (PDA). Three groups of data are obtained with the first group for checking the symmetry of the spray, the second group for spatial distribution of the spray characteristics and the third group about the effects of the water and air flowrates or velocities. The representative variables for spray characteristics presented here are the arithmetical mean axial velocity, velocity fluctuation (RMS), turbulent intensity, Sauter Mean and arithmetical mean diameter, number density and volume flux over 50000 validated drop samples.

Table F.2: Measurements from Magnified Images for $Q_\ell = 0.25\ GPM$ (unit: mm)

Q_a (SCFM)	Negative Number	z_1	r_1	z_2	r_2	z_3	r_3	L_B	L_1
0.5	0.2[2] 22	55	43	182	32	380	81	480	320
	23	36	42	121	38	339	73	440	310
	24	183	53	356	9	502	95	614	340
	25	80	48	320	12	488	96	582	313
1.0	0.25[1] 0	64	48	300	13	480	95	580	327
	1	92	48	400	11	570	99	667	327
	2	42	42	141	41	314	64	444	354
	3	88	47	330	18	501	97	595	350
	4	76	46	330	19	506	94	605	356
1.5	5	49	44	230	27	408	94	515	325
	6	37	44	218	29	396	91	490	298
	7	86	47	254	17	422	93	525	317
	19	45	41	165	31	332	88	434	300
	20	34	40	99	37	279	79	375	293
Q_a (SCFM)	Negative Number	$D_{1,S}$	$D_{1,L}$	L_2	$D_{2,S}$	$D_{2,L}$	L_3	$D_{3,S}$	$D_{3,L}$
0.5	0.2[2] 22	193	202	388	188	194	333	178	185
	23	194	195	353	165	204	350	185	205
	24	190	195	348	183	187	357	180	198
	25	190	198	318	183	194			
1.0	0.25[1] 0	185	195	365	185	190	375	180	205
	1	197	200	355	198	198	433	198	198
	2	198	202	360	188	203	354	190	195
	3	185	200	336	200	190			
	4	185	204	381	188	215			
1.5	5				185	210	280	185	190
	6	199	200	315	173	204	275	188	218
	7	186	208	322	172	214	270	183	187
	19	184	235	303	172	205			
	20	177	235	303	160	207	310	185	193

Table F.3: Measurements from Magnified Images for $Q_\ell = 0.3\ GPM$ (unit: mm)

Q_a (SCFM)	Negative Number	z_1	r_1	z_2	r_2	z_3	r_3	L_B	L_1
0.5	0.3[2] 3			140	38	261	45	330	
	4					255	42	394	330
	5					284	49	422	365
	6	76	37	241	33	460	63	545	375
1.0	9	38	35	100	33	293	64	370	257
	10					249	54	323	235
	11					205	60	302	271
	12	100	37	227	19	381	79	455	257
	13					158	44	265	263
1.5	14	178	49	257	17	395	78	483	255
	15					225	62	290	227
	16					196	59	270	229
	17	191	47	265	22	403	78	482	
	18	52	39	180	17	322	75	430	230

Q_a (SCFM)	Negative Number	$D_{1,S}$	$D_{1,L}$	L_2	$D_{2,S}$	$D_{2,L}$	L_3	$D_{3,S}$	$D_{3,L}$
0.5	0.3[2] 3				158	165			
	4	169	150	390	150	164	315	148	160
	5	175	150	390	155	160	380	155	160
	6	138	173	378	160	160			
1.0	9	160	189	274	137	175	257	165	165
	10	167	170	282	142	180	264	160	170
	11	163	170	248	145	168	238	155	177
	12	160	173	280	140	153	255	155	165
	13	173	175	268	165	170	257	145	180
1.5	14	143	190						
	15	140	160						
	16	143	150						
	17								
	18	170	210						

Table F.4: Measurements from Magnified Images for $Q_\ell = 0.4\ GPM$ (unit: mm)

Q_a (SCFM)	Negative Number	z_1	r_1	z_2	r_2	z_3	r_3	L_B	L_1
0.5	0.3[1] 19	195	40	503	32	748	55	874	510
	20	170	39	355	35	608	41	868	454
	24	194	40	632	24	824	66	933	448
1.0	0.4[1] 0	140	37	358	24	537	69	630	356
	1	143	37	334	24	523	65	615	344
	2	142	37	332	28	518	62	615	350
1.5	4	79	35	194	25	340	67	434	267
	5	159	44	284	10	417	74	518	265
	6	195	46	310	8	445	74	537	263
	7	211	45	312	8	450	76	550	255
	8	95	36	203	24	356	69	438	250
2.0	9	56	34	134	28	261	71	350	237
	10	28	34	110	29	236	67	323	255
	11	35	33	47	33	186	57	260	234
	12	39	31	85	30	214	62	290	235
	13	81	39	165	24	303	72	396	230

Q_g (SCFM)	Negative Number	$D_{1,S}$	$D_{1,L}$	L_2	$D_{2,S}$	$D_{2,L}$	L_3	$D_{3,S}$	$D_{3,L}$
0.5	0.3[1] 19	130	160						
	20	138	150	120	120	345			
	24	145	165						
1.0	0.4[1] 0	125	160						
	1	128	160	333	160	165			
	2	135	167	365	155	170			
1.5	4	146	180	250					
	5	160	167	239	150	168	216	145	150
	6	160	162	233	148	167	210	147	160
	7	148	160	245	150	158			
	8	148	168	259					
2.0	9	167	190						
	10	147	200						
	11	130	230						
	12	154	180						
	13	157	175						

Table F.5: Interface Deformation Estimated from Photographic Measurements

U_l^* (m/s)	U_a^* (m/s)	z_1 (mm)	η_1 (mm)	z_2 (mm)	η_2 (mm)	z_3 (mm)	η_3 (mm)
1.732	3.854	9.662	1.902	37.697	-2.704	62.854	6.959
	7.708	20.125	2.303	35.670	-2.729	60.250	6.458
2.165	3.854	11.063	0. 931	30.594	-2.038	53.406	5.900
	7.708	9.050	0.894	37.525	-2.331	59.275	6.344
	11.562	6.275	0.519	24.150	-1.356	45.925	6.244
2.598	3.854	11.394	0.666	28.561	0.441	47.226	2.578
	7.708	10.345	0.516	24.513	-0.983	38.561	4.144
	11.562	21.039	1.865	35.082	-2.083	46.207	5.673
3.465	3.854	28.667	1.221	76.410	-0.215	111.795	3.426
	7.708	21.795	0.811	52.513	-0.984	80.923	5.170
	11.562	22.738	1.457	40.092	-2.574	61.785	6.196
	15.416	7.354	0.380	16.646	-0.450	36.923	5.242

U_l^* (m/s)	U_a^* (m/s)	Sd_{z_1} (mm)	Sd_{η_1} (mm)	Sd_{z_2} (mm)	Sd_{η_2} (mm)	Sd_{z_3} (mm)	Sd_{η_3} (mm)
1.732	3.854	0.964	1.036	4.893	0.876	3.635	0.061
	7.708	8.848	1.321	8.665	0.847	7.098	0.621
2.165	3.854	7.093	0.548	12.069	1.560	8.682	1.210
	7.708	2.261	0.278	10.765	1.341	10.695	1.627
	11.562	2.336	0.310	6.923	0.815	6.735	0.675
2.598	3.854	0.000	0.000	5.354	0.265	12.656	1.206
	7.708	2.939	0.095	6.021	0.664	11.465	1.734
	11.562	7.280	0.502	4.451	0.274	12.761	1.231
3.465	3.854	1.778	0.073	17.411	0.714	13.763	1.574
	7.708	0.192	0.000	1.817	0.290	1.237	0.441
	11.562	8.103	0.724	7.959	1.200	6.995	0.524
	15.416	2.921	0.406	6.222	0.450	6.161	0.867

Table F.6: PDA Measurements in two Orthogonal Radial Directions-I

$z = 5.040\ inch$

$Q_\ell = 388.00\ ml/min$ $Q_a = 26200.00\ ml/min$
$P_{tank} = 60 \pm 2\ psig$ $r_m{}^* = 9.7625\ mm$
$PDA\ Samples = 50,000$

Radial Position	Axial Velocity $U_z\ (m/s)$		Diameter $D\ (\mu m)$		Number Density	Volume Flux	Turbulent Intensity
$x\ (inch)$	$Mean$	RMS	SMD	$Mean$	(cm^{-3})	$(cm^3/s.cm^2)$	(%)
23.560	2.804	2.339	88.379	45.557	4753	0.09682	83.433
23.660	3.426	2.554	83.149	40.582	4905	0.10579	74.543
23.760	4.655	2.983	77.279	38.676	3618	0.10031	64.091
23.860	5.993	3.294	75.315	39.853	2613	0.09995	54.964
23.960	7.873	3.648	70.443	37.878	1943	0.08375	46.338
24.060	9.365	4.010	67.281	38.299	1535	0.07651	42.815
24.160	10.972	4.195	65.219	38.470	1304	0.07548	38.229
24.260	12.990	4.334	62.276	38.912	1005	0.06834	33.366
24.360	14.798	4.390	60.238	39.031	899	0.06781	29.665
24.460	16.449	4.328	57.835	38.582	860	0.06847	26.309
24.560	17.089	5.003	59.455	42.297	1414	0.13342	29.277
24.660	18.085	4.995	60.092	43.537	1172	0.12617	27.619
24.760	18.157	4.894	57.689	40.984	1282	0.11674	26.954
24.860	17.763	5.001	58.724	42.318	1354	0.12962	28.153
24.960	17.418	4.308	58.406	41.748	792	0.07716	24.734
25.060	16.420	4.271	57.500	40.010	832	0.06939	26.011
25.160	14.688	4.435	59.823	41.523	974	0.07853	30.196
25.260	12.531	4.370	62.761	42.709	1049	0.08586	34.871
25.360	10.755	4.230	64.379	43.594	1431	0.10267	39.329
25.460	8.774	4.081	65.458	41.287	1682	0.09050	46.511
25.560	7.369	3.836	67.482	43.095	2191	0.10832	52.051
25.660	5.901	3.435	70.129	43.674	2795	0.11359	58.202
25.760	4.538	3.077	74.161	46.455	3836	0.13754	67.800
25.860	3.517	2.765	76.189	46.549	5244	0.15011	78.639
25.960	2.685	2.373	78.955	49.395	5552	0.12987	88.366

Table F.6: PDA Measurements in two Orthogonal Radial Directions-II

$z = 5.040\ inch$							
$Q_\ell = 388.00\ ml/min$				$Q_a = 26200.00\ ml/min$			
$P_{tank} = 60 \pm 2\ psig$				$r_m^* = 9.7625\ mm$			
$PDA\ Samples = 50,000$							
Radial Position	Axial Velocity $U_z\ (m/s)$		Diameter $D\ (\mu m)$		Number Density	Volume Flux	Turbulent Intensity
$y\ (inch)$	$Mean$	RMS	SMD	$Mean$	(cm^{-3})	$(cm^3/s.cm^2)$	(%)
23.560	2.860	2.457	81.860	41.360			85.909
23.660	4.145	2.860	77.840	38.420			68.999
23.760	5.535	3.333	74.100	36.800			60.217
23.860	7.438	3.761	72.070	38.160			50.565
23.960	9.311	4.115	69.270	38.220			44.195
24.060	11.140	4.381	65.940	37.940			39.327
24.160	13.240	4.642	62.190	37.420			35.068
24.260	15.610	4.666	60.430	39.140			29.890
24.360	17.370	4.630	58.090	38.380			26.655
24.460	18.060	5.373	58.650	41.490			29.751
24.560	19.100	5.281	56.360	40.010			27.649
24.660	19.190	5.457	58.620	43.020			28.437
24.760	18.420	5.401	57.780	41.280			29.321
24.860	16.500	5.422	59.490	42.380			32.861
24.960	14.790	5.365	62.850	44.090			36.275
25.060	12.180	5.233	66.080				42.964
25.160	9.994	5.008	67.580	46.230			50.110
25.260	7.764	4.693	70.470	47.380			60.446
25.360	5.756	4.232	73.140	49.210			73.523
25.460	4.163	3.813	75.350	51.290			91.593
25.560	2.746	3.340	77.480	53.000			121.630
25.660	2.760	2.821	79.190	54.800			102.220
25.760	2.782	2.506	80.470	49.980			90.079

Table F.7: PDA Measurements at Different Locations in the Spray-I

$z = 9.500\ inch$							
$Q_\ell = 388.00\ ml/min$				$Q_a = 26200.00\ ml/min$			
$P_{tank} = 60 \pm 2\ psig$				$r_m^* = 9.7625\ mm$			
$PDA\ Samples = 50,000$							
Radial Position	Axial Velocity $U_z\ (m/s)$		Diameter $D\ (\mu m)$		Number Density	Volume Flux	Turbulent Intensity
$x\ (inch)$	$Mean$	RMS	SMD	$Mean$	(cm^{-3})	$(cm^3/s.cm^2)$	(%)
24.160	8.880	6.270	70.826	45.519	1645	0.09024	70.603
24.260	9.112	8.146	59.113	34.360	5887	0.09716	89.391
24.360	17.880	12.160	54.156	32.421	2234	0.07698	68.007
24.460	37.213	14.815	49.395	33.055	425	0.05384	39.813
24.560	51.184	16.365	48.056	34.503	259	0.05073	31.974
24.660	61.378	15.970	43.253	32.932	218	0.03947	26.019
24.760	38.714	15.903	51.227	36.700	368	0.06459	41.079
24.860	14.537	11.018	57.463	36.728	1880	0.10341	75.795
24.960	5.719	5.881	65.974	40.827	7144	0.14908	102.834

Table F.7: PDA Measurements at Different Locations in the Spray-II

$z = 8.000\ inch$							
$Q_\ell = 388.00\ ml/min$			$Q_a = 26200.00\ ml/min$				
$P_{tank} = 60 \pm 2\ psig$			$r_m{}^* = 9.7625\ mm$				
$PDA\ Samples = 50.000$							
Radial Position	Axial Velocity $U_z\ (m/s)$		Diameter $D\ (\mu m)$		Number Density	Volume Flux	Turbulent Intensity
$x\ (inch)$	$Mean$	RMS	SMD	$Mean$	(cm^{-3})	$(cm^3/s.cm^2)$	(%)
23.960	5.343	4.425	80.608	52.882	4363	0.11770	82.807
24.060	5.987	4.735	69.145	38.894	4068	0.07446	79.082
24.160	9.185	5.837	58.961	32.816	1842	0.04655	63.556
24.260	12.885	7.906	53.107	32.299	4450	0.06802	61.362
24.360	21.920	9.697	50.107	31.894	1172	0.05877	44.239
24.460	29.516	10.006	50.378	32.353	774	0.06131	33.901
24.560	37.670	10.645	48.720	31.410	495	0.04753	28.258
24.660	41.412	10.745	45.344	31.403	469	0.04489	25.948
24.760	37.825	10.816	45.277	32.804	486	0.04567	28.595
24.860	28.900	10.871	51.733	35.096	661	0.06605	37.617
24.960	18.146	9.416	58.776	36.238	1274	0.08601	51.891
25.060	11.718	6.543	61.726	33.434	1380	0.05316	55.838
25.160	7.032	5.069	69.196	36.749	2633	0.07914	72.088
25.260	4.312	3.741	75.676	42.444	4907	0.09905	86.764

Table F.7: PDA Measurements at Different Locations in the Spray-III

$z = 6.500\ inch$							
$Q_l = 388.00\ ml/min$				$Q_a = 26200.00\ ml/min$			
$P_{tank} = 60 \pm 2\ psig$				$r_m^* = 9.7625\ mm$			
$PDA\ Samples = 50,000$							
Radial Position	Axial Velocity $U_z\ (m/s)$		Diameter $D\ (\mu m)$		Number Density	Volume Flux	Turbulent Intensity
$x\ (inch)$	$Mean$	RMS	SMD	$Mean$	(cm^{-3})	$(cm^3/s.cm^2)$	(%)
23.760	3.426	2.884	90.298	51.688	4102	0.10224	84.191
23.860	4.222	3.114	81.381	41.476	3688	0.08704	73.737
23.960	5.659	3.819	73.078	34.962	2971	0.06851	67.490
24.060	8.168	4.480	65.765	31.617	1979	0.05251	54.851
24.160	11.607	5.265	60.071	30.678	1230	0.04095	45.364
24.260	15.456	5.645	55.946	30.316	819	0.03393	36.520
24.360	19.126	7.004	55.132	33.180	1247	0.06576	36.621
24.460	22.922	7.226	52.979	33.045	958	0.06023	31.524
24.560	27.335	7.324	49.895	33.003	779	0.05389	26.792
24.660	28.489	7.365	49.858	34.384	819	0.06678	25.851
24.760	27.261	7.456	49.691	33.956	832	0.06390	27.349
24.860	23.822	7.457	52.480	35.461	950	0.07172	31.303
24.960	19.210	7.094	55.936	34.782	1321	0.08474	31.932
25.060	15.236	5.747	58.021	32.819	907	0.04551	37.719
25.160	11.711	5.388	63.477	33.249	1382	0.05701	46.009
25.260	8.080	4.692	67.396	32.865	2220	0.06674	58.096
25.360	6.348	3.857	69.779	35.509	2647	0.07289	60.767
25.460	3.643	3.108	75.834	36.032	5994	0.08648	85.294
25.560	2.347	2.467	83.481	40.904	8306	0.09387	105.097

Table F.7: PDA Measurements at Different Locations in the Spray-IV

$z = 5.000\ inch$							
$Q_\ell = 388.00\ ml/min$			$Q_a = 26200.00\ ml/min$				
$P_{tank} = 60 \pm 2\ psig$			$r_m^* = 9.7625\ mm$				
$PDA\ Samples = 50,000$							
Radial Position	Axial Velocity $U_z\ (m/s)$		Diameter $D\ (\mu m)$		Number Density	Volume Flux	Turbulent Intensity
$x\ (inch)$	$Mean$	RMS	SMD	$Mean$	(cm^{-3})	$(cm^3/s.cm^2)$	(%)
23.560	2.470	2.303	88.036	41.789	6226	0.09053	93.293
23.660	3.577	2.672	80.929	35.855	4926	0.08740	74.707
23.760	4.966	3.050	75.384	33.356	3418	0.07343	61.416
23.860	6.472	3.429	72.137	35.040	2361	0.06777	52.984
23.960	8.527	3.823	66.935	33.620	1811	0.06100	44.835
24.060	10.510	4.144	62.873	31.564	1449	0.05015	39.428
24.160	12.552	4.427	60.822	32.496	1174	0.05021	35.274
24.260	14.638	4.698	58.525	32.360	907	0.04433	32.095
24.360	17.159	4.763	54.816	32.249	784	0.04055	27.276
24.460	18.863	5.282	55.377	35.417	1251	0.07946	28.000
24.560	20.267	5.712	59.565	42.640	1083	0.11810	28.183
24.660	20.785	5.565	54.785	38.510	1201	0.09599	26.772
24.760	19.897	5.541	53.097	35.763	1233	0.08057	27.849
24.860	18.457	5.577	54.098	35.363	1274	0.08091	30.215
24.960	15.788	5.516	57.912	36.501	1505	0.08880	34.936
25.060	13.512	4.847	59.996	35.131	1158	0.06203	35.872
25.160	11.379	4.676	60.971	32.318	1287	0.04918	41.094
25.260	8.876	4.363	66.770	32.591	1826	0.05805	49.150
25.360	6.774	3.980	70.334	34.177	2116	0.05861	58.757
25.460	5.336	3.352	71.428	34.791	3476	0.08039	62.823
25.560	3.774	2.940	75.383	36.553	5167	0.09081	77.888
25.660	2.783	2.510	78.364	36.303	6045	0.07770	90.202
25.760	2.044	2.137	82.047	40.034	6159	0.06637	104.558

Table F.7: PDA Measurements at Different Locations in the Spray-V

$z = 4.000\ inch$							
$Q_\ell = 388.00\ ml/min$				$Q_a = 26200.00\ ml/min$			
$P_{tank} = 60 \pm 2\ psig$				$r_m^* = 9.7625\ mm$			
$PDA\ Samples = 50,000$							
Radial Position	Axial Velocity $U_z\ (m/s)$		Diameter $D\ (\mu m)$		Number Density	Volume Flux	Turbulent Intensity
$x\ (inch)$	$Mean$	RMS	SMD	$Mean$	(cm^{-3})	$(cm^3/s.cm^2)$	(%)
23.360	1.856	1.954	87.474	32.612	6675	0.05349	105.273
23.460	2.950	2.159	79.821	30.178	4134	0.05516	73.200
23.560	3.594	2.385	80.388	36.778	4635	0.09345	66.344
23.660	4.802	2.728	74.077	33.217	3381	0.07083	56.804
23.760	5.712	3.152	71.385	31.135	2679	0.05640	55.179
23.960	8.765	3.772	65.219	30.923	1833	0.05364	43.031
24.160	11.633	4.055	61.006	31.196	1229	0.04648	34.855
24.360	15.765	4.071	54.599	30.683	853	0.03671	25.821
24.560	18.187	3.996	51.055	31.097	685	0.03299	21.969
24.760	17.846	4.050	52.254	32.209	723	0.03725	22.694
24.960	14.881	4.210	55.257	32.357	915	0.04167	28.294
25.160	11.400	4.175	63.356	37.175	1159	0.06337	36.624
25.360	7.587	3.786	67.115	33.888	1899	0.05573	49.901
25.560	4.983	3.117	72.827	31.985	3447	0.06782	62.547
25.760	2.642	2.434	78.592	34.410	5868	0.06840	92.148
25.960	1.327	1.791	81.968	29.578	9163	0.04415	134.979

Table F.8: PDA Measurements for Various Water and Air Flowrates-I

$Q_l = 207.00\ ml/min$			$Q_a = 22900.00\ ml/min$				
$x = 24.435\ inch$			$PDASamples = 50,000$				
$P_{tank} = 60 \pm 2\ psig$			$r_m^* = 9.7625\ mm$				
Axial Position	Axial Velocity $U_z\ (m/s)$		Diameter $D\ (\mu m)$		Number Density	Volume Flux	Turbulent Intensity
$z\ (inch)$	$Mean$	RMS	SMD	$Mean$	(cm^{-3})	$(cm^3/s.cm^2)$	(%)
9.7675	60.570	20.490	28.417	21.741	338	0.01470	33.828
9.4675	52.805	18.647	29.397	22.653	409	0.01657	35.313
9.1675	45.303	15.777	28.992	21.393	549	0.01633	34.826
8.8675	39.235	13.781	30.481	22.671	650	0.01925	35.124
8.5675	34.313	11.779	30.357	22.131	835	0.01993	34.327
8.2675	29.829	10.274	31.093	22.394	1025	0.02131	34.444
7.9675	26.659	8.945	30.977	21.413	1181	0.02004	33.544
7.6675	24.096	7.963	32.192	22.480	1380	0.02420	33.048
7.3675	21.879	7.002	32.420	22.041	1685	0.02531	32.004
7.0675	20.025	6.493	33.672	23.464	1666	0.02754	32.426
6.7675	18.364	5.604	33.168	22.241	1872	0.02450	30.517
6.4675	17.022	5.282	35.040	24.127	2041	0.03147	31.029
6.1675	17.267	4.378	33.771	20.589	964	0.01247	25.352
5.8675	16.143	4.154	34.941	21.756	1118	0.01564	25.732
5.5675	15.449	3.852	35.172	21.477	1164	0.01531	24.930
5.2675	14.719	3.652	36.996	24.812	1240	0.02110	24.812
4.9675	14.051	3.524	36.066	21.947	1221	0.01627	25.079
4.6675	13.486	3.305	35.941	21.041	1269	0.01465	24.503
4.3675	12.923	3.106	40.200	27.998	1476	0.03511	24.035
4.0675	12.536	2.973	37.241	23.134	1587	0.02089	23.698

Table F.8: PDA Measurements for Various Water and Air Flowrates-II

$Q_\ell = 207.00\ ml/min$				$Q_a = 26200.00\ ml/min$			
$x = 24.435\ inch$				$PDASamples = 50,000$			
$P_{tank} = 60 \pm 2\ psig$				$r_m{}^* = 9.7625\ mm$			
Axial Position	Axial Velocity $U_z\ (m/s)$		Diameter $D\ (\mu m)$		Number Density	Volume Flux	Turbulent Intensity
$z\ (inch)$	$Mean$	RMS	SMD	$Mean$	(cm^{-3})	$(cm^3/s.cm^2)$	(%)
9.4675	62.870	19.245	29.057	23.650	324	0.01779	30.610
9.1675	56.954	17.672	27.821	21.745	373	0.01460	31.028
8.8675	51.026	15.885	29.752	23.040	490	0.02013	31.131
8.5675	45.318	13.619	29.314	22.002	569	0.01815	30.052
8.2675	40.209	12.093	30.343	22.539	645	0.01929	30.074
7.9675	36.272	10.764	29.631	21.206	795	0.01821	29.676
7.6675	32.890	9.835	30.899	22.308	869	0.02043	29.901
7.3675	29.966	8.872	31.102	22.048	1012	0.02093	29.608
7.0675	27.858	8.146	31.434	21.975	1245	0.02373	29.241
6.7675	25.922	7.569	34.136	24.780	1354	0.03436	29.198
6.4675	23.863	6.991	33.338	23.585	1362	0.02681	29.299
6.1675	22.239	6.426	32.567	21.594	1800	0.02589	28.897
5.8675	20.705	6.057	33.445	22.615	1884	0.02930	29.252
5.5675	19.331	5.751	35.641	25.028	1868	0.03764	29.749
5.2675	18.208	5.406	34.672	23.363	2112	0.03302	29.690
4.9675	18.162	4.528	33.290	20.227	1089	0.01409	24.929
4.6675	17.601	4.290	33.709	20.352	1098	0.01407	24.376
4.3675	16.686	4.179	34.330	21.004	1008	0.01329	25.048
4.0675	16.060	3.945	34.497	20.955	1125	0.01440	24.567

Table F.8: PDA Measurements for Various Water and Air Flowrates-III

$Q_l = 207.00\ ml/min$			$Q_a = 29500.00\ ml/min$				
$x = 24.435\ inch$			$PDASamples = 50.000$				
$P_{tank} = 60 \pm 2\ psig$			$r_m{}^* = 9.7625\ mm$				
Axial Position	Axial Velocity (m/s)		Diameter $D\ (\mu m)$		Number Density	Volume Flux	Turbulent Intensity
$z\ (inch)$	$Mean$	RMS	SMD	$Mean$	(cm^{-3})	$(cm^3/s.cm^2)$	(%)
9.4675	68.737	18.722	30.692	26.084	248	0.01964	27.237
9.1675	65.620	17.976	29.977	24.533	289	0.01879	27.394
8.8675	59.818	16.886	31.981	25.895	327	0.02245	28.228
8.5675	55.298	15.321	31.267	24.400	406	0.02190	27.706
8.2675	50.120	13.721	32.255	24.772	439	0.02215	27.376
7.9675	46.164	12.466	32.265	24.251	487	0.02148	27.004
7.6675	41.923	11.296	32.173	23.846	602	0.02264	26.944
7.3675	38.598	10.503	32.006	23.347	708	0.02293	27.212
7.0675	35.364	9.593	32.127	23.212	830	0.02385	27.126
6.7675	33.029	9.059	33.284	23.986	857	0.02517	27.428
6.4675	30.543	8.663	35.986	27.116	900	0.03411	28.362
6.1675	28.443	8.092	33.839	24.039	1118	0.02774	28.449
5.8675	26.950	7.686	34.580	24.660			28.519
5.5675	24.993	7.176	35.060	24.909	1335	0.03326	28.711
5.2675	23.591	6.809	36.079	26.575	1645	0.04638	28.864
4.9675	22.367	6.378	34.710	23.293	1518	0.03040	28.515
4.6675	21.213	6.124	37.491	27.349	1786	0.05055	28.870
4.3675	20.175	5.757	35.768	24.813	1754	0.03579	28.535
4.0675	19.154	5.675	37.290	26.819	1881	0.04523	29.633

Table F.8: PDA Measurements for Various Water and Air Flowrates-IV

$Q_\ell = 207.00\ ml/min$			$Q_a = 32745.00\ ml/min$				
$x = 24.435\ inch$			$PDASamples = 50,000$				
$P_{tank} = 60 \pm 2\ psig$			$r_m^* = 9.7625\ mm$				
Axial Position	Axial Velocity $U_z\ (m/s)$		Diameter $D\ (\mu m)$		Number Density	Volume Flux	Turbulent Intensity
$z\ (inch)$	$Mean$	RMS	SMD	$Mean$	(cm^{-3})	$(cm^3/s.cm^2)$	(%)
9.4675	71.481	18.569	30.302	25.851	199	0.01602	25.978
9.1675	68.552	17.887	30.506	25.123	268	0.01959	26.096
8.8675	63.597	16.978	31.76	25.730	297	0.02137	26.696
8.5675	59.220	15.833	31.398	24.487	356	0.02108	26.736
8.2675	54.208	14.252	32.561	25.330	399	0.02321	26.292
7.9675	50.121	12.948	30.632	22.599	433	0.01702	25.834
7.6675	45.901	11.942	31.706	23.403	551	0.02173	26.017
7.3675	42.468	10.957	31.734	22.873	587	0.02017	25.802
7.0675	39.203	10.577	32.603	23.365	674	0.02297	26.980
6.7675	36.150	9.884	31.510	22.008	790	0.02066	27.342
6.4675	33.984	9.254	32.111	22.502	901	0.02308	27.231
6.1675	31.755	8.846	33.095	23.167	901	0.02326	27.857
5.8675	29.643	8.341	33.480	23.544	1084	0.02761	28.139
5.5675	27.898	7.915	34.147	23.793	1190	0.02995	28.372
5.2675	26.287	7.520	35.499	25.229	1154	0.03232	28.607
4.9675	24.819	7.069	34.949	24.192	1286	0.03035	28.482
4.6675	23.711	6.739	34.902	22.742	1353	0.02675	28.419
4.3675	22.348	6.492	35.511	23.821	1392	0.02946	29.052
4.0675	21.599	6.187	36.671	25.047	1423	0.03394	28.647

Table F.8: PDA Measurements for Various Water and Air Flowrates-V

$Q_\ell = 388.00\ ml/min$			$Q_a = 22900.00\ ml/min$				
$x = 24.435\ inch$			$PDASamples = 50,000$				
$P_{tank} = 60 \pm 2\ psig$			$r_m^* = 9.7625\ mm$				
Axial Position	Axial Velocity $U_z\ (m/s)$		Diameter $D\ (\mu m)$		Number Density	Volume Flux	Turbulent Intensity
$z\ (inch)$	$Mean$	RMS	SMD	$Mean$	(cm^{-3})	$(cm^3/s.cm^2)$	(%)
9.1675	55.648	14.602	34.546	25.205	327	0.02104	26.239
8.8675	49.628	12.999	36.678	26.745	422	0.02784	26.193
8.5675	43.879	11.086	35.753	25.081	482	0.02303	25.265
8.2675	38.764	9.697	35.332	24.730	551	0.02149	25.015
7.9675	34.383	8.561	35.359	24.265	702	0.02308	24.900
7.6675	31.181	7.639	36.195	24.713	895	0.02747	24.499
7.3675	28.339	6.893	36.231	24.376	997	0.02650	24.323
7.0675	26.074	6.239	36.572	24.562	1125	0.02864	23.927
6.7675	23.896	5.777	37.420	25.179	1353	0.03304	24.176
6.4675	22.289	5.386	38.639	26.245	1338	0.03445	24.164
6.1675	20.763	4.954	38.465	24.785	1482	0.03190	23.861
5.8675	19.536	4.666	39.772	26.225	1713	0.03977	23.886
5.5675	18.388	4.360	40.447	26.856	1727	0.04108	23.709
5.2675	18.097	3.704	40.044	24.527	944	0.02213	20.470
4.9675	17.291	3.558	40.619	24.206	877	0.01950	20.577
4.6675	16.595	3.424	41.652	24.985	912	0.02110	20.631
4.3675	15.969	3.274	42.421	24.637	906	0.02016	20.501
4.0675	15.368	3.095	43.360	24.985	1063	0.02407	20.137

Table F.8: PDA Measurements for Various Water and Air Flowrates-VI

$Q_\ell = 388.00\ ml/min$			$Q_a = 26200.00\ ml/min$				
$x = 24.435\ inch$			$PDA\ Samples = 50.000$				
$P_{tank} = 60 \pm 2\ psig$			$r_m{}^* = 9.7625\ mm$				
Axial Position	Axial Velocity $U_z\ (m/s)$		Diameter $D\ (\mu m)$		Number Density	Volume Flux	Turbulent Intensity
$z\ (inch)$	$Mean$	RMS	SMD	$Mean$	(cm^{-3})	$(cm^3/s.cm^2)$	(%)
9.6675	73.660	16.139	35.478	29.942	192	0.02538	21.910
9.2675	65.915	15.126	36.779	29.823	271	0.03147	22.948
8.8675	58.181	13.763	38.319	30.066	335	0.03510	23.655
8.4675	51.583	12.042	35.088	25.806	391	0.02347	23.344
8.0675	45.145	10.503	36.022	26.775	501	0.02794	23.266
7.6675	39.731	9.221	36.288	26.389	679	0.03215	23.209
7.2675	35.179	8.130	35.417	24.920	735	0.02603	23.110
6.8675	31.967	7.424	36.998	26.379	922	0.03467	23.223
6.4675	29.041	6.998	38.692	27.946	1045	0.04167	24.097
6.0675	26.681	6.538	38.900	27.064	1186	0.03963	24.504
5.6675	24.632	6.056	40.496	29.028	1230	0.04692	24.588
5.2675	22.647	5.564	40.478	27.722	1489	0.04676	24.569
4.8675	21.054	5.249	41.253	27.772	1439	0.04315	24.929
4.4675	19.738	4.867	42.647	29.715	1606	0.05491	24.660
4.0675	18.509	4.469	43.644	30.401	1750	0.06023	24.143

Table F.8: PDA Measurements for Various Water and Air Flowrates-VII

$Q_\ell = 388.00\ ml/min$				$Q_a = 29500.00\ ml/min$			
$x = 24.435\ inch$				$PDASamples = 50.000$			
$P_{tank} = 60 \pm 2\ psig$				$r_m^* = 9.7625\ mm$			
Axial Position	Axial Velocity $U_z\ (m/s)$		Diameter $D\ (\mu m)$		Number Density	Volume Flux	Turbulent Intensity
$z\ (inch)$	$Mean$	RMS	SMD	$Mean$	(cm^{-3})	$cm^3/s.cm^2$	(%)
8.8675	62.712	14.359	39.881	33.686	217	0.03230	22.897
8.5675	58.080	13.300	38.993	32.106	309	0.03668	22.900
8.2675	54.020	12.180	37.906	30.337	348	0.03324	22.548
7.9675	50.380	11.136	37.325	29.076	412	0.03301	22.105
7.6675	46.622	10.344	37.695	29.252	491	0.03637	22.187
7.3675	43.559	9.598	37.533	28.617	532	0.03459	22.034
7.0675	40.534	9.064	37.942	28.670	581	0.03530	22.362
6.7675	37.953	8.653	38.964	29.750	642	0.03995	22.799
6.4675	35.579	8.289	40.060	30.729	785	0.05093	23.299
6.1675	33.468	7.798	39.820	30.064	865	0.04975	23.300
5.8675	31.934	7.776	43.607	35.064	805	0.07073	24.350
5.5675	29.913	7.315	42.119	32.635	1026	0.06740	24.455
5.2675	28.284	6.798	40.671	29.774	987	0.04721	24.036
4.9675	26.934	6.409	41.006	30.399	1031	0.04997	23.795
4.6675	25.649	6.202	42.488	31.639	1076	0.05547	24.179
4.3675	24.553	5.937	41.826	30.200	1238	0.05340	24.180
4.0675	23.466	5.697	42.448	29.983	1262	0.05292	24.279

Table F.8: PDA Measurements for Various Water and Air Flowrates-VIII

$Q_\ell = 388.00\ ml/min$			$Q_a = 32745.00\ ml/min$				
$x = 24.435\ inch$			$PDA\ Samples = 50,000$				
$P_{tank} = 60 \pm 2\ psig$			$r_m{}^* = 9.7625\ mm$				
Axial Position	Axial Velocity $U_z\ (m/s)$		Diameter $D\ (\mu m)$		Number Density	Volume Flux	Turbulent Intensity
$z\ (inch)$	$Mean$	RMS	SMD	$Mean$	(cm^{-3})	$(cm^3/s.cm^2)$	(%)
8.8675	65.776	14.706	38.789	33.102	219	0.03241	22.358
8.5675	60.986	13.609	39.446	33.063	256	0.03514	22.316
8.2675	57.103	12.557	39.001	32.110	319	0.03729	21.989
7.9675	53.461	11.628	37.341	29.452	365	0.03198	21.750
7.6675	49.792	10.795	38.002	29.865	448	0.03757	21.681
7.3675	46.482	10.189	38.410	29.851	483	0.03780	21.921
7.0675	43.392	9.469	38.080	28.994	578	0.03930	21.823
6.7675	40.564	9.056	39.539	30.695	592	0.04372	22.326
6.4675	38.372	8.769	41.780	33.189	677	0.05854	22.853
6.1675	35.905	8.235	39.161	29.343	782	0.04501	22.937
5.8675	33.612	7.996	40.748	30.849	820	0.05095	23.789
5.5675	31.946	7.708	42.201	32.914	866	0.06212	24.128
5.2675	30.213	7.309	41.381	30.802	981	0.05552	24.192
4.9675	28.656	7.093	42.302	32.411	1005	0.06125	24.753
4.6675	27.059	6.802	42.684	32.204	1207	0.06851	25.137
4.3675	25.437	6.413	43.875	33.165	1261	0.07415	25.213
4.0675	24.455	6.056	42.841	31.303	1366	0.06578	24.765

Table F.8: PDA Measurements for Various Water and Air Flowrates-IX

$Q_\ell = 580.00\ ml/min$			$Q_a = 26200.00\ ml/min$				
$x = 24.435\ inch$			$PDA\ Samples = 50.000$				
$P_{tank} = 60 \pm 2\ psig$			$r_m{}^* = 9.7625\ mm$				
Axial Position	Axial Velocity $U_z\ (m/s)$		Diameter $D\ (\mu m)$		Number Density	Volume Flux	Turbulent Intensity
$z\ (inch)$	$Mean$	RMS	SMD	$Mean$	(cm^{-3})	$(cm^3/s.cm^2)$	(%)
9.4675	67.025	16.296	39.507	33.196	213	0.03513	24.313
9.1675	63.415	14.854	39.446	31.802	245	0.03497	23.424
8.8675	58.066	13.268	40.571	32.001	290	0.03816	22.849
8.5675	53.831	11.983	38.834	29.211	358	0.03401	22.261
8.2675	48.861	10.590	38.621	28.464	427	0.03348	21.675
7.9675	44.126	9.454	37.187	26.489	494	0.02852	21.424
7.6675	40.088	8.775	37.580	26.935	598	0.03225	21.888
7.3675	36.742	8.085	36.596	25.676	706	0.02982	22.004
7.0675	33.912	7.604	37.751	27.123	806	0.03567	22.424
6.7675	31.502	7.089	37.104	26.140	910	0.03362	22.505
6.4675	29.226	6.671	37.560	26.333	1065	0.03774	22.824
6.1675	27.455	6.242	38.595	27.388	1157	0.04285	22.737
5.8675	25.532	5.919	38.788	27.500	1291	0.04528	23.182
5.5675	24.207	5.641	39.060	27.620	1345	0.04517	23.303
5.2675	22.984	5.325	39.622	28.769	1496	0.05365	23.166
4.9675	21.779	5.094	40.308	29.362	1573	0.05695	23.389
4.6675	21.039	4.745	40.005	28.704	1682	0.05552	22.555
4.3675	19.988	4.601	41.465	30.424	1681	0.06322	23.021
4.0675	19.144	4.393	41.764	31.421	1637	0.06539	22.947

Table F.8: PDA Measurements for Various Water and Air Flowrates-X

$Q_\ell = 580.00\ ml/min$			$Q_a = 29500.00\ ml/min$				
$x = 24.435\ inch$			$PDA\ Samples = 50,000$				
$P_{tank} = 60 \pm 2\ psig$			$r_m{}^* = 9.7625\ mm$				
Axial Position	Axial Velocity $U_z\ (m/s)$		Diameter $D\ (\mu m)$		Number Density	Volume Flux	Turbulent Intensity
$z\ (inch)$	$Mean$	RMS	SMD	$Mean$	(cm^{-3})	$(cm^3/s.cm^2)$	(%)
9.1675	60.156	16.467	42.617	35.317	234	0.04300	27.373
8.8675	56.754	14.547	43.951	36.665	247	0.04586	25.651
8.5675	54.768	12.989	42.354	33.582	314	0.04503	23.716
8.2675	51.206	11.498	42.098	32.652	363	0.04488	22.454
7.9675	47.975	10.376	40.479	30.123	421	0.03904	21.627
7.6675	44.691	9.549	40.390	29.928	527	0.04359	21.367
7.3675	41.656	8.703	39.919	28.838	559	0.03873	20.892
7.0675	38.995	8.138	40.524	30.025	685	0.04784	20.870
6.7675	36.504	7.643	40.183	29.344	736	0.04527	20.938
6.4675	34.209	7.168	40.055	28.720	747	0.04052	20.954
6.1675	32.456	6.845	40.964	30.093	976	0.05694	21.091
5.8675	30.928	6.600	40.836	30.013	1057	0.05922	21.341
5.5675	29.549	6.249	40.739	29.626	1038	0.05368	21.150
5.2675	27.878	6.027	41.453	30.793	1066	0.05801	21.620
4.9675	26.691	5.755	41.911	31.310	1179	0.06431	21.560
4.6675	25.467	5.528	42.070	30.931	1190	0.06062	21.705
4.3675	24.561	5.323	42.414	31.136	1267	0.06425	21.673
4.0675	23.653	5.330	43.219	33.310	1302	0.07645	22.536

Table F.8: PDA Measurements for Various Water and Air Flowrates-XI

$Q_\ell = 580.00\ ml/min$			$Q_a = 32745.00\ ml/min$				
$x = 24.435\ inch$			$PDA\ Samples = 50.000$				
$P_{tank} = 60 \pm 2\ psig$			$r_m{}^* = 9.7625\ mm$				
Axial Position	Axial Velocity $U_z\ (m/s)$		Diameter $D\ (\mu m)$		Number Density	Volume Flux	Turbulent Intensity
$z\ (inch)$	$Mean$	RMS	SMD	$Mean$	(cm^{-3})	$(cm^3/s.cm^2)$	(%)
9.1675	64.550	16.518	43.604	36.502	154	0.03307	25.589
8.8675	61.824	14.543	45.075	38.624	177	0.04053	23.523
8.5675	59.691	13.303	43.647	36.316	264	0.04942	25.287
8.2675	55.942	11.943	43.819	35.754	307	0.05178	21.350
7.9675	52.926	10.968	42.648	33.401	345	0.04553	20.723
7.6675	49.818	10.067	41.313	32.037	418	0.04605	20.208
7.3675	46.781	9.295	40.418	30.452	508	0.04547	19.869
7.0675	43.820	8.825	40.972	31.502	577	0.05152	20.139
6.7675	41.531	8.396	40.305	30.778	618	0.04911	20.217
6.4675	39.171	7.918	40.217	30.366	659	0.04759	20.215
6.1675	37.270	7.620	41.088	31.371	704	0.05242	20.446
5.8675	35.171	7.349	40.882	31.384	786	0.05550	20.895
5.5675	33.562	7.154	40.869	31.254	868	0.05729	21.315
5.2675	31.896	6.875	41.708	32.490	976	0.06862	21.556
4.9675	30.471	6.757	42.232	33.345	939	0.06747	22.176
4.6675	29.112	6.433	42.289	32.766	1011	0.06672	22.096
4.3675	28.066	6.285	43.491	34.456	1037	0.07618	22.394
4.0675	27.324	6.234	43.243	35.194	1173	0.08695	22.815

Table F.8: PDA Measurements for Various Water and Air Flowrates-XII

$Q_\ell = 580.00\ ml/min$			$Q_a = 35722.00\ ml/min$				
$x = 24.435\ inch$			$PDA\ Samples = 50,000$				
$P_{tank} = 60 \pm 2\ psig$			$r_m^* = 9.7625\ mm$				
Axial Position	Axial Velocity $U_z\ (m/s)$		Diameter $D\ (\mu m)$		Number Density	Volume Flux	Turbulent Intensity
$z\ (inch)$	$Mean$	RMS	SMD	$Mean$	(cm^{-3})	$(cm^3/s.cm^2)$	(%)
9.1675	63.620	16.860	43.780	36.880			22.447
8.8675	60.550	14.890	45.020	38.620			22.266
8.5675	60.810	13.7 4	43.560	36.360			22.803
8.2675	57.510	12.460	43.460	35.450			22.166
7.9675	54.250	11.410	42.400	33.720			21.587
7.6675	51.030	10.640	41.560	32.550			21.398
7.3675	48.090	9.809	40.280	30.620			21.222
7.0675	44.920	9.221	40.680	31.340			21.237
6.7675	42.630	8.867	40.510	31.000			20.978
6.4675	39.790	8.347	40.760	30.970			20.800
6.1675	37.910	8.051	41.550	31.870			20.528
5.8675	36.510	7.748	41.150	31.650			20.397
5.5675	35.600	7.502	41.420	31.900			20.850
5.2675	33.330	7.195	42.320	33.010			21.032
4.9675	31.720	7.031	43.050	34.170			21.666
4.6675	30.000	6.841	43.270	33.970			22.595
4.3675	29.560	6.582	43.930	34.730			24.591
4.0675	28.570	6.413	44.000	35.550			26.501